

Development and application of geobotanical remote sensing
methods for mineral exploration in thick vegetation areas

Arie Naftali Hawu Hede

2016

**Development and application of geobotanical remote sensing
methods for mineral exploration in thick vegetation areas**



Arie Naftali Hawu Hede

Graduate School of Engineering

Kyoto University

This dissertation is submitted for the degree of

Doctor of Philosophy in Engineering

January 2016

Acknowledgements

I believe that every good gift and perfect gift is from above (James 1:17a). For this, as for everything, I am grateful to God, including the knowledge, wisdom, power, good health, and wellbeing that were necessary for finishing this dissertation volume. This book will become another chapter in the story of my life.

I would like to express my deepest gratitude to my supervisor, Prof. Katsuaki Koike, Graduate School of Engineering, Kyoto University, Japan. Throughout my studies at Kyoto University, he provided continuous encouragement, wise advice, and tons of great ideas. He always challenged me to take one more step forward. I am extremely thankful and indebted to him for every valuable thing he taught me.

I am heartily thankful to the committee members, Prof. Hitoshi Mikada and Prof. Masayuki Tamura for their constructive comments and have reviewed my dissertation. I would like to express my deepest thanks to my co-supervisors, Prof. Mamoru Mimura and Assoc. Prof. Tadanori Goto. My grateful thanks also extend to Asst. Prof. Koki Kashiwaya, for his kind assistance and help during the laboratory experiments.

I am indebted to my friends in the Laboratory of Environmental Geosphere Engineering for providing a nice environment in which to learn daily. I give special thanks to Kubo-san, Tian, Lu, Hoang, Tezuka-san, Keichi-san, Takahashi-san, Baba-san, Kobayashi-san, Maher, Luis, and Rios. I wish to thank Watanabe-san for all her kindness and helping me in undertaking the necessary documents related to my study in Kyoto University.

I would like to take this opportunity to give my sincere thanks to all my colleagues in the Earth Resources Exploration Research Group, Faculty of Mining and Petroleum Engineering,

Institut Teknologi Bandung (ITB), Indonesia, who have always supported me. My deepest and most sincere gratitude goes to Prof. Sudarto Notosiswoyo, Dr. Komang Anggayana, and Dr. Budi Sulistijo, who gave me additional support funding during the field study. I gratefully thank Dr. Nur Heriawan and Dr. Irwan Iskandar for their recommendation and making it possible for me to be connected with Koike-sensei. To Dr. Syafrizal, Dr. Lilik Eko Widodo, Mrs. Teti Indriati, Dr. Agus Haris, and Andy Yahya, I would very much like to extend my most sincere thanks for their support.

I wish to express my sincere gratitude to Dr. Ryoichi Kouda of the Geological Survey of Japan, AIST, Dr. Ryoichi Yamada of the Graduate School of Science, Tohoku University, and Mr. Hidekaze Kato of the International Institute for Mining Technology (MINETEC) for their precious instructions of the kuroko deposits and the guidance of geological survey in the Kosaka area. I would like also to give my gratitude to Mr. Hari Widjajanto, Mr. Kusyanto, Mr. Aris Asikin, and Mr. Wiwid Aryanto from PT. Aneka Tambang (Antam), Indonesia for providing me with permission to conduct a field study and use the data.

My sincere thankfulness go as well to the Ministry of Education, Culture, Sports, Science, and Technology of Japan—Japanese *Monbukagakusho*—for the scholarship that has supported my daily life and study during these three years of pursuing a doctoral degree.

I wish to thank my entire family in Indonesia who provided me with continuous support in their prayers. My brothers, sisters, and friends, thank you for supporting me. Lastly and most importantly, I wish to thank my parents; my father, Seprianus Serchan Hede who waiting for me in Indonesia and my mother, Sri Handayani Sulastri who took the lead to heaven many years ago. I dedicate this dissertation to them.

Abstract

In the 21st century, the world has experienced a rapid increase in the consumption of and demand for mineral resources, which has resulted in considerable needs for innovations in mineral exploration. Remote sensing is one of the exploration techniques that is commonly used during the prospecting phase because it can provide a rapid assessment at low costs and with minimal risks. However, as for the spectral applications, the validity of remote sensing is limited to arid and semi-arid areas where vegetation is sparse or absent. Exploration and potential assessments of mineral deposits by optical remote sensing are difficult in thickly vegetated areas because the reflectance spectra of the vegetation conceal the spectra of the underlying soil and rocks. To overcome this constraint, the use of geobotanical remote sensing (GBRS) can be considered. Therefore, this study was undertaken to develop GBRS methods for analyzing vegetation anomalies under metal stress related to mineral deposits, and also to address an improved image enhancement method to solve the problem of spectral mixture. An overview of each chapter can be found below.

The introduction, including the background, the general notion of GBRS, the objectives, the study areas, and the datasets used in this study, can be found in **Chapter 1**. **Chapter 2** concerns the development of a GBRS method to analyze the effect of metals on vegetation reflectance at various wavelengths, from the visible to the short-wave infrared (SWIR) regions. To this end, laboratory experiments were undertaken to clarify the relationships among the metals (Cu, Pb, Zn, and Cd) in soils and the reflectance spectra of a selected plant species. Then, I propose a new vegetation index (VI) using the reflectance data in five bands, from the visible green to SWIR regions, called the vegetation index considering greenness and short-wave infrared (VIGS), which can accurately detect vegetation stress caused by metal contamination of

the soil. The results clarified the featured changes in the reflectance spectra according to the metal types and contents in the soil in the region from the visible to the SWIR range. Moreover, the results indicate that the VIGS can enhance the identification of differences in vegetation stress depending on the metal content of the soil.

The relationship between geochemical data (Cu, Pb, Zn, Co, Ni, Mn, Li, K, Fe, and Cr) and the vegetation reflectance in natural conditions analyzed using a multispectral remote sensing image (e.g., Landsat ETM+) is discussed in **Chapter 3**. The study area is located in Jambi, Indonesia, where mineral deposits of copper porphyry exist and mineralized zones are distributed throughout the tropical forest region. This chapter demonstrates the possibility of using reflectance values derived from multispectral satellite imagery to detect geochemically enriched zones in dense vegetation areas.

In **Chapter 4**, a new method is proposed to apply the facts about VIGS characteristics that were developed in relation to mineral exploration using the same data from the previous chapter. Rather than a pixel-by-pixel analysis, this chapter evaluates the positional concordance of the VI anomalies derived from the imagery with the selected metals (Cu, Pb, and Zn) concentration distribution, as analyzed using a kriging interpolation. The effectiveness of VIGS is proven because VIGS anomalies appeared in high-content zones common to the three metals, which is similar to the laboratory experiment results. Moreover, this study also demonstrates that GBRS study requires an understanding of physical evaluations in terms of a correlation with vegetation characteristics.

Chapter 5 presents novel combined methods for remote detection of vegetation anomalies that can be used as indicators of ore deposit occurrences by using VI analysis as an indicator of plants' physiological activities. The study area is in the Hokuroku district in Akita,

northern Japan, which is one of the richest ore deposit (volcanogenic massive sulfide and vein-type) districts in Japan and is covered by thick vegetation. The superiority of this method is demonstrated by the correlation of the vegetation anomaly zones with the geologic exploration datasets. As a result, vegetation anomaly zones were drawn apparently similar to the ring structures that controlled the distributions of ore deposits, and most major ore deposits that are located in the forest areas were in agreement with the vegetation anomalies.

Chapter 6 aims to improve the directed principal component analysis (DPCA) to enhance the hydrothermal alteration zone in a vegetated area by optimizing the band combination ratio integrated with a geographic information system-based analysis. As a case study, the Pongkor district in West Java, Indonesia was selected because vein-type Au-Ag epithermal deposits are found in this area, mostly covered by thick vegetation. This study focuses on the ASTER image, which has a more advanced capability to discriminate silicates and clay minerals through a broader range of data in the SWIR region. In this chapter, the possibility of an optimization ratio derived from the band combination to represent the components (vegetation and minerals) is explored. Finally, the concluding remarks, including the primary results from all chapters, can be found in **Chapter 7**. A list of future works related to this study, which will help to develop GBRS study further, is also presented.

Keywords: Geobotany, remote sensing, vegetation index, reflectance spectra, mineral exploration

Contents

Acknowledgements.....	i
Abstract	iii
Contents	vi
List of Figures.....	ix
List of Tables	xiv
Chapter 1 Introduction	1
1.1. Background of study	1
1.2. Objectives.....	4
1.3. Geobotanical Remote Sensing (GBRS)	5
1.4. Study area.....	9
1.5. Datasets	10
1.5.1. Field survey and laboratory experiments.....	11
1.5.2. Satellite imagery and others supporting data.....	12
1.6. Structure of dissertation	15
References.....	17
Chapter 2 Development of a new vegetation index for detecting vegetation anomalies in metal-contaminated soils.....	20
2.1. Introduction	20
2.2. Materials and methods	24
2.2.1. Laboratory experiment.....	24
2.2.2. Definition of the new vegetation index.....	27
2.3. Results	30
2.3.1. Physiological and reflectance analysis.....	30
2.3.2. Comparison between NDVI and VIGS.....	35
2.4. Discussion	36
2.4.1. Changes in the plants physiology	36
2.4.2. Changes in the spectroscopic features	38
2.5. Conclusions	40

References.....	41
Chapter 3 Correlating vegetation reflectance spectra by satellite imagery with geochemical data	45
3.1. Introduction	45
3.2. Study area and geological datasets.....	46
3.2.1. Geologic setting	46
3.2.2. Geochemical data.....	51
3.3. Methods.....	52
3.3.1. Image processing for atmospheric and topographic correction	52
3.3.2. Supervised classification.....	53
3.3.3. Statistical analysis.....	55
3.4. Results and discussion.....	56
3.4.1. Characterization of geochemical data.....	56
3.4.2. Relation between geochemical data and vegetation reflectance.....	57
3.4.3. PLSR analysis	61
3.5. Conclusions	63
References.....	63
Chapter 4 Application of a new vegetation index to detecting vegetation anomaly due to metals enrichment in a tropical forest	66
4.1. Introduction	66
4.2. Methodology and data processing.....	67
4.2.1. Geochemical spatial data distribution.....	67
4.2.2. VI calculation.....	70
4.3. Results	71
4.3.1. Spatial distribution of metal contents	71
4.3.2. Relationship between VIs and control factors of vegetation stress	74
4.3.3. Correlation of VIs with metal contents.....	79
4.4. Discussion	82
4.5. Conclusions	84
References.....	85
Chapter 5 Applying VIGS to multi-temporal satellite image for identification of kuroko-type ore deposits	87

5.1.	Introduction	87
5.2.	Study area and geologic setting.....	88
5.3.	Methods.....	94
5.3.1.	Satellite images	94
5.3.2.	Land-cover information and geological datasets	95
5.3.3.	Calculation of the VIs	97
5.3.4.	Image enhancement methods.....	97
5.4.	Results and discussion.....	99
5.4.1.	Temporal change in vegetation index.....	99
5.4.2.	Spatial characterization of vegetation anomaly	102
5.4.3.	Correlating vegetation anomaly with ore deposits potential map.....	104
5.5.	Discussion	110
5.6.	Conclusions	111
	References.....	112
	Chapter 6 Detection of hydrothermal alteration zones in a dense vegetated area by directed principal component analysis.....	115
6.1.	Introduction	115
6.2.	Study location and geologic setting	117
6.3.	Materials and methods	121
6.3.1.	Satellite image data.....	121
6.3.2.	Ground-truth data.....	122
6.3.3.	DPCA and GIS-based analysis	123
6.4.	Results and Discussion.....	126
6.4.1.	Petrographic and spectroscopy analyses.....	126
6.4.2.	Selection of band ratios and DPCA results.....	130
6.5.	Conclusions	135
	References.....	136
	Chapter 7 Summary and future works	139
7.1.	Summary	139
7.2.	Future works.....	143
	List of associated publications and presentations	146

List of Figures

Fig. 1.1. Vegetation condition (light to dark green color) for the entire world based on the normalized difference vegetation index.....	2
Fig. 1.2. Illustration of plant growth in a mineralization area, modified from Sabins (1999).....	5
Fig. 1.3. Atmospheric transmission of electromagnetic waves (Sabins, 1997).....	7
Fig. 1.4. Typical reflectance curve of green vegetation with the main factors that affecting the signature.....	7
Fig. 1.5. Changes in spectral pattern for plants undergoing vegetation stress caused by metal-enriched soils used in a GBRS study (Sabins, 1999).....	8
Fig. 1.6. General methodology of GBRS study.....	9
Fig. 1.7. Locations of study (a) in Indonesia and (b) in Japan.....	10
Fig. 2.1. Growth of Japanese mustard spinach (<i>Brassica rapa</i> var. <i>perviridis</i>) in metal-contaminated soil and normal soil in a experimental room..	24
Fig. 2.2. Measurements of (a) reflectance spectra using ASD Fieldspec3 and (b) total chlorophyll using an AtLeaf chlorophyll meter under laboratory conditions.....	26
Fig. 2.3. Comparison of NDVI and VIGS values using reflectance data from (a) Horler et al. (1980) and (b) Sridhar et al. (2007)..	30
Fig. 2.4. Difference in growth of Japanese mustard spinach with metal content level in soils (L = low, M = medium, and H = high)..	31
Fig. 2.5. Changes in total chlorophyll content of leaves with metal content and days since sowing.....	32
Fig. 2.6. Typical reflectance spectra of Japanese mustard spinach in normal soils (reference) and different levels of Cd-contaminated soils.	32

Fig. 2.7. Average reflectances (X symbols) measured between 60 and 80 elapsed days for each metal and content level, converted to reflectances in Landsat bands (visible B1–B3, NIR B4, and SWIR B5 and B7)..	33
Fig. 2.8. Schematic of a leaf cross section, showing the interaction between the optical incident energy and leaf structure after Buschmann & Nagel (1993).	34
Fig. 2.9. Comparison of NDVI and VIGS change with metal contents and days since sowing...	35
Fig. 2.10. SEM photomicrographs showing the effect of metal absorption on stomatal closure.	37
Fig. 2.11. Schematic point location on the leaf surface of an SEM-EDX analysis and semi-quantitative Cu element distribution.	37
Fig. 2.12. Typical feature of a spectral response curve in the VNIR region indicates the red edge region found in this study.	39
Fig. 3.1. Location of study area in central Sumatra, sampling sites of geochemical data, and mineral occurrences superimposed on sub-scene of true-color composited Landsat ETM+ image acquired on 15 August 2002.	46
Fig. 3.2. Simplified geological map of the study area (after Kusnama et al., 1992; Rosidi et al., 1996; Simandjuntak et al., 1994; Suwarna et al., 1992).	47
Fig. 3.3. Productivity map of aquifers (near-surface permeability for groundwater flow) superimposed on fault and river distributions, following a hydrogeological map of Indonesia (Setiawan et al., 2013; Sukiban, 2005; Yudhanagara, 2005; Zahirdin & Hendra, 1982).	50
Fig. 3.4. Land cover map of plant formations and other categories produced by the maximum likelihood supervised classification of a Landsat ETM+ image.	55
Fig. 3.5. Biplot scores of F1-F2 and F2-F3 obtained from PCA analysis.	57

Fig. 3.6. A schematic spatial overview of the average reflectance value using a circular area of influence.....	58
Fig. 3.7. Performance of the correlations of the metal contents (Cu, Zn, Ni, and K) and PLS model.....	62
Fig. 4.1. Histograms and Q-Q plots of log-transformed contents of Cu, Pb, and Zn at sampling sites.	67
Fig. 4.2. Flow chart showing the research methodology.	70
Fig. 4.3. Experimental semivariograms of log-transformed Cu, Pb, and Zn content data and approximation with the spherical model. Cu and Pb data are along the minor axes.	71
Fig. 4.4. Distributions of metal contents estimated by ordinary kriging (OK) for Cu and Pb and simple kriging (SK) for Zn.	72
Fig. 4.5. C-A models of kriged metal contents in Fig. 4.4 and three segments for approximating the curves.	73
Fig. 4.6. Distributions of low, medium, and high content categories defined by C-A models in Fig. 4.5.	73
Fig. 4.8. Changes in NDVI (blue) and VIGS (red) for land-cover types, shown by averages (×) and standard deviations (bars above and below the average).....	75
Fig. 4.9. Relationships of average NDVI and VIGS with (a) elevation, (b) slope gradient, and (c) slope aspect for three natural forest types.....	77
Fig. 4.10. Relationships of NDVI and VIGS of primary forest with (a) geological units and (b) three categories of aquifer productivity, shown as box plots.....	78
Fig. 4.11. Comparison of average NDVI and VIGS for each metal content category.	81

Fig. 4.12. Spatial characterization of density of VIGS anomaly values (greater than mean + standard deviation) with metal content.....	83
Fig. 5.1. Map of the known ore deposit locations in the Hokuroku district, northern Japan.....	88
Fig. 5.2. Surface geological and Miocene sedimentary basin map of the study area	91
Fig. 5.3. Map of the land cover generated by the Japan Aerospace Exploration Agency (JAXA) that is superimposed with the ASTER GDEM shaded relief.....	95
Fig. 5.4. Field photographs showing typical forest cover and outcrops.	96
Fig. 5.5. Workflow of image and data analyses.....	99
Fig. 5.6. Forest type spatial distribution according to the elevation and multi-temporal data....	101
Fig. 5.7. (a) Comparison of NDVI and VIGS of the five images and (b) Histogram of the NDVI and VIGS for multi-temporal images.	102
Fig. 5.8. Semivariogram of the ratio (mean/ standard deviation) of VIGS values	103
Fig. 5.9. Anomaly intensity images and image enhancement.	104
Fig. 5.10. Map of vegetation anomaly.....	105
Fig. 5.11. Simplified division and facies map of the study area modified after a digital geological map (Wakitawa et al., 2009).....	106
Fig. 5.12. Residual gravity map produced from the residual analysis.....	107
Fig. 5.13. Map of ore exploration index using multivariate regression analysis (Suzuki, 2003) overlaid with the possible ring structures (Kouda & Koide, 1978).....	108
Fig. 5.14. Histograms of geo-properties classified by vegetation (deciduous and evergreen types) anomaly classes.....	109
Fig. 6.1. Study location in Pongkor, West Java province, Indonesia, superimposed on an ASTER image.....	117

Fig. 6.2. (a) Location of the study site, Pongkor mine and (b) regional geological map with schematic cross section (A-B) showing the main ore veins of the Pongkor deposits.....	119
Fig. 6.3. Alteration map of the Pongkor region modified from Basuki et al. (1994).	120
Fig. 6.4. Simplified longitudinal section of the hydrothermal alteration of Cikoret and Ciurug Utara (Syafrizal et al., 2007).....	121
Fig. 6.5. Field photographs show (a) quartz vein, (b) weathered quartz vein with some manganese-oxides, (c) exposed pyroclastic soils, and (d) altered kaolinite with an abundance of highly oxidized pyrite.	122
Fig. 6.6. Schematic representation of the DPC analysis (Fraser & Green, 1987).	124
Fig. 6.7. Workflow of the image processing and interpretation.	126
Fig. 6.8. (a) Microphotograph of a quartz vein showing mostly coarse-grained quartz layering with microgranule quartz. (b) Altered tuff litic formed by fragments of andesitic, quartzitic, plagioclase, clay and opaque minerals in a polished section.	127
Fig. 6.9. Typical spectral analysis results for (a) rock and (b) soil samples.....	129
Fig. 6.10. The spectral plots for key minerals end-members that can be related to the type of argillic and propylitic alterations from the USGS and JPL spectral library.	129
Fig. 6.11. Plots of the reflectance spectra of typical hydrothermally altered minerals (propylitic and argillic alterations) and vegetation. The reflectances are at the ASTER bands.	131
Fig. 6.12. (a) True-color bands 3, 2, and 1 in RGB composition compared with (b-f) the mineral images in 8-bit color from the DPCA and GIS-based analysis can be used as an indicator of hydrothermal alteration zones.....	133

List of Tables

Table 1.1. Electromagnetic spectrum.....	7
Table 1.2. The methods, purposes, and instruments used in this study	12
Table 1.3. List of satellite imagery, geochemical data, and others supporting data used in this research	13
Table 1.4. Bands, wavelength, resolution, and description for Landsat ETM+ data.....	14
Table 1.5. Bands, wavelength, resolution, and description for ASTER data	14
Table 2.1. Essential elements for higher-order plants (Salisbury & Ross, 1992).....	21
Table 2.2. Metal toxicity characteristics in plants	22
Table 2.3. Changes in reflectances in vegetation growth around mineral deposits from metal absorption.....	23
Table 3.1. Lithological summary of the study area	49
Table 3.2. Descriptive statistics from 282 data points; metal unit in ppm, except for Fe in %	51
Table 3.3. Pearson correlation coefficients between the element content and reflectance of the Landsat ETM+ band at the pixel corresponding with the sample point (n = 201)	59
Table 3.4. Pearson correlation coefficient between the element content and reflectance of Landsat ETM+ band for the selected samples located in the selected area	60
Table 3.5. Mean reflectance values in Landsat ETM+ bands with different metal concentrations	61
Table 4.1. Semivariogram models and parameters of Cu, Pb and Zn content data.....	71
Table 4.2. onditions of VI control factors for selecting domain to correlate VI values with soil metal content in study area	79

Table 4.3. Average reflectances of Landsat ETM+ bands after atmospheric and topographic corrections (B1–B5 and B7) and area for each metal content category	80
Table 5.1. Major ore deposits in the Hokuroku district and their specification.....	92
Table 5.2. Detailed description of the Landsat 7 ETM+ images used in this study	94
Table 6.1. Common absorption features in the SWIR region related to the type of minerals	128
Table 6.2. List of selected bands (b_i and b_j) that used in the normalized difference-based ratio $((b_i - b_j) / (b_i + b_j))$ as the input images for DPCA	131

Chapter 1

Introduction

1.1. Background of study

The consumption of mineral resources (base, precious, or minor metals, and rare earth elements), conventional hydrocarbon energy resources (oil, natural gas, and coal), and non-conventional hydrocarbons (oil shale) has experienced rapid growth in many countries in recent years. This has led to a higher demand for these resources and has resulted in considerable needs for innovation in natural resource exploration.

Remote sensing is one of the most popular tools for indirect exploration and is commonly used during the prospecting phase as it can provide a rapid assessment at a low cost and with minimal risk. This technique, in both its optic and radar applications, has been growing in line with technological advances. Remote sensing satellites with onboard optical sensors have been effectively applied in geology to identify minerals and rocks, produce geological maps, and detect manifestations of mineral and hydrocarbon deposits and groundwater outflows by the reflectance and emissivity spectral characteristics of Earth surface materials (Koide & Koike, 2012; Sabins, 1999; van der Meer et al., 2012). Geometrical features appearing on satellite imagery have been used to characterize large geological structures such as folds and faults (Fernandes et al., 2005; Fraser et al., 1997) and estimate the distribution, direction, and size of fracture systems (Koike & Ichikawa, 2006; Koike et al., 1998).

As for spectral applications, the validity of remote sensing is limited to arid and semiarid areas where vegetation is sparse or absent. Because the reflectance spectra of vegetation conceal the spectra of underlying soils and rocks, vegetation is the most critical barrier to geological

identification and mapping in the application of remote sensing. Unfortunately, the climate most of the world is temperate to humid climates which often leads to either intense weathering or heavy vegetation growth (Fig. 1.1). Under these conditions, optical remote sensing applications for resource exploration become more challenging. Therefore, the exploration and the potential assessment of mineral deposits by optical remote sensing could be difficult in thickly vegetated areas.

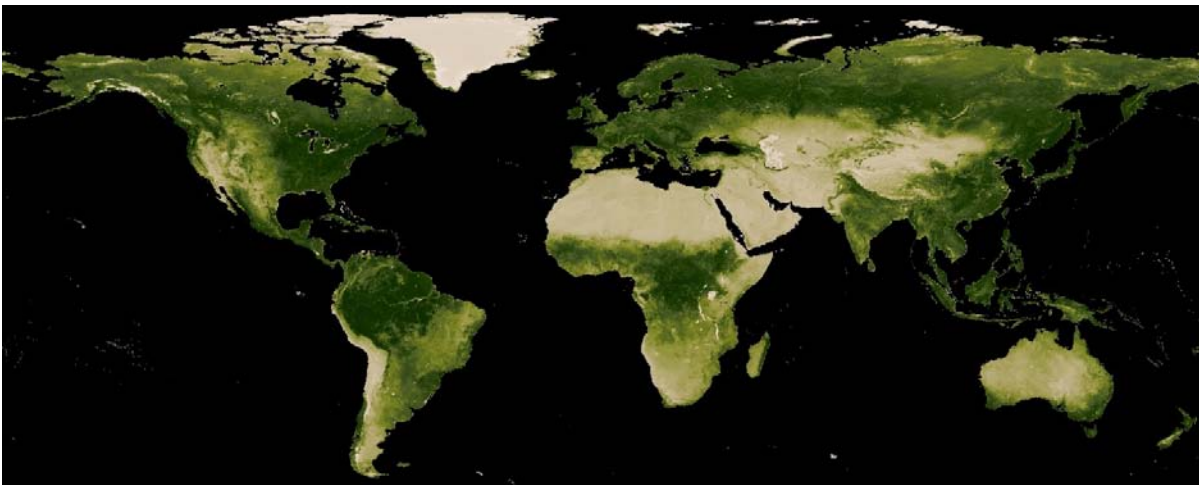


Fig. 1.1. Vegetation condition (light to dark green color) for the entire world based on the normalized difference vegetation index (NDVI) (1 month – Terra MODIS) on August 2014. Images by Reto Stockli, NASA's Earth Observatory Group, using data provided by the MODIS Land Science Team (<http://neo.sci.gsfc.nasa.gov>).

However, vegetation can be an essential part of geological researches. The scientific study of the relationship between vegetation and geological condition is called geobotany. Traditional geobotany is an extension of geochemistry and biogeochemistry, resulting in a field able to fully examine botanical phenomena, including the nature and distribution of plant

communities, the ways in which plants indicate the presence of mineral deposits, and the detection of morphologic changes in plants related to geological influence (Sabins, 1999).

Traditional geobotany mainly investigates how the nature and distribution of plants can be affected by environmental and geological conditions, in addition to how vegetation conditions may indicate the condition of the rock beneath. In recent years, the integration of geobotany with remote sensing technology has allowed for the study of spectral response patterns relating to morphological and physiological changes resulting from the absorption of metals (the term metal in this study refers to heavy metals) in vegetation (Bruce & Hornsby, 1987). However, vegetation in nature is affected by complex interactions from both biotic and abiotic factors.

Recently, several kinds of optical remote sensing images have become available, in both multispectral (Landsat, ASTER, EO1-ALI, MODIS) and hyperspectral (EO1-Hyperion) forms. Although their spatial resolutions have increased to 15–250 m per pixel; pixels at this resolution display several materials (vegetation, soil, rocks, water, and artificial materials), and the reflectance spectra are a mixture of the spectra of all end-members. Several studies have tried to separate or remove vegetation spectra from non-vegetation components by spectral unmixing or directed principal component analysis (Asner & Lobell, 2000; Carranza & Hale, 2002; Fraser & Green, 1987; Guerschman et al., 2015), and by the forced invariance method for vegetation suppression, without considering non-vegetation components spectra (Crippen & Blom, 2001; Yu et al., 2011).

It has been suggested that vegetation absorbs nutrients from the substrate, including metals from the soil, which affects the spectral response. Although initial research has been conducted on the relationship between metal deposits and the existence of vegetation anomalies above them, no detailed results have yet been found, and the mechanism by which metals

generate vegetation has also not yet been clarified. This research seeks to implement geobotanical remote sensing for analyzing the spectral response in vegetation under metal stress, and also addresses how to improve and optimize image enhancement methods in order to solve the problem of spectral mixtures.

1.2. Objectives

The main objectives of this research can be summarized as follows:

1. To clarify the change in reflectance spectra of plants due to varying metal concentrations in the soil and presence of different types of metals.
2. To understand and interpret mechanisms caused by metal absorption in plants that affects the spectral response.
3. To determine which factors should be considered when using spectra attributes in order to determine the vegetation stress caused by geochemical anomalies.
4. To develop an accurate methodology for correlating vegetation spectral responses with vegetation stress caused by metals, as an indicator of mineral occurrence.
5. To optimize image enhancement methods in a vegetated terrain in order to detect mineralization areas.

Moreover, the general objective of this research is to develop unconventional methods in order to apply remote detection of geological features that relate to the occurrence of mineral deposits in heavily vegetated areas, utilizing the spectral response of vegetation. This study integrates laboratory experiments and case studies in several locations known to contain mineral deposits that were once covered by dense vegetation. The laboratory experiments were conducted to clarify and analyze the responses of plants grown in soils contaminated by metals.

Through case studies, the vegetation spectral response derived from satellite imagery was analyzed.

1.3. Geobotanical Remote Sensing (GBRS)

As above mentioned, geobotany is based on the idea that plants can express the geological condition of the area that they are growing in, and traditionally maintains that particular plants are associated with certain stratigraphic units or geological formations. Furthermore, biogeochemical prospecting has found that the metal content of plants growing in areas of mineralization is higher than in plants grown under normal conditions (Fig. 1.2) (Sabins, 1999). This relationship between metal content and vegetation is the basis for biogeochemical and geobotanical prospecting methods.

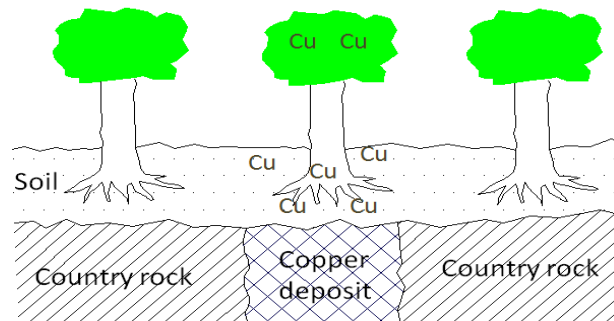


Fig. 1.2. Illustration of plant growth in a mineralization area, modified from Sabins (1999).

General criteria for geobotany relating to mineral exploration can be summarized as follows (Bruce & Hornsby, 1987; Sabins, 1999):

1. Indicator communities and plants.

There are certain plants that grow well in areas of mineralization, although they may be sterile, unproductive, and have different characteristics compared to normal specimens.

This condition is possible since some plants have adapted to natural stress conditions, in this case, the mineralization area.

2. Physiological changes as stress indicators.

Vegetation responses to the absorption of metals are known as “vegetation stress” and can present as a decline in grow rates, photosynthetic activity, and chlorophyll content (Chapin, 1991; Woolhouse, 1983). These symptoms often occur because heavy metals inhibit the plant’s absorption of water from the soil, although they may also result from salinity, drought, disease, nutrient deficiency, and senescence.

Remote sensing study analyzes the interaction characteristic between object features and electromagnetic energy, recorded in the microwave, infrared, visible to the long wavelength of the ultraviolet region (Sabins, 1997) (Fig. 1.3). This study specifically uses only optical remote sensing; visible to shortwave infrared region. In using GBRS, it is important to understand the spectra pattern of vegetation (in particular, green vegetation). General spectral curves of most vegetation types are remarkably similar. The pattern itself, a response to electromagnetic waves irradiated from the sun, can be divided into three main wavelength ranges, as shown in (Fig. 1.4). The visible range (0.40–0.70 μm) shows low reflectance values due to the absorption by photosynthetic pigments, primarily chlorophylls, as well as carotenoids, xanthophylls, and anthocyanins. In the near infrared (NIR) range (0.70–1.40 μm), reflectance values increase remarkably where there are no strong absorption features, because the internal cellular structure of leaves promotes scattering of radiation within this range. In the third range, the shortwave infrared (SWIR) region (1.40–2.5 μm), the variable reflectance is mainly related to water absorption or leaf moisture.

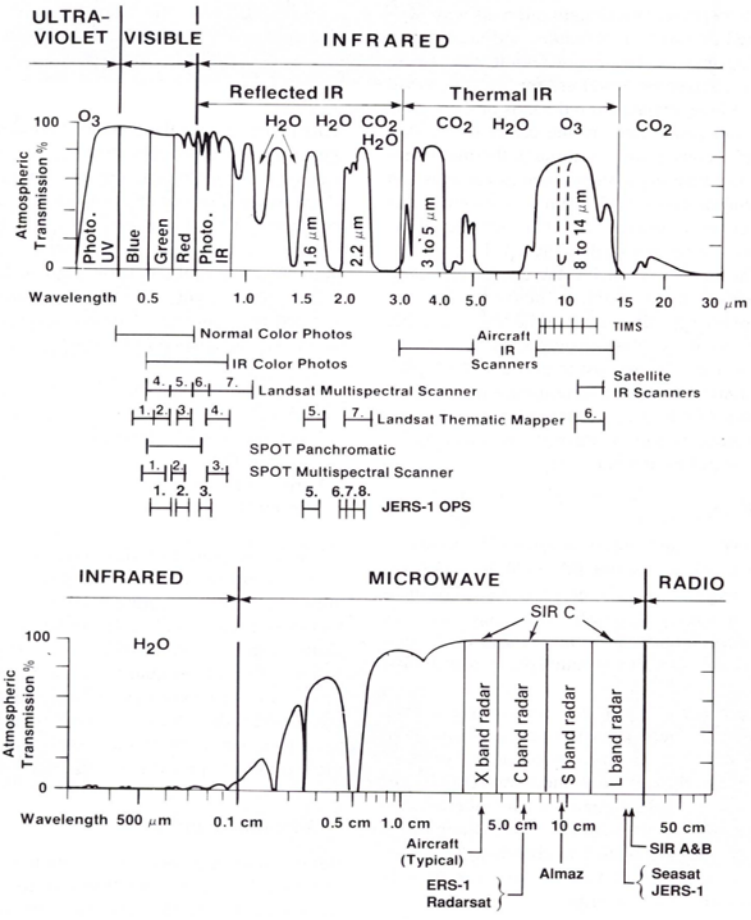


Fig. 1.3. Atmospheric transmission of electromagnetic waves (Sabins, 1997).

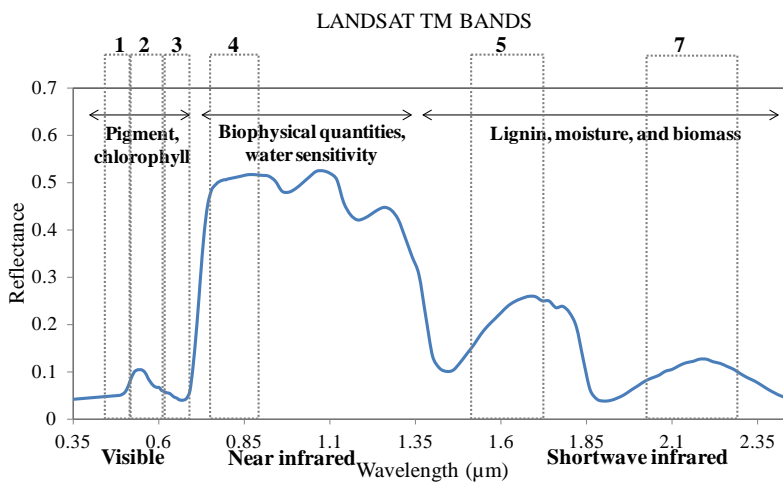


Fig. 1.4. Typical reflectance curve of green vegetation with the main factors that affecting the signature.

One key factor of using GBRS for mineral exploration is the existence of unusual vegetation conditions in mineralized areas, which can be identified from the reflectance spectral pattern. This idea has been used since the early stages of satellite remote sensing, and effects of metal absorption by plants on the reflectance spectra have been investigated (Horler et al., 1980; Rencz & Watson, 1989; Sabins, 1999). Additionally, an understanding of the relationship between plant communities and metal content in soils is essential because the spectral response of plants to the absorption of metals from the substrate materials forms the basis for GBRS (Fig. 1.5) (Beswick et al., 1991; Bruce & Hornsby, 1987).

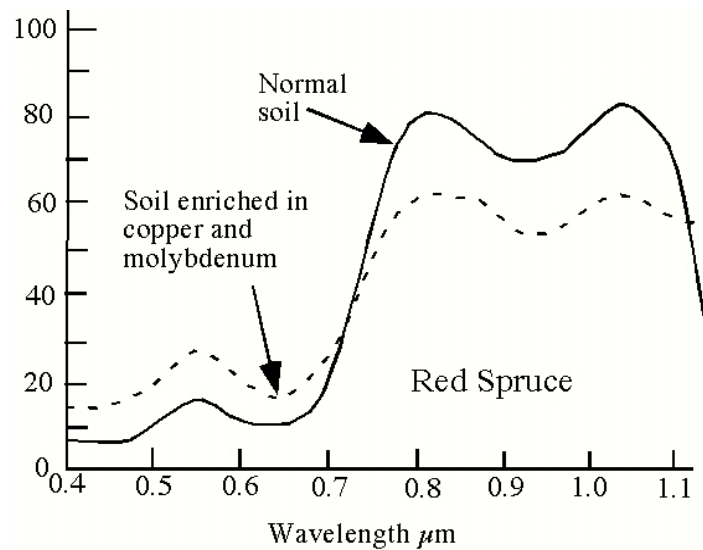


Fig. 1.5. Changes in spectral pattern for plants undergoing vegetation stress caused by metal-enriched soils used in a GBRS study (Sabins, 1999).

The general methodology for GBRS study, as shown in Fig. 1.6, involves two general stages. First, from a geobotanical perspective, an understanding must be established of the internal and external factors influencing vegetation condition. Among the internal factors is plant physiology in this cases it is worth noting that the response that vegetation with metal varies

depending on its concentration (Barceló & Poschenrieder, 1990). External factors that may affect vegetation conditions include geological factors, topography, and environmental conditions. The second stage relates to remote sensing analysis, and includes image and spectra analysis. It is necessary to consider all information from the satellite imagery (e.g., image acquisition in the spring or fall is the most sensitive to vegetation conditions). Image correction and spectra analysis occur at the preprocessing and processing stages.

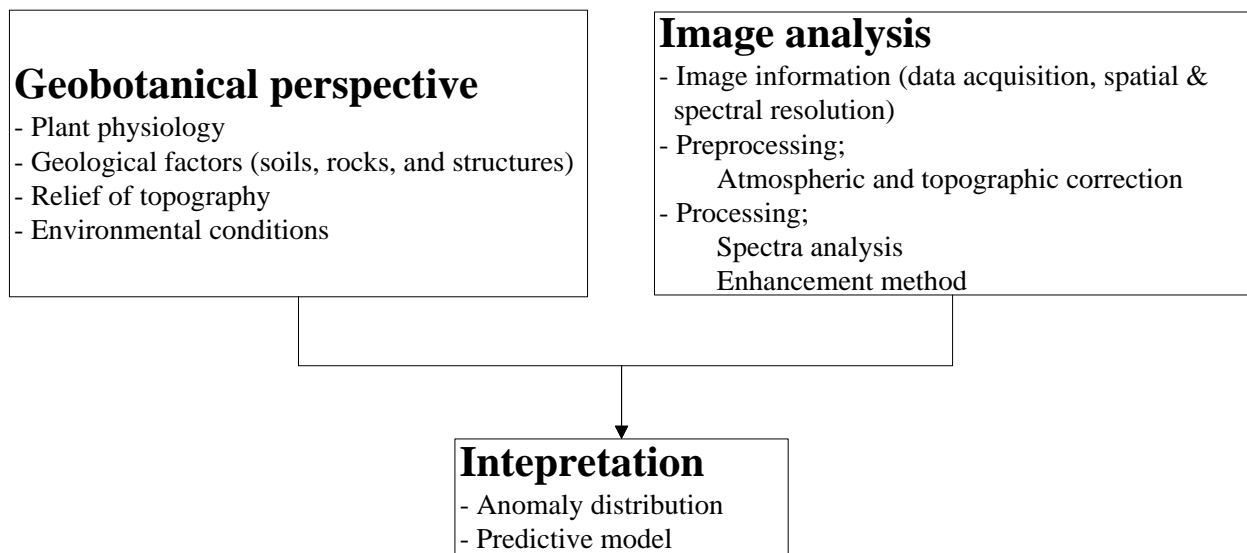


Fig. 1.6. General methodology of GBRs study.

1.4. Study area

This research consists of laboratory experiments and case studies. The case studies were conducted in three geographic areas: the Jambi region, Pongkor region, and Hokuroku region. Jambi and Pongkor are located in Sumatra and Java, Indonesia, respectively (Fig. 1.7a), and the Hokuroku region is in northern Japan (Fig. 1.7b).

The Jambi region features copper mineralization, while gold is present in Pongkor. Both locations were selected based on the availability of geo-exploration datasets, including geochemical data and mining activity. A set of geochemical systematic data in the Jambi region was used as ground truth data and to analyze of metal distribution. The Pongkor deposit is one of the most famous gold deposits in Indonesia and is home to an active mine owned by PT. Antam, an Indonesian gold mining company. Dense tropical rain forest vegetation covers both of these locations. The Hokuroku region in Japan is one of the world’s most famous sites of Volcanogenic Massive Sulfide (VMS) ore deposits of the kuroko (black ore) type. Hokuroku is also largely covered by dense vegetation, consisting mainly of deciduous and evergreen forest.

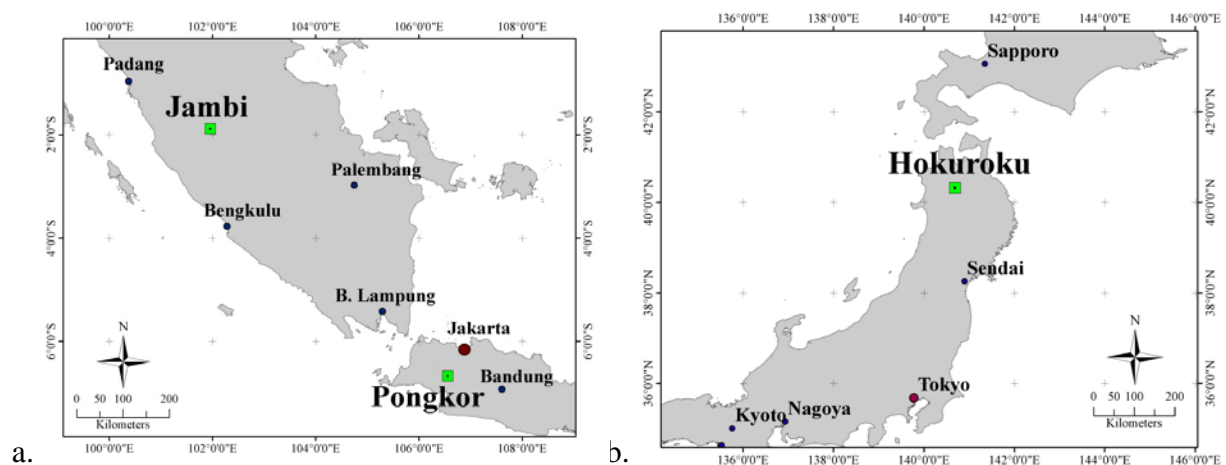


Fig. 1.7. Locations of study (a) in Indonesia and (b) in Japan.

1.5. Datasets

The data used in this research can mainly be divided into primary and secondary data. The primary data were taken during field surveys and laboratory analyses. The secondary data mainly originated from satellite imagery, a set of geochemical data quoted from the report of a regional geochemical investigation from a government agency, and other supporting data, such

as digital elevation models (DEMs), geological data, and information about land use and vegetation types.

1.5.1. Field survey and laboratory experiments

The field surveys were performed to allow for geological observation, ground checking, assessing vegetation condition growth in the study area, and collecting samples. This collection of ground truth data will be used to calibrate remote sensing data and aid in the interpretation of remotely sensed results. The collected samples include rocks and soil. The chip sampling method was used for collecting rock, while soil samples were taken from a depth of 5–20 cm below the surface.

A two-part laboratory analysis was performed on the samples taken from field surveys, and standardized laboratory experiments were performed in which the effect of heavy metal contamination in cultivated plant samples was studied. The standardized experiments, which are described in Chapter 2, involved cultivating Japanese mustard spinach (*Brassica rapa* var. *perviridis*) in laboratory conditions. The aim of this study was to clarify the relationship between vegetation response and metal contamination by analyzing the response of vegetation grown in soils contaminated by selected metals. This part is indispensable to identifying vegetation anomalies caused by metal contamination. The details of the methods, purposes, and instruments used during laboratory works as listed in Table 1.1.

Table 1.1. The methods, purposes, and instruments used in this study.

Method	Purpose	Instrument
X-ray diffraction (XRD)	Mineral composition	XRD 7000 Shimadzu
X-ray fluorescence (XRF)	Chemical element composition	Delta handheld XRF analyzer
Petrographic analysis	Morphology, mineral composition and their distribution	Nikon E200 polarization microscope
Spectroscopic analysis	Reflectance measurement	FieldSpec3 ASD
	Total chlorophyll measurement	AtLeaf
Scanning electron microscope with energy-dispersive X-ray (SEM EDX)	Morphology and elemental distribution	JEOL JSM-6150A

1.5.2. Satellite imagery and others supporting data

Generally, there are two kinds of secondary data used in this research. The first includes multispectral satellite imagery, which covers the visible to shortwave infrared spectrum (400–2,500 nm). The second consists of data points and vectors, which mainly belong to a set of geological data. In addition, I used a range of supporting data that have been collected from several previously published sources. Summaries of all of the satellite imagery, geological data, and other supporting data sources used in this research can be viewed in Table 1.2.

The optical satellite imagery referenced in this study uses multispectral data taken from Landsat and the Advanced Spaceborne Thermal Emission and Reflection Radiometer (ASTER) images. The Landsat program is a joint effort between the United States Geological Survey (USGS) and the National Aeronautics and Space Administration (NASA), and has a long history of acquiring satellite imagery. Landsat images have been applied to regional planning, as well as agricultural, environmental, and geological purposes. There are currently 8 Landsat series, the newest one being Landsat 8, which launched on February 11, 2013. In this study, I used the

Landsat Enhanced Thematic Mapper Plus (ETM+), the 7th generation of the Landsat series, which first launched on April 5, 1999, and has remained active up until the present day. Landsat images consist of 8 spectral bands, with a spatial resolution of 30 m for bands 1–7 and 15 m for band 8 (panchromatic) (Table 1.3). The operation and distribution of Landsat is held by the USGS, and there are no restrictions on Landsat data available for download at <http://glovis.usgs.gov>.

Table 1.2. List of satellite imagery, geochemical data, and others supporting data used in this research.

Data	Type	Scale	Source
Landsat	Raster	30 m	http://glovis.usgs.gov
ASTER	Raster	15–30 m	http://gds.ersdac.jspacesystems.or.jp/?lang=en
DEM	Raster	30 m, 90 m	http://gdem.ersdac.jspacesystems.or.jp/ http://srtm.csi.cgiar.org
Geological map	Vector	1:250,000	Japan Geological Agency and Indonesia Geological Agency
Vegetation map	Raster Vector	90 m 1:1,000,000 1:250,000	Land-cover map generated by Japan Aerospace Exploration Agency (JAXA) http://www.eorc.jaxa.jp/ALOS/lulc/lulc_jindex.html Central Sumatra vegetation map (Blasco, Laumonier, Purnadjaja, & Setiabudhi, 1986) Indonesia land-cover map by National Coordinating Agency for Surveys and Mapping
Geochemical datasets	Points	1 points / 10 km ²	Joint cooperation of Indonesia Geological Agency and British Geological Survey (British Geological Survey, 2007)
Gravity datasets	Points, vector, and raster		Gravity database of Japan, Geological Survey of Japan

Table 1.3. Bands, wavelength, resolution, and description for Landsat ETM+ data.

Landsat ETM+ Band	Wavelength (micrometers)	Resolution (m)	Description
Band 1	0.45-0.52	30	Visible blue
Band 2	0.52-0.60	30	Visible green
Band 3	0.63-0.69	30	Visible red
Band 4	0.77-0.90	30	Near infrared
Band 5	1.55-1.75	30	Shortwave infrared
Band 6	10.40-12.50	60	Thermal infrared
Band 7	2.09-2.35	30	Shortwave infrared
Band 8	0.52-0.90	15	Panchromatic

Table 1.4. Bands, wavelength, resolution, and description for ASTER data.

ASTER band	Label	Wavelength (micrometers)	Resolution (m)	Nadir or Backward	Description
B1	VNIR_Band1	0.520–0.600	15	Nadir	Visible green
B2	VNIR_Band2	0.630–0.690	15	Nadir	Visible red
B3	VNIR_Band3	0.760–0.860	15	Nadir	Near infrared
B3B	VNIR_Band3	0.760–0.860	15	Backward	
B4	SWIR_Band4	1.600–1.700	30	Nadir	Shortwave infrared
B5	SWIR_Band5	2.145–2.185	30	Nadir	
B6	SWIR_Band6	2.185–2.225	30	Nadir	
B7	SWIR_Band7	2.235–2.285	30	Nadir	
B8	SWIR_Band8	2.295–2.365	30	Nadir	
B9	SWIR_Band9	2.360–2.430	30	Nadir	
B10	TIR_Band10	8.125–8.475	90	Nadir	
B11	TIR_Band11	8.475–8.825	90	Nadir	
B12	TIR_Band12	8.925–9.275	90	Nadir	
B13	TIR_Band13	10.250–10.950	90	Nadir	
B14	TIR_Band14	10.950–11.650	90	Nadir	

Another source of multispectral data used in this research is ASTER imagery. The ASTER is an imaging instrument onboard the Terra satellite and is a cooperative effort courtesy of NASA; Japan's Ministry of Economy, Trade, and Industry (METI); and Japan Space Systems (J-spacesystems). Although there are 14 different bands of the electromagnetic spectrum, ranging from visible to thermal infrared light (Table 1.4), this study uses only those that fall between visible and shortwave infrared, and does not include thermal and panchromatic images.

I also used a digital elevation model (DEM) taken from the Shuttle Radar Topography Mission (SRTM) and the ASTER Global Digital Elevation Model (ASTER GDEM). The SRTM DEMs, a product of the United States National Aeronautics and Space Administration (NASA), have a resolution of 90 m at the equator and have been processed to fill data voids. The ASTER GDEM (about 30 m resolution) is a product of the Ministry of Economy, Trade, and Industry (METI) of Japan and NASA. The DEM data was used at the stage preprocessing image in order to calculate topographic correction. In addition, several forms of data including geochemical data, geological maps, a land use map, and a vegetation map have also been collected from different sources – primarily government agencies.

1.6. Structure of dissertation

This dissertation consists of the following seven chapters in which Chapter 1 is an introduction, Chapter 2 is a laboratory experiment, Chapter 3 is a case study using reflectance derived from satellite image, Chapter 4 and 5 are case studies using VIGS, Chapter 6 is a case study for spectral mixture problem, and Chapter 7 is a conclusion. Details of each chapter are explained as follows.

Chapter 1 provides an introduction to the research. It contains several sub-chapters, which detail the background of the study and explain the objectives. I also briefly describe GBRS, which is the main topic of the research. This chapter also introduces those study areas in which the research takes place and presents the datasets that I use, including laboratory experiments.

Chapter 2 discusses the results of a standardized laboratory experiment involving the cultivation of Japanese mustard spinach (*Brassica rapa* var. *perviridis*) under laboratory conditions. The goal of this study is to clarify the change in reflectance spectra of plants with different metal concentrations in soil and with different types of metal and developed a new vegetation index, the Vegetation Index considering Greenness and Shortwave infrared (VIGS), based on experimental results.

Chapter 3 analyzes the relationship between geochemical data and spectral attributes by using a multispectral remote sensing image. The possibility of using reflectance values derived from multispectral satellite imagery to detect geochemically enriched zones in dense vegetation areas is demonstrated.

Chapter 4 evaluates the effectiveness of VIGS derived from satellite image (Landsat ETM+) by correlating metal contents categories in the top layer concentration distribution, as analyzed through a kriging interpolation and the C-A model. Moreover, this chapter also demonstrated that the GBRS study requires an understanding of the physical evaluation in terms of a correlation with vegetation characteristics.

Chapter 5 proposes novel combine method for implementing VIGS described in the previous chapter by using multitemporal Landsat ETM+ data to detect vegetation anomalies and demonstrate the relation to ore deposits distributions by comparing with geo-exploration datasets and forest type distributions in the Hokuroku region, Akita Prefecture, Japan.

Chapter 6 discusses another approach of GBRS to detect the hydrothermal mineralization zones of dense vegetated areas. This method involves the optimization of the combinations band ratio, principal component analysis, geographic information system (GIS)-based analysis by using an ASTER image.

Chapter 7 offers concluding remarks, including primary results from all chapters. I also provide a list of proposed future works related to this study, which will help further develop GBRS techniques.

References

- Asner, G. P., & Lobell, D. B. (2000). A biogeophysical approach for automated SWIR unmixing of soils and vegetation. *Remote Sensing of Environment*, 74(1), 99–112. [http://doi.org/10.1016/S0034-4257\(00\)00126-7](http://doi.org/10.1016/S0034-4257(00)00126-7)
- Barceló, J., & Poschenrieder, C. (1990). Plant water relations as affected by heavy metal stress: A review. *Journal of Plant Nutrition*. <http://doi.org/10.1080/01904169009364057>
- Beswick, A. E., Beckett, P. J., Courtin, G. M., & Tapper, G. O. (1991). Evaluation of geobotanical remote sensing as an aid to mineral exploration in Northerneastern Ontario. Ontario Geological Survey.
- Bruce, B., & Hornsby, J. K. (1987). A Canadian perspective on the application of satellite remote sensing to regional geobotany. *Geocarto International*. <http://doi.org/10.1080/10106048709354108>
- Carranza, E. J. M., & Hale, M. (2002). Mineral imaging with Landsat Thematic Mapper data for hydrothermal alteration mapping in heavily vegetated terrane. *International Journal of Remote Sensing*. <http://doi.org/10.1080/01431160110115014>
- Chapin, F. (1991). Integrated responses of plants to stress. *BioScience*, 41(1), 29–36. <http://doi.org/10.2307/1311538>

- Crippen, R. E., & Blom, R. G. (2001). Unveiling the Lithology of Vegetated Terrains in Remotely Sensed Imagery. *American Society for Photogrammetry and Remote Sensing Proceedings*, 91109, 935–943.
- Fernandes da Silva, P. C., Cripps, J. C., & Wise, S. M. (2005). The use of Remote Sensing techniques and empirical tectonic models for inference of geological structures: Bridging from regional to local scales. *Remote Sensing of Environment*, 96(1), 18–36. <http://doi.org/10.1016/j.rse.2005.01.007>
- Fraser, A., Huggins, P., Rees, J., & Cleverly, P. (1997). A satellite remote sensing technique for geological structure horizon mapping. *International Journal of Remote Sensing*, 18(7), 1607–1615. <http://doi.org/10.1080/014311697218313>
- Fraser, S. J., & Green, A. A. (1987). A software defoliant for geological analysis of band ratios. *International Journal of Remote Sensing*, 8(3), 525–532. <http://doi.org/10.1080/01431168708948659>
- Guerschman, J. P., Scarth, P. F., McVicar, T. R., Renzullo, L. J., Malthus, T. J., Stewart, J. B., Jasmine, E. R., & Trevithick, R. (2015). Assessing the effects of site heterogeneity and soil properties when unmixing photosynthetic vegetation, non-photosynthetic vegetation and bare soil fractions from Landsat and MODIS data. *Remote Sensing of Environment*, 161, 12–26. <http://doi.org/10.1016/j.rse.2015.01.021>
- Horler, D. N., Barber, J., & Barringer, A. R. (1980). Effects of heavy metals on the absorbance and reflectance spectra of plants. *International Journal of Remote Sensing*, 1(2), 121–136. <http://doi.org/10.1080/01431168008547550>
- Koide, K., & Koike, K. (2012). Applying vegetation indices to detect high water table zones in humid warm-temperate regions using satellite remote sensing. *International Journal of Applied Earth Observation and Geoinformation*, 19, 88–103. <http://doi.org/10.1016/j.jag.2012.03.017>
- Koike, K., & Ichikawa, Y. (2006). Spatial correlation structures of fracture systems for deriving a scaling law and modeling fracture distributions. *Computers & Geosciences*, 32(8), 1079–1095. <http://doi.org/10.1016/j.cageo.2006.02.013>
- Koike, K., Nagano, S., & Kawaba, K. (1998). Construction and analysis of interpreted fracture planes through combination of satellite-image derived lineaments and digital elevation

- model data. *Computers & Geosciences*, 24(6), 573–583. [http://doi.org/10.1016/S0098-3004\(98\)00021-1](http://doi.org/10.1016/S0098-3004(98)00021-1)
- Laumonier, Y. (1997). *The vegetation and physiography of Sumatra*. (M. J. A. Werger, Ed.). Dordrecht: Springer Netherlands. <http://doi.org/10.1007/978-94-009-0031-8>
- Rencz, A. N., & Watson, G. P. (1989). Biogeochemistry and LANDSAT TM data: Application to gold exploration in northern New Brunswick. *Journal of Geochemical Exploration*, 34(3), 271–284. [http://doi.org/10.1016/0375-6742\(89\)90117-9](http://doi.org/10.1016/0375-6742(89)90117-9)
- Sabins, F. F. (1997). *Remote sensing: principles and interpretation* (3rd edn.). Illinois: Waveland Press, Inc.
- Sabins, F. F. (1999). Remote sensing for mineral exploration. *Ore Geology Reviews*, 14(3-4), 157–183. [http://doi.org/10.1016/S0169-1368\(99\)00007-4](http://doi.org/10.1016/S0169-1368(99)00007-4)
- van der Meer, F. D., van der Werff, H. M. A., van Ruitenbeek, F. J. A., Hecker, C. A., Bakker, W. H., Noomen, M. F., van der Meijde, M., Carranza, E. J. M., de Smeth., J. B., & Woldai, T. (2012). Multi- and hyperspectral geologic remote sensing: A review. *International Journal of Applied Earth Observation and Geoinformation*, 14(1), 112–128. <http://doi.org/10.1016/j.jag.2011.08.002>
- Woolhouse, H. W. (1983). Toxicity and tolerance in the responses of plants to metals. In O. L. Lange, P. S. Nobel, C. B. Osmond, & H. Ziegler (Eds.), *Encyclopedia of Plant Physiology-Physiological Plant Ecology III* (pp. 245–300). Springer Berlin Heidelberg. Retrieved from <http://link.springer.com/10.1007/978-3-642-68153-0>
- Yu, L., Porwal, A., Holden, E.-J., & Dentith, M. C. (2011). Suppression of vegetation in multispectral remote sensing images. *International Journal of Remote Sensing*, 32(22), 7343–7357. <http://doi.org/10.1080/01431161.2010.523726>

Chapter 2

Development of a new vegetation index for detecting vegetation anomalies in metal-contaminated soils

2.1. Introduction

The effect of metals in soil on vegetation has been frequently studied, either in the laboratory setting or under natural field conditions (Slonecker, 2011; Woolhouse, 1983). Assessment of metal contamination has many uses, not only for environmental reasons, such as pollution monitoring and phytoremediation, but also for developing a breakthrough method in mineral exploration technology on vegetated terrain (Boluda et al., 1993; Dunagan et al., 2007; Rosso et al., 2005).

Biogeochemical studies have shown that the effects of metal absorption in plants are usually related to the metabolism of plants. Some metals, such as N, S, P, K, Ca, and Mg, are macronutrients (with a minimum requirement in tissue concentration of 1,000 ppm in dry matter), whereas other metals, such as Zn, Fe, Mn, Cu, Mo, B, Cl, and Ni, are micronutrients (with a concentration in dry tissue of less than 100 ppm) (Salisbury & Ross, 1992). Table 2.1 lists the metal elements essential for most higher-order plants.

However, metal nutrients may have result in impairment of plant metabolism and photosynthesis activity, especially where there is an excess of metals, generally derived from substrate materials (soils or rocks). Metal enrichment in soils can arise from a variety of factors that may be caused by natural conditions (e.g., mineral outcrop/deposits) or anthropogenic events (e.g., industrial processing). Naturally, plants must adapt to their environmental conditions,

including metal exposure, because they are stationary. However, plants respond to metal enrichment using various complex strategies, whether as accumulators or excluders, which affects their growth, biomass accumulation, and visual symptoms (Slonecker, 2011). Table 2.2 lists common symptoms related to metal exposure in plants.

Table 2.1. Essential elements for higher-order plants (Salisbury & Ross, 1992).

Element	Form available to plants	Atomic Wt.	Concentration in dry tissue (ppm)
Mo	MoO_4^{2-}	95.95	0.1
Ni	Ni^{2+}	58.71	?
Cu	Cu^+ , Cu^{2+}	63.54	6
Zn	Zn^{2+}	65.38	20
Mn	Mn^{2+}	54.94	50
B	H_3BO_3	10.82	20
Fe	Fe^{3+} , Fe^{2+}	55.85	100
Cl	Cl^-	35.46	100
S	SO_4^{2-}	32.07	1,000
P	H_2PO_4^- , HPO_4^{2-}	30.98	2,000
Mg	Mg^{2+}	24.32	2,000
Ca	Ca^{2+}	40.08	5,000
K	K^+	39.10	10,000
N	NO_3^- , NH_4^+	14.01	15,000
O	O_2 , H_2O , CO_2	16.00	450,000
C	CO_2	12.01	450,000
H	H_2O	1.01	60,000

In terms of mineral deposit exploration, excess metal enrichment around the deposits may cause changes in the characteristics of endemic plants, which may be a clue to the underlying deposits. Therefore, analysis of stress in vegetation can be a useful indicator for mineral exploration.

Table 2.2. Metal toxicity characteristics in plants, modified from Slonecker (2011) and Woolhouse (1983).

Metal	Metal exposure effects
Copper	Leaf chlorosis, decreased root growth, membrane damage, and reduced leaf biomass
Lead	Inhibited root elongation, stunted growth, chlorosis, purple discoloration
Zinc	Inhibition of root growth, chlorosis, stunted growth
Cadmium	Leaf chlorosis, necrosis, curled leaves, inhibited root elongation
Arsenic	Red or brown necrotic spots on old leaves, reduced growth
Nickel	Leaf chlorosis, necrosis, inhibited root growth, stunted growth
Mercury	Leaf chlorosis, reduced biomass, stunted roots

Spectroscopy analyses related to the effects of metals (in particular, heavy metals) in plants due to vegetation stress conditions can be performed using spectral patterns (Horler et al., 1980; Rencz & Watson, 1989). Metal-induced vegetation stress interferes with chlorophyll activity and inhibits water absorption from soils and the supply to leaves (Barceló & Poschenrieder, 1990). Furthermore, an understanding of the relationship of plant formations to geological conditions and metal content in soils is essential. In the optical region, the wavelength ranges from visible to near infrared (VNIR), 400–1,400 nm, in which the effect of absorbed metal on the reflectance spectra is easy to identify; this approach has been used in geobotanical remote sensing (Boluda et al., 1993; Dunagan et al., 2007; Kooistra et al., 2004). Horler et al. (1980) summarized the change in reflectance spectra in the VNIR regions for general vegetation growth around mineral deposits (Table 2.3).

Table 2.3. Changes in reflectances in vegetation growth around mineral deposits from metal absorption, modified from Horler et al. (1980).

Metals	Reflectance change at a certain wavelength.	Vegetation type
Cu, Mo	Increases at 0.67 μm	<i>Pinus contorta</i>
	Increases at 0.38 – 0.72 μm , decreases at 0.72 – 1.1 μm	<i>Picea rubens</i>
	Increases at 0.38 – 0.72 μm , increases at 0.72 – 1.1 μm	<i>Abies balsamea</i>
Cu	Increases at 0.81 μm , the first derivative of reflectance increases between 0.70 – 0.78 μm	<i>Pinus ponderosa</i>
Pb, Zn	Apparent increase at the 0.68 – 0.90 μm range	<i>Quercus</i> sp.
Mo	Reflectance ratio at 2.22 μm /1.65 μm increases, decreases at 2.22 μm	<i>Pinus pendrosa</i>
	Reflectance ratio at 2.22 μm /1.65 μm increases, increases at 2.22 μm	<i>Juniperus utahensis</i>
Metal sulfide	The first derivative of reflectance changes between 0.70 – 0.78 μm	Conifers

However, this effect has also been observed at longer wavelengths, in shortwave infrared (SWIR) bands of 1,400–2,500 nm as the vegetation stress, and it is likely to be enhanced by combining VNIR and SWIR (Horler et al., 1980; Sridhar et al., 2007). Therefore, it is necessary to thoroughly understand vegetation stress in all regions. In this study, I elaborate the effects of metals on vegetation reflectance at various wavelengths in the VNIR–SWIR region. Although the majority of geobotanical remote sensing studies have focused on the VNIR wavelength, this study concentrated on longer wavelengths via the inclusion of SWIR as well as VNIR.

Given the above background, this chapter is aimed to develop a vegetation index (VI) using the reflectances in several bands from VNIR and SWIR so that the VI is sensitive to vegetation stress by metal absorption. The VI is used to emphasize the change in reflectances at bands selected for estimating the magnitude of stress. For this research, laboratory experiments

were undertaken to clarify the relationship between the metals in soils and the reflectance spectra of a selected plant species. Four types of metals were used for the experiment and to investigate the difference in the VIs with the metal content.

2.2. Materials and methods

2.2.1. Laboratory experiment

The purpose of the laboratory experiment was to clarify the change in reflectance spectra of plants with different metal concentration in soils and with different types of metal. Japanese mustard spinach (*Brassica rapa* var. *perviridis*) was selected for the experiment because of its relatively short lifetime (approximately 2–4 months) and ease of cultivation from seed under laboratory conditions (Fig. 2.1). The soil, in a pot with a volume of 400 cm³, was composed of minerals and organic matter (humus and plant debris), classified according to size from clay to sand in the aggregate.

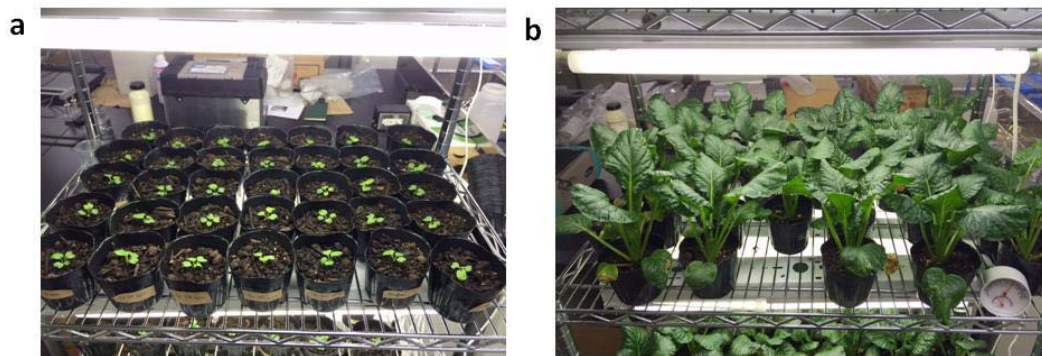


Fig. 2.1. Growth of Japanese mustard spinach (*Brassica rapa* var. *perviridis*) in metal-contaminated soil and normal soil in a experimental room. These photos show (a) initial stage of cultivation; 14 days after sowing and (b) a mature condition of the plants; 70 days after sowing.

Height of a pot was 10 cm.

Four types of metal, Cu, Pb, Zn, and Cd, were selected for simulating contaminated soils for the following reasons. Cu, Pb, Zn are common metals present in mineralized soils around metal deposits. Although soil Cd, a contaminant derived from mineral outcrops, is rare and generally limited when associated with sphalerite (ZnS) in the form of greenockite (CdS), it has been recognized as having strong biological toxicity (Woolhouse, 1983). Cu and Zn are micronutrients, and Pb and Cd may have different physiological functions in plants at a level of tolerance (Alloway, 2013). The four metals originated from standard metal solutions of $\text{Cu}(\text{NO}_3)_2$, $\text{Pb}(\text{NO}_3)_2$, $\text{Zn}(\text{NO}_3)_2$, and $\text{Cd}(\text{NO}_3)_2$. The solutions were mixed with HNO_3 , $\text{Na}(\text{OH})_2$, and K-phosphate buffers to preserve the composition of the non-metallic elements and the pH at a normal level (6–7). The solutions were uniformly mixed with the soils, and the metal contaminants were classified into three levels based on their metal concentration: low (20 ppm), medium (100 ppm), and high (200 ppm). In total, 26 pots were prepared: 2 pots for each of the four metals and the three contaminant levels (24 pots) and, as a control, 2 pots of normal soil without metals added. The seeds were germinated in the control soil for 2 weeks, and then the sprouts were transplanted to the pots with metal-contaminated soils. The plants had been exposed to light and dark for 16 and 8 hours a day, respectively, at approximately 20 °C in the daytime and 15 °C in the nighttime, and supplied with distilled water daily to preserve the moisture level.

The measurements of reflectance spectra and total chlorophyll content began when the plants bore four or more leaves at 60 days after the sowing and continued over the next 20 days, at 5-day intervals. Four 100 W quartz–tungsten–halogen lights were used as a source of illumination for the spectral measurements at a 45° incident angle under darkroom conditions to prevent the entry of light from outside. A fiber optic sensor was placed less than 5 cm from the leaves.

The reflectance spectra of a specimen was the average of the measurements of two to four leaves, repeated 10 times for each leaf, and the total chlorophyll content of a specimen was averaged from the leaves measured along the adaxial direction and by inserting a leaf into the device aperture (Fig. 2.2). To convert the reflectance spectra to the VNIR and SWIR band reflectances of Landsat TM and ETM+ sensors, the original reflectances were averaged over a wavelength range of each band using ENVI software.

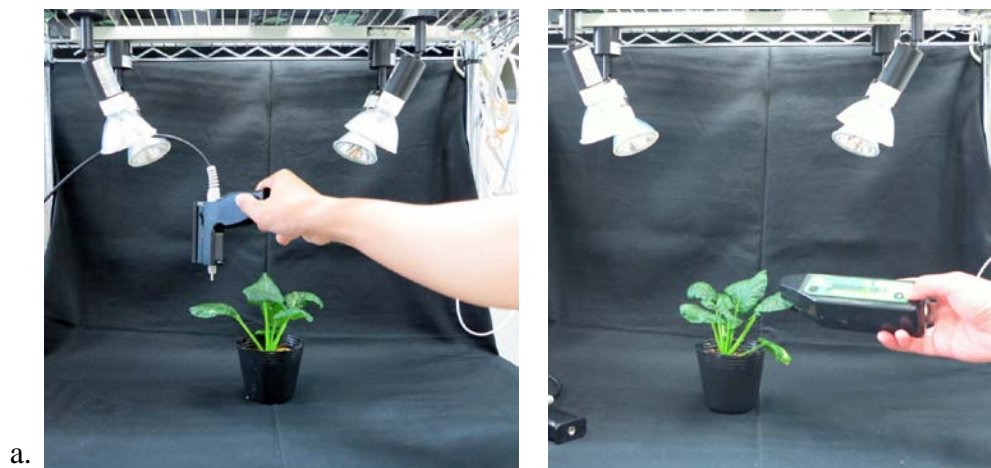


Fig. 2.2. Measurements of (a) reflectance spectra using ASD Fieldspec3 and (b) total chlorophyll using an AtLeaf chlorophyll meter under laboratory conditions.

Additional analyses were performed using microphotographs and semi quantitative elemental mapping with scanning electron analysis–energy dispersive spectrometry (SEM-EDS) to show the structural pattern of vegetation stress and the distribution of elements in the surface. Samples were prepared for the SEM analysis by simple air-drying without pre-treatment. Samples from fresh leaves were mounted on SEM stubs and stored in a desiccator with a silica gel until dry for 24 h. This simple preparation enabled successful examination of the wax microstructure at high resolution, and some shrinkage of the epidermal cells occurred (Pathan et

al., 2008). SEM preparation and analysis were performed on the last day of the spectra and total chlorophyll measurement. The experiments took place at the Laboratory of Geochemistry Environment, Kyoto University, in October-December 2013.

2.2.2. Definition of the new vegetation index

VI is considered an important approaches to analyzing vegetation stress using remote sensing (Slonecker, 2011), which is a mathematical manipulation of a digital number (DN) used to quantify and detect vegetation conditions. There are numerous types of VIs, but only some are useful for evaluating vegetation stress caused by heavy metals. For areas covered almost entirely by plants, with only a small fraction of exposed soil, a normalized difference vegetation index (NDVI; Rouse et al. (1973)) is the most reliable VI for evaluating vegetation stress due to metal absorption (Boluda et al., 1993; Dunagan et al., 2007). NDVI is formulated as follows:

$$\text{NDVI} = \frac{N - R}{N + R} \quad (2.1)$$

where N and R are the reflectances at NIR and visible red wavelengths, respectively. NDVI is useful for multispectral imagery, covering wide areas with a small number of bands such as the Landsat series and Advanced Spaceborne Thermal Emission and Reflection Radiometer (ASTER) imageries. The wavelength of each band is broad. As a recent advance, VIs derived from a more limited wavelength range of hyperspectral imagery than NDVI have successfully detected vegetation stress from metals. These VIs include the red edge position (REP), the photochemical reflectance index (PRI), and the normalized pigment chlorophyll index (NPCl) (Curran et al., 1990; Gamon et al., 1992; Peñuelas, Gamon et al., 1994). However, hyperspectral imageries do not cover the entire Earth's land surface. Landsat and ASTER imagery are more versatile, because they provide global coverage of the land's surface.

Common to NDVI and other VIs, including the above and listed in Slonecker (2011), is the main use of VNIR reflectances only. However, SWIR reflectances are sensitive to leaf water content and thus can be used to detect vegetation stress by water supply interference. Therefore, a VI derived from reflectance data in the VNIR and SWIR regions is expected to enhance detection accuracy of vegetation anomalies. Based on this expectation, a new VI, the Vegetation Index considering Greenness and Shortwave infrared (VIGS), is proposed. This index is aimed at wide availability to general multispectral satellite imagery by integrating visible green, red, NIR, and SWIR reflectances as:

$$\text{VIGS} = w_1 \left(\frac{G - R}{G + R} \right) + w_2 \left(\frac{N - R}{N + R} \right) + w_3 \left(\frac{N - S1}{N + S1} \right) + w_4 \left(\frac{N - S2}{N + S2} \right) \quad (2.2)$$

where G , $S1$, and $S2$ denote reflectances in the visible green and two SWIR regions, respectively, and w_1 , w_2 , w_3 , and w_4 are weights for emphasizing each term. For Landsat ETM+ imagery, $S1$ and $S2$ correspond to bands 5 and 7 (B5 and B7). The visible blue region (Landsat band 1) is excluded here, because even though the blue band is capable of differentiating vegetation from soil or rock surfaces, it has been known as the “noisiest” region caused by atmospheric scatter. Considering reports on the variability of reflectances induced by vegetation stress in the selected regions (Carter, 1991; Horler et al., 1980; Sridhar et al., 2007) and using the data sets in the latter two references, a weights set, $w_1=1.0$, $w_2=0.5$, $w_3=1.5$ and $w_4=1.5$, was obtained as the most suitable because the VIGS from this combination greatly enhanced the difference in stress. More explanation about selection of the VIGS band combination and weights values as follows.

As mentioned above, the reflectance characteristics and control factors are the bases of selecting the bands and formulating VIGS. Moreover, VIGS is basically composed of the following three previous VIs. The first is a visible green to red normalized difference index as Motechka et al. (2010), represents the best range to detect chlorosis, one of the representative

phenomena of metal-induced vegetation stress. Motohka et al. (2010) demonstrated that the green-red vegetation index was useful to quantify seasonal changes in vegetation activity, in particular the degree of senescence. The second is the most widely-used VI, NDVI as has been discussed before. Because SWIR reflectances have been known to be affected by leaf water content, which is partly controlled by the metal-induced stress, as demonstrated by the present study and several previous studies summarized in Ji et al. (2011), shortwave infrared-based normalized difference spectral index was incorporated into VIGS as the third VI.

For the determination of weight values were determined by trial and error based on a preliminary examination using experimental data sets from two references (Horler et al. 1980; Sridhar et al. 2007). In the two references for the data source (Horler et al. 1980; Sridhar et al. 2007), pea plants and barley plants (*Hordeum vulgare*) were selected for the metal-induced vegetation stress. Pea plants were grown in culture solutions with different copper (Cu), lead (Pb), and zinc (Zn) concentrations (Horler et al., 1980). The metal treatments of Cu 200 ppm, Pb 500 ppm, Pb 1000 ppm, Pb 2000 ppm, Zn 200 ppm, and Zn 400 ppm were expressed as Cu, Pb-1, Pb-2, Pb-3, Zn-1, and Zn-2, respectively (Fig. 2.3a). In the case of barley plants by Sridhar et al. (2007), 2 mM, 50 mM, and 150 mM of Zn solutions and 1 mM and 10 mM of cadmium (Cd) solutions (Zn-1, Zn-2, Zn-3, Cd-1, and Cd-2 in short: Fig. 2b) were added to the soils. To make a reference data, one control sample without metal addition was prepared for each metal experiment. The NDVI and VIGS results for the data sets are shown in Fig. 2.3 in which the VI values of NDVI decrease with increasing the metal-induced vegetation stress, while the VIGS values increase with the stress. The above set of weights was used for VIGS. For the comparison, the NDVI and VIGS values were normalized between 0 and 1 using the maximum value. Both the VIs express the vegetation stresses that increase with increasing the metal concentration. The

other sets of weights were inferior to the above set of weights to express the stresses. Based on those preliminary examinations, the above set of weights was selected.

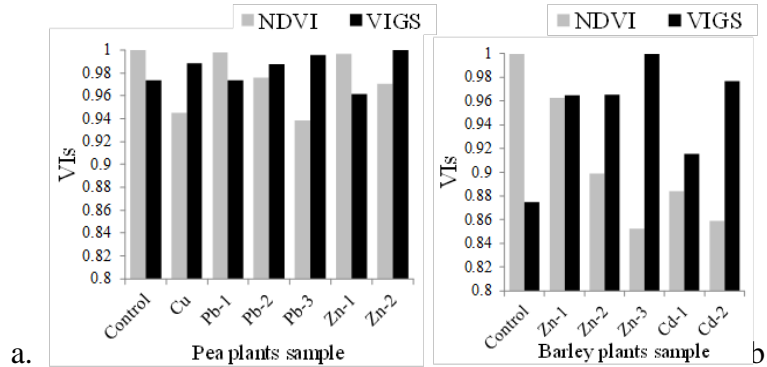


Fig. 2.3. Comparison of NDVI and VIGS values using reflectance data from (a) Horler et al. (1980) and (b) Sridhar et al. (2007). The value ranges were normalized between 0 and 1.

2.3. Results

2.3.1. Physiological and reflectance analysis

The effect of soil metal contamination on plant growth was obvious—with all four metals, the higher metal content resulted in shorter plants (Fig. 2.4). This symptom of vegetation stress from metal contamination is the same as the results of previous studies (Horler et al., 1980; Slonecker, 2011). Another common symptom of high exposure to metal was chlorosis of leaves, the cause of which is insufficient chlorophyll in leaves associated with a low photosynthetic rate. Chlorosis causes insufficient production of chlorophyll, followed by a decrease in the photosynthetic rate. Chlorotic leaves were a paler green than the leaves of plants exposed to a lower level of metal and the plants in control soil. The most typical chlorosis appeared in the specimen with a high Cd content.

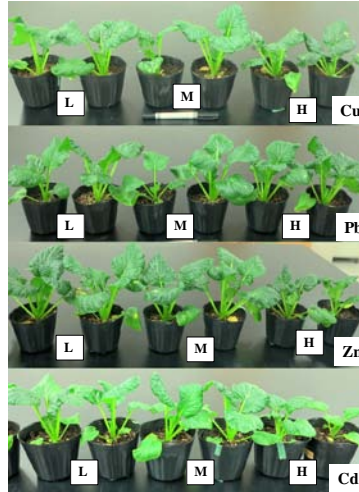


Fig. 2.4. Difference in growth of Japanese mustard spinach with metal content level in soils (L = low, M = medium, and H = high). Selected metals were Cu, Pb, Zn, and Cd. This photo shows a mature condition of the plants, 70 days since sowing.

Although chlorosis was not visible in the specimens in soil with a low metal content, it was associated with the total chlorophyll content of leaves, which generally decreased with increasing metal content, except for Pb (Fig. 2.5). The chlorophyll content in leaves can reveal patterns that indicate high, medium, and low levels of metal in soils as well as chlorophyll content. The effect of metal content on total chlorophyll content was strongest in the Cd specimens: the chlorophyll content of the specimen with high Cd content was half of that of the reference specimen. The Cu and Zn specimens showed similar trends and total chlorophyll content. This condition means that the soil content of Cu, Zn, and Cd was sufficient to interfere with the photosynthetic activity of Japanese mustard spinach. By contrast, this effect was weak in the Pb specimens, in which there was no significant difference in the total chlorophyll content regardless in the level of Pb content.

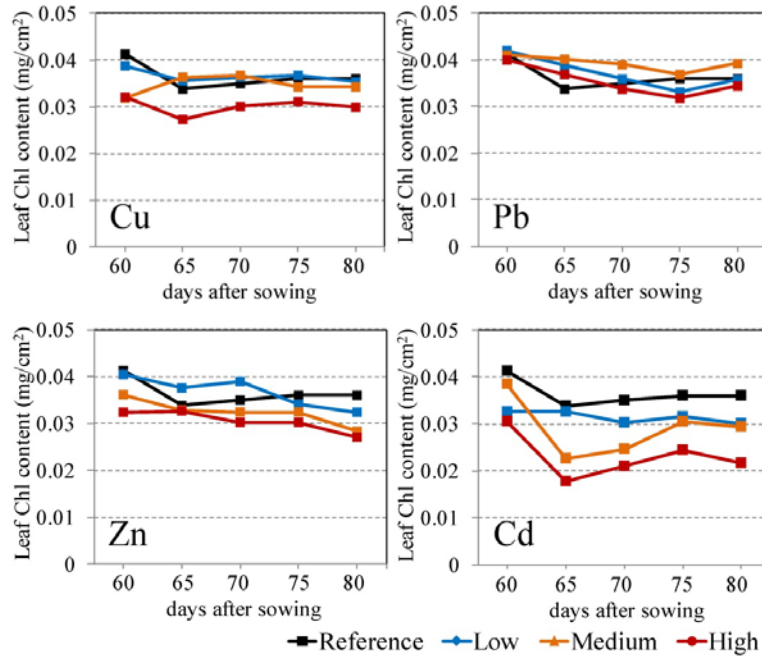


Fig. 2.5. Changes in total chlorophyll content of leaves with metal content and days since sowing. Each chlorophyll (Chl) content is an average of two specimens at each metal content level in soils and two reference specimens.

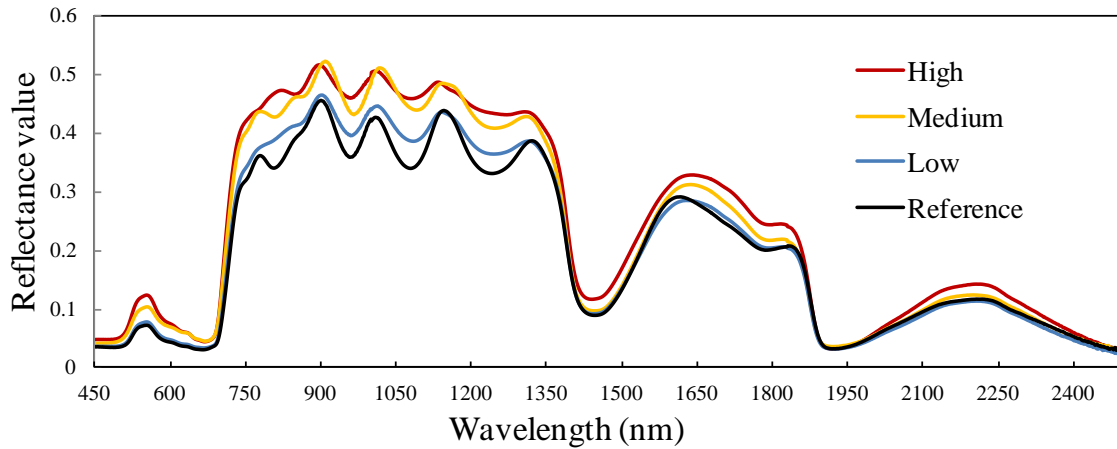


Fig. 2.6. Typical reflectance spectra of Japanese mustard spinach in normal soils (reference) and different levels of Cd-contaminated soils. These spectra were collected on 65 days after sowing.

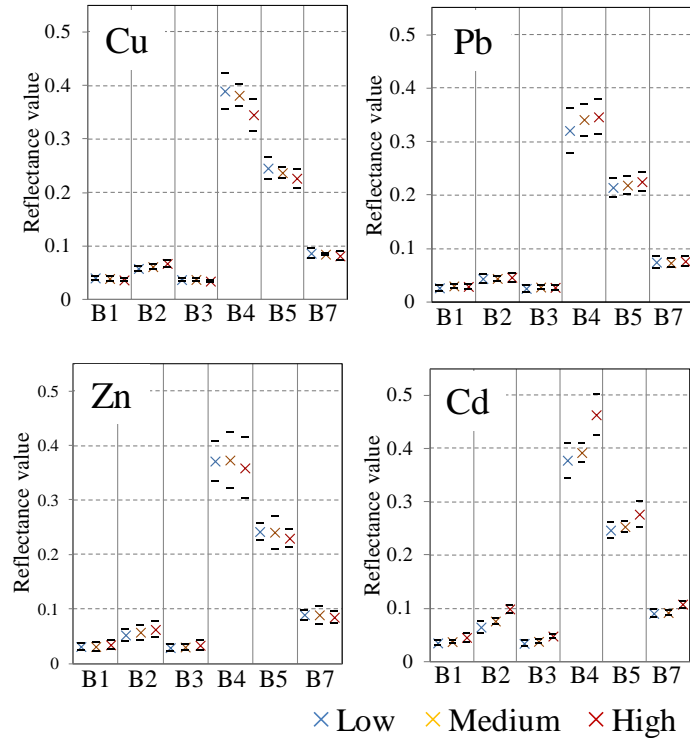


Fig. 2.7. Average reflectances (X symbols) measured between 60 and 80 elapsed days for each metal and content level, converted to reflectances in Landsat bands (visible B1–B3, NIR B4, and SWIR B5 and B7). Bars above and below averages indicate standard deviations.

The results also elucidated the featured changes in the reflectance spectra based on the metal type and content in soils, e.g., Fig. 2.6. is typical reflectance spectra characteristics of reference and Cd-contaminated soils. Moreover, the results for all metals (Cu, Pb, Zn, and Cd) also in comparison with Landsat bands can be explain as follows. The reflectances in the visible wavelength (450–750 nm and Landsat B1–B3) were dominated by the pigments composed of chlorophylls, carotenoids, and anthocyanins (Sims & Gamon, 2002). The blue (B1) and red (B3) regions are absorbed by chlorophyll. In consonance with the magnitude of decrease in the total chlorophyll content, the reflectances of Cu and Zn specimens only slightly increased with increasing metal, the increase was largest in the Cd specimens (Fig. 2.7). Common to these

metals, the reflectances increased most remarkably in the visible green (B2) caused by chlorophyll degradation.

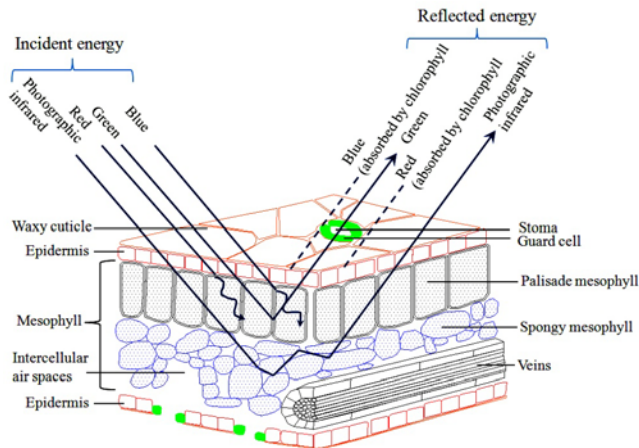


Fig. 2.8. Schematic of a leaf cross section, showing the interaction between the optical incident energy and leaf structure after Buschmann & Nagel (1993).

In the NIR (B4) and SWIR (B5 and B7), the reflectance change patterns with the metal content are classified into two groups, I: Cu and Zn and II: Pb and Cd (Fig. 2.7). Group I shows the decrease in reflectances in the three bands with increasing metal content, whereas the reflectances in Group II increase. The cellular structure of leaves and the water content in the tissues dominate the reflectances in the NIR and SWIR, respectively (Grant, 1987). Deformation and collapse of mesophyll cells must have occurred in Group I, which reduced the spongy mesophyll air volume and consequently decreased the scattering of electromagnetic (EM) waves (Knipling, 1970; Rosso et al., 2005). This is the most likely explanation for the decrease in the reflectance in the NIR. Cd strongly and Pb slightly loaded the leaf moisture stress, causing the dehydration of the plants (even though this is not experimentally validated). This phenomenon induced an increase in the reflective surface area of cells and consequently the NIR reflectance

by enhancement of the scattering intensity of EM waves from the cells (Ripple, 1986). In addition, a decrease in the water content caused an increase in the SWIR reflectance by reducing the water absorption of EM waves. Fig. 2.8 shows the interaction between optical energy and schematic leaf section.

2.3.2. Comparison between NDVI and VIGS

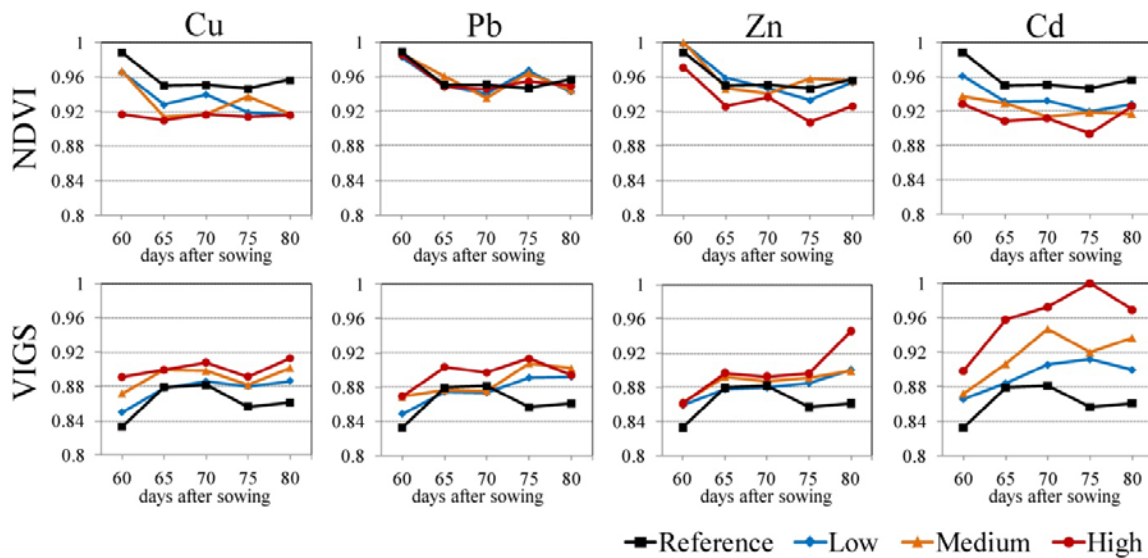


Fig. 2.9. Comparison of NDVI and VIGS change with metal contents and days since sowing. As with total chlorophyll content of leaves (Fig. 2.5), each VI value is an average of two specimens at each metal content in soils and two reference specimens without metal addition.

Using the Landsat band reflectances, the NDVI and VIGS are calculated and their changes in metal content and elapsed day are compared in Fig. 2.9. The value ranges were normalized between 0 and 1 by using the maximum value result from the calculation and a minimum value of 0 to clarify and compare between VIs. The two VIs show opposite trends: the

NDVI decreases with increasing metal content and the VIGS change is the reverse. The NDVI's changes are concordant with the total chlorophyll content, which is confirmed in the absence of the NDVI value changes in Pb, despite the difference in metal content. By contrast, a change in VI values appeared in the VIGS in the Pb specimens, and more remarkable changes were revealed by the VIGS in the Cd and Zn specimens. Another noteworthy point is that the magnitude of VIGS values accurately followed the order of metal content for most elapsed days; i.e., the VIGS values increased in order of low, medium, and high content. This consistency verifies the effectiveness of using SWIR for the VI.

2.4. Discussion

2.4.1. Changes in the plants physiology

As found in this study, metal absorption causes a phenomenon termed vegetation stress, which can be caused by any metal type and results in the physiological decline in growth rate, photosynthetic activity, and chlorophyll content. The declines are also caused by many other factors, such as salinity, drought, disease, nutrient deficiency, and senescence (Chapin, 1991; Woolhouse, 1983). However, the effect of metal absorption by plants is metal-dependent and different metal contaminants may induce different plant responses to the same level (see Tables 2.2 and 2.3).

To investigate the morphology and elemental distribution of the metal-enrichment in leaf surfaces, I carried out scanning electron microscope measurements with energy-dispersive X-ray spectroscopy (SEM-EDX). The SEM analysis revealed a direct effect of metal on a plant's structure in stomatal form. Detailed observation showed that a high content of Cd stimulated stomata closure (Fig. 2.10a), which may have induced hydropassivity from turgor pressure

changes or hydroactive mechanisms for abscisic acid (ABA) signaling (Poschenrieder & Barceló, 1999) compared with the control plants (Fig. 2.10b). This condition is caused by the effects of metal absorption on photosynthetic activity due to decreased CO₂ availability, which causes transpiration decrease and impairs water-use efficiency in plants (Osakabe et al., 2014).

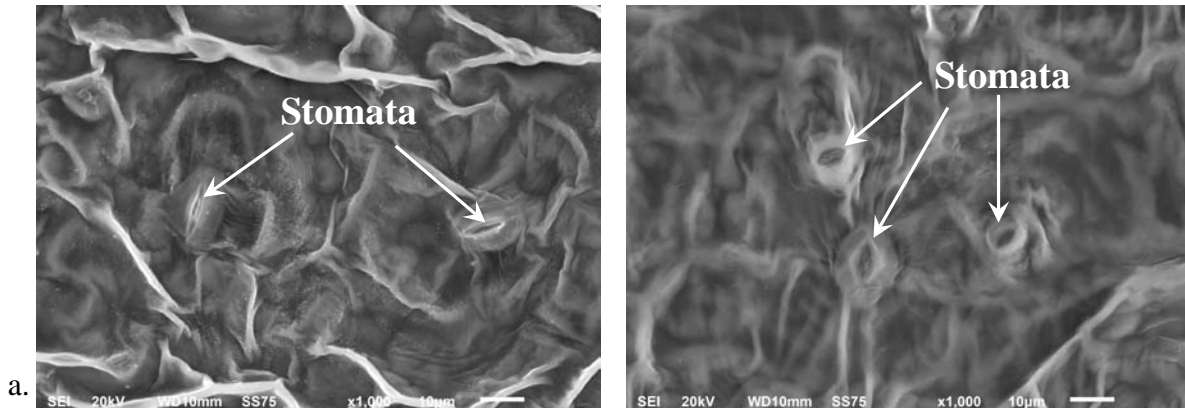


Fig. 2.10. SEM photomicrographs showing the effect of metal absorption on stomatal closure in: (a) leaf with high Cd content in soil; (b) reference leaf without addition of metal, with open stomata. These leaf samples were prepared by a simple air-drying method.

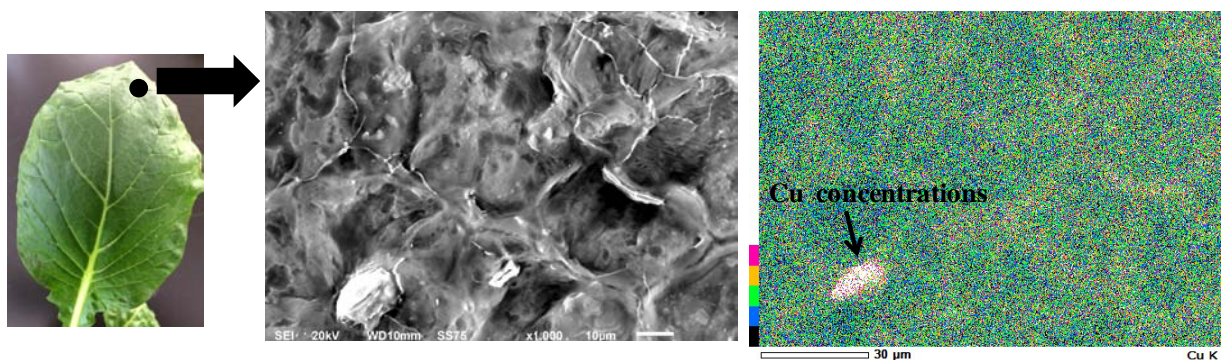


Fig. 2.11. Schematic point location on the leaf surface of an SEM-EDX analysis and semi-quantitative Cu element distribution. The SEM-EDX analyses were performed on the adaxial faces.

Interesting results were found during the SEM-EDX analysis from a metal-enriched area concentrated on the surface of leaves within deformed stomata tissues and preferential localization at the edges of the leaves (Fig. 2.11). This evidence indicated that metal-contaminated plants may show disruptions in transpiration gas exchange activity.

2.4.2. Changes in the spectroscopic features

For the spectral analysis, the response of a metal anomaly can appear by a spectral pattern in the visible to SWIR region. The spectroscopic features exhibited systematic differences due to added metal and changed gradually over time. As presented in section 2.4.1, chlorophyll content, as an indicator of stress, is strongly related to the visible region. A common feature that is usually used as a signature of a stress condition related to decreasing leaf chlorophyll content is red edge position (REP) (Curran et al., 1990). Red edge is a feature of rapid change in vegetation reflectance at approximately 690–740 nm of narrow electromagnetic spectrum (Fig. 2.12a). REP can be defined as the maximum derivative of vegetation reflectance in the red edge region (Fig. 2.12b). As a result, the REP tended toward shorter wavelengths as total chlorophyll content decreased in line with the increasing metal content. Consequently, the REP confirmed the effectiveness of the spectra in the visible region to reveal the chlorophyll stress that can be caused by the toxicity of metal in plants.

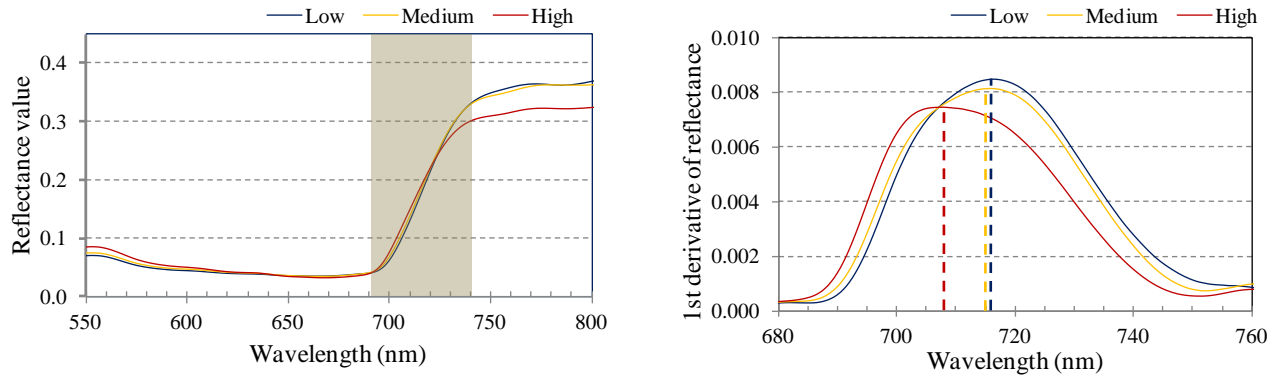


Fig. 2.12. Typical feature of a spectral response curve in the VNIR region indicates the red edge region found in this study. (a) Reflectance spectra of Cu contamination show the red edge region (gray shading). (b) The first derivative of reflectance from (a) shows the peak values as an indicator of the REP. The REP for higher Cu content tends toward shorter wavelengths.

However, the expansion effects of metal stress in plants not only relate to chloroplast but also affect the structure in leaves and water stress, which can be revealed at longer wavelengths. A noteworthy feature found by the experiment is that there were two change patterns in the NIR reflectance spectra (the reflectance decrease in Group (i) and increase in Group (ii), see Section 4.1), associated with the metal contents. These patterns are similar to the initial stage, Group (ii), and the advanced stage, Group (i), of plant senescence (Grant, 1987). This condition suggest that, in some way, the correlating of reflectance spectra as the response of metal content probably confusing, may be caused by of the complexity of plants (Horler et al., 1980). Another consideration is other factors concurred with metal absorption that should be anticipated. There is a possibility for conflicting result given by previous researchers, as summarized by Horler et al. (1980), that the degree of whether increasing or decreasing of vegetation reflectance is affected by metal content are dependent on metal type and plant species. It is even more strongly

appearing in the NIR to SWIR that have higher reflectance rather than visible wavelengths as shown at present results.

In this study, the NDVI graph for Pb-treated samples indicates that there is no significant difference between lower and higher levels of metal contamination. This can be explained by the total chlorophyll content, which showed the same tendency, and suggests that Pb contamination is not severe enough to affect the spectral response of Japanese mustard spinach. The VIGS values are more sensitive to vegetation stress than NDVI and can enhance the stress difference depending on the metal contents in soils.

Based on these results, it is concluded that the use of VNIR only is inadequate to accurately detect vegetation stress by metal absorption, because it does not address water stress whose effect appeared in the SWIR region. VIGS considers both chloroplast-related, water stresses, and the varied responses of plants due to metal stress. Another point is that the NDVI tended to decrease while VIGS increased with selected metals (Cu, Pb, Zn, and Cd) in the specific conditions. The essential function of the VI is to enhance the difference in vegetation activity, which is associated with plant type, amount, and condition, and minimize the effects of solar irradiance and soil background (Jackson & Huete, 1991). Because non-vegetation pixels typically have small VI values, values actually related to vegetation anomalies are desired to be large so they can easily be distinguished from non-vegetation values. The VIGS can satisfy this requirement.

2.5. Conclusions

This chapter discusses the applicability of geobotanical remote sensing through spectral analysis and describes a new vegetation index, the VIGS, to detect vegetation stress caused by metal contamination in soils. The conclusions can be summarized as follows:

- Vegetation stress due to contamination of soil by metal (Cu, Pb, Zn, and Cd) in Japanese mustard spinach showed clear effects on the rate of plant growth under conditions of higher metal content. The contamination also caused chlorosis of leaves that caused a decline in the photosynthetic rate and induced chlorophyll deficiency in the leaves.
- There were changes in reflectance spectra with different types and levels of metal exposure. In consonance with the magnitude of decrease in total chlorophyll content, the reflectances in the visible region increased with increasing metal content. In NIR and SWIR, there were two patterns of reflectance change in which these phenomena were related to either deformation of cells or an increase in the reflective surface area of cells.
- A new VI combining reflectances in VNIR and SWIR, the VIGS, is proposed that will enhance the detection of vegetation stress due to metal absorption. To evaluate sensitivity, the VIGS was compared with the NDVI. The VIGS was proven to be more sensitive for detecting vegetation stress because it considers both the chloroplast-related stress and the water stress.

References

Alloway, B. (2013). Heavy metals and metalloids as micronutrients for plants and animals. In B. J. Alloway (Ed.), *Heavy Metals in Soils SE - 7* (Vol. 22, pp. 195–209). Springer Netherlands. http://doi.org/10.1007/978-94-007-4470-7_7

- Barceló, J., & Poschenrieder, C. (1990). Plant water relations as affected by heavy metal stress: A review. *Journal of Plant Nutrition*, 13(1), 1–37. <http://doi.org/10.1080/01904169009364057>
- Boluda, R., Andreu, V., Gilabert, M. A., & Sobrino, P. (1993). Relation between reflectance of rice crop and indices of pollution by heavy-metals in soils of Albufera natural park (Valencia, Spain). *Soil Technology*, 6, 351–363.
- Buschmann, C., & Nagel, E. (1993). In vivo spectroscopy and internal optics of leaves as basis for remote sensing of vegetation. *International Journal of Remote Sensing*, 14(4), 711–722. <http://doi.org/10.1080/01431169308904370>
- Carter, G. A. (1991). Primary and secondary effects of water content on the spectral reflectance of leaves. *American Journal of Botany*, 78(7), 916–924. <http://doi.org/10.2307/2445170>
- Chapin, F. (1991). Integrated responses of plants to stress. *BioScience*, 41(1), 29–36. <http://doi.org/10.2307/1311538>
- Curran, P. J., Dungan, J. L., & Gholz, H. L. (1990). Exploring the relationship between reflectance red edge and chlorophyll content in slash pine. *Tree Physiology*, 7(1_2_3_4), 33–48.
- Dunagan, S. C., Gilmore, M. S., & Varekamp, J. C. (2007). Effects of mercury on visible/near-infrared reflectance spectra of mustard spinach plants (*Brassica rapa* P.). *Environmental Pollution (Barking, Essex)*, 148(1), 301–311. <http://doi.org/10.1016/j.envpol.2006.10.023>
- Gamon, J. A., Peñuelas, J., & Field, C. B. (1992). A narrow-waveband spectral index that tracks diurnal changes in photosynthetic efficiency. *Remote Sensing of Environment*, 41(1), 35–44. [http://doi.org/10.1016/0034-4257\(92\)90059-S](http://doi.org/10.1016/0034-4257(92)90059-S)
- Grant, L. (1987). Diffuse and specular characteristics of leaf reflectance. *Remote Sensing of Environment*, 22(2), 309–322. [http://doi.org/10.1016/0034-4257\(87\)90064-2](http://doi.org/10.1016/0034-4257(87)90064-2)
- Horler, D. N., Barber, J., & Barringer, A. R. (1980). Effects of heavy metals on the absorbance and reflectance spectra of plants. *International Journal of Remote Sensing*, 1(2), 121–136. <http://doi.org/10.1080/01431168008547550>
- Jackson, R. D., & Huete, A. R. (1991). Interpreting vegetation indices. *Preventive Veterinary Medicine*, 11(3-4), 185–200. [http://doi.org/10.1016/S0167-5877\(05\)80004-2](http://doi.org/10.1016/S0167-5877(05)80004-2)

- Ji, L., Zhang, L., Wylie, B. K., & Rover, J. (2011). On the terminology of the spectral vegetation index $(\text{NIR} - \text{SWIR}) / (\text{NIR} + \text{SWIR})$. *International Journal of Remote Sensing*, 32(21), 6901–6909. <http://doi.org/10.1080/01431161.2010.510811>
- Knipling, E. B. (1970). Physical and physiological basis for the reflectance of visible and near-infrared radiation from vegetation. *Remote Sensing of Environment*, 1(3), 155–159. [http://doi.org/10.1016/S0034-4257\(70\)80021-9](http://doi.org/10.1016/S0034-4257(70)80021-9)
- Kooistra, L., Salas, E. A. ., Clevers, J. G. P. ., Wehrens, R., Leuven, R. S. E. ., Nienhuis, P. ., & Buydens, L. M. . (2004). Exploring field vegetation reflectance as an indicator of soil contamination in river floodplains. *Environmental Pollution*, 127(2), 281–290. [http://doi.org/10.1016/S0269-7491\(03\)00266-5](http://doi.org/10.1016/S0269-7491(03)00266-5)
- Motohka, T., Nasahara, K. N., Oguma, H., & Tsuchida, S. (2010). Applicability of Green-Red Vegetation Index for remote sensing of vegetation phenology. *Remote Sensing*, 2(10), 2369–2387. <http://doi.org/10.3390/rs2102369>
- Osakabe, Y., Osakabe, K., Shinozaki, K., & Tran, L.-S. P. (2014). Response of plants to water stress. *Frontiers in Plant Science*, 5(86). <http://doi.org/10.3389/fpls.2014.00086>
- Pathan, A. K., Bond, J., & Gaskin, R. E. (2008). Sample preparation for scanning electron microscopy of plant surfaces-Horses for courses. *Micron*, 39(8), 1049–1061.
- Peñuelas, J., Gamon, J. A., Fredeen, A. L., Merino, J., & Field, C. B. (1994). Reflectance indices associated with physiological changes in nitrogen- and water-limited sunflower leaves. *Remote Sensing of Environment*, 48(2), 135–146. [http://doi.org/10.1016/0034-4257\(94\)90136-8](http://doi.org/10.1016/0034-4257(94)90136-8)
- Poschenrieder, C., & Barceló, J. (1999). Water relations in heavy metal stressed plants. In *Heavy Metal Stress in Plants SE - 10* (pp. 207–229). Springer Berlin Heidelberg. http://doi.org/10.1007/978-3-662-07745-0_10
- Rencz, A. N., & Watson, G. P. (1989). Biogeochemistry and LANDSAT TM data: Application to gold exploration in northern New Brunswick. *Journal of Geochemical Exploration*, 34(3), 271–284. [http://doi.org/10.1016/0375-6742\(89\)90117-9](http://doi.org/10.1016/0375-6742(89)90117-9)
- Ripple, W. J. (1986). Spectral reflectance relationships to leaf water stress. *Photogrammetric Engineering and Remote Sensing*, 52(10), 1669–1675.
- Rosso, P. H., Pushnik, J. C., Lay, M., & Ustin, S. L. (2005). Reflectance properties and physiological responses of *Salicornia virginica* to heavy metal and petroleum

- contamination. *Environmental Pollution*, 137(2), 241–252. <http://doi.org/10.1016/j.envpol.2005.02.025>
- Rouse, J. W., Haas, R. H., Schell, J. A., & Deering, D. W. (1973). Monitoring vegetation systems in the Great Plains with ERTS. In *Proceedings of the Third ERTS-1 Symposium* (pp. 309–317). NASA SP-351 I.
- Salisbury, F. B., & Ross, C. W. (1992). Plant physiology. In *Plant physiology*. Wadsworth Publishing Company.
- Sims, D. A., & Gamon, J. A. (2002). Relationships between leaf pigment content and spectral reflectance across a wide range of species, leaf structures and developmental stages. *Remote Sensing of Environment*, 81(2-3), 337–354. [http://doi.org/10.1016/S0034-4257\(02\)00010-X](http://doi.org/10.1016/S0034-4257(02)00010-X)
- Slonecker, E. T. (2011). Analysis of the effects of heavy metals on vegetation hyperspectral reflectance properties. In P. S. Thenkabail, J. G. Lyon, & A. Huete (Eds.), *Hyperspectral remote sensing of vegetation* (pp. 561–578). CRC Press. <http://doi.org/doi:10.1201/b11222-33>
- Sridhar, B. B. M., Han, F. X., Diehl, S. V, Monts, D. L., & Su, Y. (2007). Spectral reflectance and leaf internal structure changes of barley plants due to phytoextraction of zinc and cadmium. *International Journal of Remote Sensing*, 28(5), 1041–1054. <http://doi.org/10.1080/01431160500075832>
- Woolhouse, H. W. (1983). Toxicity and tolerance in the responses of plants to metals. In O. L. Lange, P. S. Nobel, C. B. Osmond, & H. Ziegler (Eds.), *Encyclopedia of plant physiology-physiological plant ecology III* (pp. 245–300). Springer Berlin Heidelberg. Retrieved from <http://link.springer.com/10.1007/978-3-642-68153-0>

Chapter 3

Correlating vegetation reflectance spectra by satellite imagery with geochemical data

3.1. Introduction

Previous geobotany articles have discussed the possibility of using satellite imagery to identify the spectral characteristics of vegetation in areas with geochemical anomalies related to mineral deposits (Boluda et al., 1993; Carranza & Hale, 2001; Karr & Mouat, 1990). The results of the laboratory experiments, which are discussed in Chapter 2, show that the metal absorption of plants induced anomalies that are often associated with chlorosis, which can be seen in the visible regions. Metal absorption was also found to affect the internal structure and water absorption of plants, contributing to the spectral pattern in the near infrared (NIR) and shortwave infrared (SWIR) regions.

In this chapter, an analysis is conducted in order to more clearly understand geobotanical remote sensing by correlating the reflectance value derived from satellite imagery in the visible and SWIR regions with geochemical data obtained under natural conditions. This relationship is also examined by a partial least-squares regression (PLSR) analysis. The PLSR method has commonly been used to analyze a relationship between the metal content and the reflectance spectra (Kooistra et al., 2004; Kooistra et al., 2001; Pandit et al., 2010).

3.2. Study area and geological datasets

The study area is located in Jambi, central Sumatra, Indonesia and is 50 km × 50 km, ranging from 101.73° to 102.18° E and 1.64° to 2.09° S (Fig. 3.1). This area is mountainous with tropical rain forests, and it is mostly covered by dense vegetation.

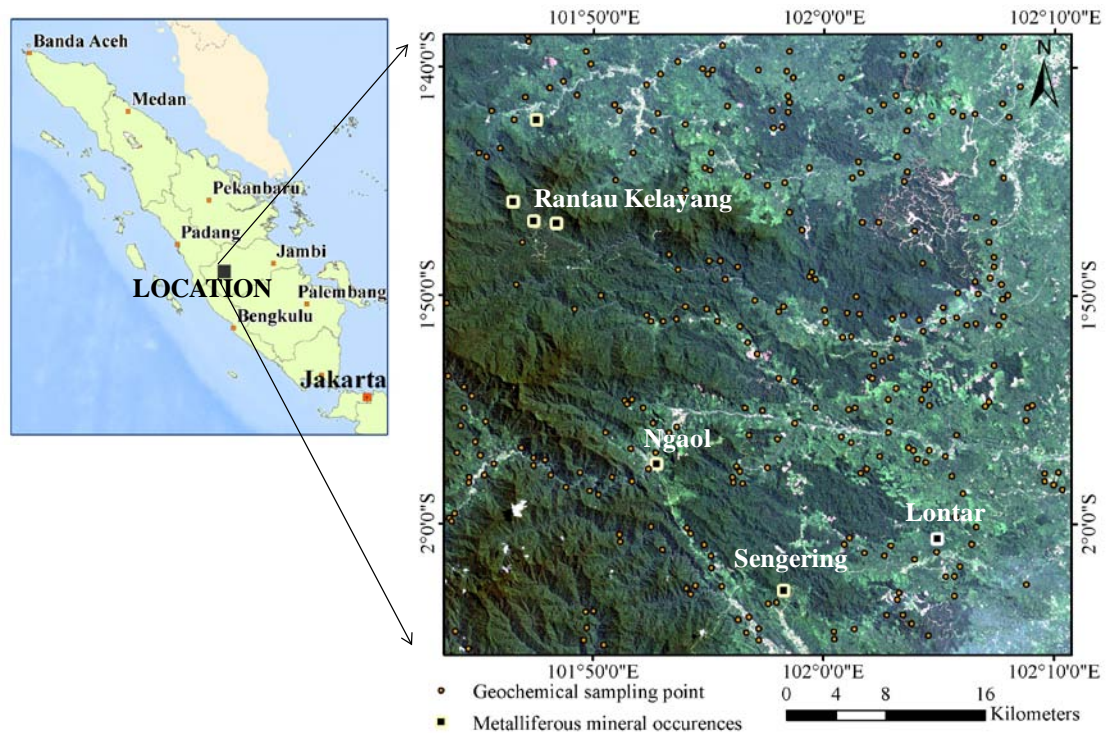


Fig. 3.1. Location of study area in central Sumatra, sampling sites of geochemical data, and mineral occurrences superimposed on sub-scene of true-color composited Landsat ETM+ image acquired on 15 August 2002.

3.2.1. Geologic setting

The main geology and structure of the study area are summarized with a simplified geological map (Fig. 3.2), which is based on the references that were used to prepare regional geological maps (Kusnama et al., 1992; Rosidi et al., 1996; Simandjuntak et al., 1994; Suwarna

et al., 1992). The study area is mainly covered with block-shaped Permian intrusions that trend northwest–southeast. They are part of the Palepat formation and are composed of lava, crystal lithic tuff, and lithic tuff composed of andesite and propylite. The Permian intrusions have undergone low-grade metamorphism and are now deformed. These blocks, the oldest geological formations in the study area, are important in mineral explorations because many regions in which mineralization occurred were found in the formations.

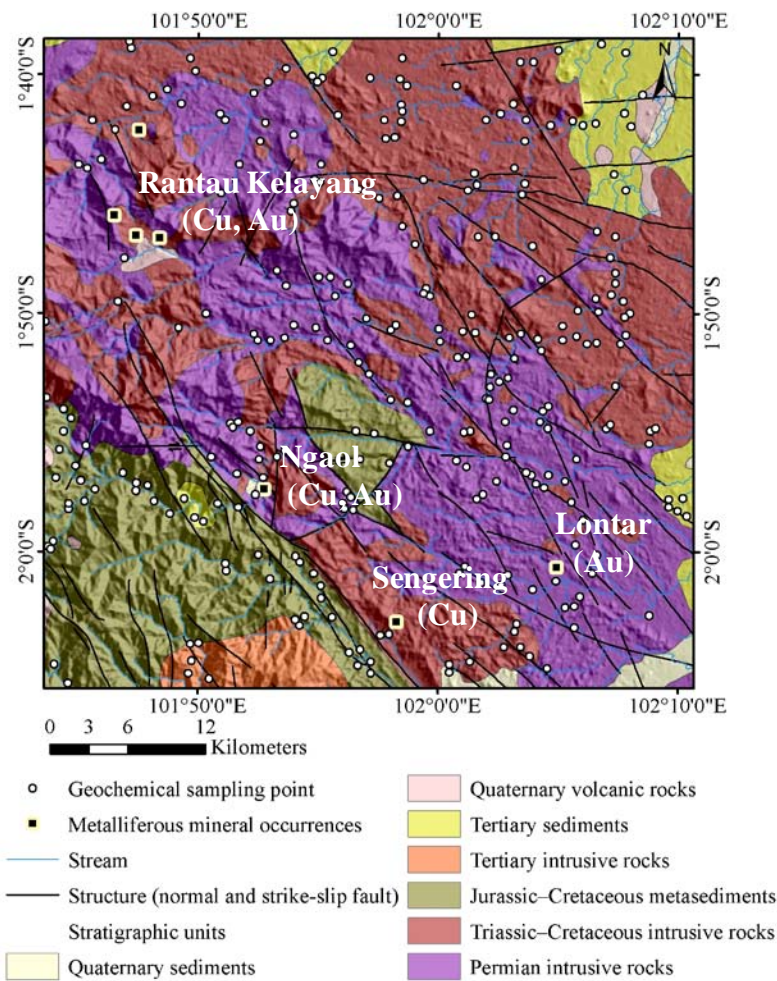


Fig. 3.2. Simplified geological map of the study area (after Kusnama et al., 1992; Rosidi et al., 1996; Simandjuntak et al., 1994; Suwarna et al., 1992).

The subordinate lithology is Triassic–Cretaceous granitoid, with the same trend as the Permian block. In the middle and southwest parts, Jurassic–Cretaceous metasedimentary rocks composed of compact quartzite and weakly deformed pelitic shale and siltstone are distributed along a NW–SE thrust and bounded by Tertiary intrusions. Quaternary volcanic rocks are partially distributed in the west and northeast parts, and Quaternary sediments are only on the plains near the southern and southeast edges of the study area. The distribution of the lithologic units is controlled by faults that mostly strike along NW–SE and (a few) E–W directions. The valleys are deep and their directions are also controlled by the fault strikes. An overall lithological summary including detailed groupings of each lithologic unit can be seen in Table 3.1.

The study area is characterized by joint or separate occurrences of precious and base metals (Crow et al., 1993). Three zones in which significant Cu mineralization occurred were discovered in the Permian intrusions in the Rantau Kelayang, Ngaol, and Sengering regions (see Fig. 3.2). In Rantau Kelayang, low-grade Cu mineralization in the form of disseminated chalcopyrite, a typical feature of porphyry copper deposit, occurred via hydrothermal alterations, propylitization, and silification. The average copper content was found to be less than 0.1% in the fracture zones. In the Ngaol region, the soil survey found some anomalies regarding Cu and Au, near the contact between Jurassic metasedimentary rocks and granitoid intrusions. Small quantities of chalcopyrite were found in the Sengering region. In addition, there are many small Au mining sites along the rivers in the Lontar region because sizeable nuggets of Au are occasionally found in the riverbanks.

Table 3.1. Lithological summary of the study area (after Kusnama et al., 1992; Rosidi et al., 1996; Simandjuntak et al., 1994; Suwarna et al., 1992).

Simplified geological units	Lithocode	Age	Geological Formation	Lithology
Quaternary sediments	1	Holocene to recent	Aluvium	Silt, sand, and gravel
		Holocene to recent	Lake deposits	Silt, sand, clay, mud, and gravel
		Pliocene - Pleistocene	Kasai formation	Acidic pumice tuff, tuffaceous sandstone with bentonit and some lignite intercalations.
Quaternary volcanic rocks	2	Holocene	Undifferentiated volcanics rocks	Volcanic breccia, lahars, tuff breccia, and tuff; basaltic to andesitic composition
		Holocene	Tuff-Volcanic breccia	Tuff, laharc breccia, and andesitic to basaltic
		Pliocene - Pleistocene	Ryho andesite volcanic	Rhyolitic, dacitic andesitic lavas, welded tuff, hybric tuff pucmiceous lithic tuff and volcanic breccia
		Pleistocene	Bukitpunjung formation	Acid to intermediate volcanic breccia, tuff and lava, dark grey to brownish yellow
		Pleistone-Holocene	Undifferentiated acid volcanic rocks	Lava, crystal, and vitric tuff, tuff, tuff-breccia, ignimbrite and obsidian of acid to intermediate composition
Tertiary sediments	3	Miocene-Pliocene	Muaraenim formation	Sandstone, sandy claystone and lignite which reaches up to 10% of the formation thickness
		Miocene-Pliocene	Airbenakat formation	Claystone with sandstone intercalations
		Oligocene-Miocene	Rantaukil formation	Clayey sandstone, tuffaceous sandstone, calcareous sandstone, sandy claystone, tuffaceous claystone, marl, and thin lenses of limestone
		Eocene-Oligocene	Sinamar formation	Conglomerate, coarse-grained quartz sandstone, micaceous quartz sandstone, arkosic sandstone
		Eocene-Oligocene	Gumai formation	Shale, marly limestone, thin layers of andesitic tuff
		Eocene	Bandan formation	Welded tuff, volcanic breccia, and conglomeratic tuff
Tertiary intrusive rocks	4	Paleocene-Eocene	Granodiorite	
		Paleocene-Eocene	Nagan granodiorite	
Jurassic–Cretaceous metasedimentary rocks	5	Cretaceous	Paneta formation	Tuffaceous shale with limestone intercalations
		Cretaceous	Mersrip member of Paneta formation	Limestone with calcareous shale intercalations
		Jurassic	Asai formation/Siguntur formation	Quartzite compact and weakly deformed, pelitic shale, compact limestone, and locally silicified
		Jurassic	Tabir formation	Conglomerate and tuffaceous sandstone, calcareous sandstone with pisolitic andesitic tuff
Triassic–Cretaceous intrusive rocks	6	Cretaceous	Andesite and basalt	
		Cretaceous	Diabase	
		Jurassic	Granite	Biotite granite, granodiorite, and quartz porphyry
		Triassic-Jurassic	Tantan granodiorite	
		Jurassic	Diorite	The composition ranges from hornblende diorite to quartz diorite with spots of mafic minerals
		Jurassic	Syenite	
		Jurassic	Diorite	
Permian intrusive rocks	7	Permian	Palepat formation	Mainly lava, crysal lithic tuff, and lithic tuff of andesitic composition; hydrothermally propylitized, mineralized the rocks with the introduction of pyrites, copper, and molybdenum
		Permian	Ngaol formation	Gneiss, quartzite, meta-limestone, and schist.
		Permian	Meta-limestone member of Ngaol formation	Occurs in lenses, compact, and cavernous, in part marbledized and fractured

Vegetation condition is usually influenced by hydraulic properties of topsoils, particularly permeability, which controls the amount and velocity of water infiltration to deeper soils. Permeability in the study area is strongly correlated with the general geology; it is low in the areas of Permian intrusions and granitoid, moderate in fractured and weathered zones, and

moderate to high in the Quaternary sediments. From the productivity map of aquifers (i.e., near-surface permeability for groundwater flow) modified from a hydrogeological map of Indonesia (Setiawan et al., 2013; Sukiban, 2005; Yudhanagara, 2005; Zahirdin & Hendra, 1982), nearly all the study area has low permeability (non-exploitable groundwater and poorly productive aquifers only for local use), and there are a few locally productive aquifers near faults in the Ngaol region and in the Quaternary sediments (Fig. 3.3).

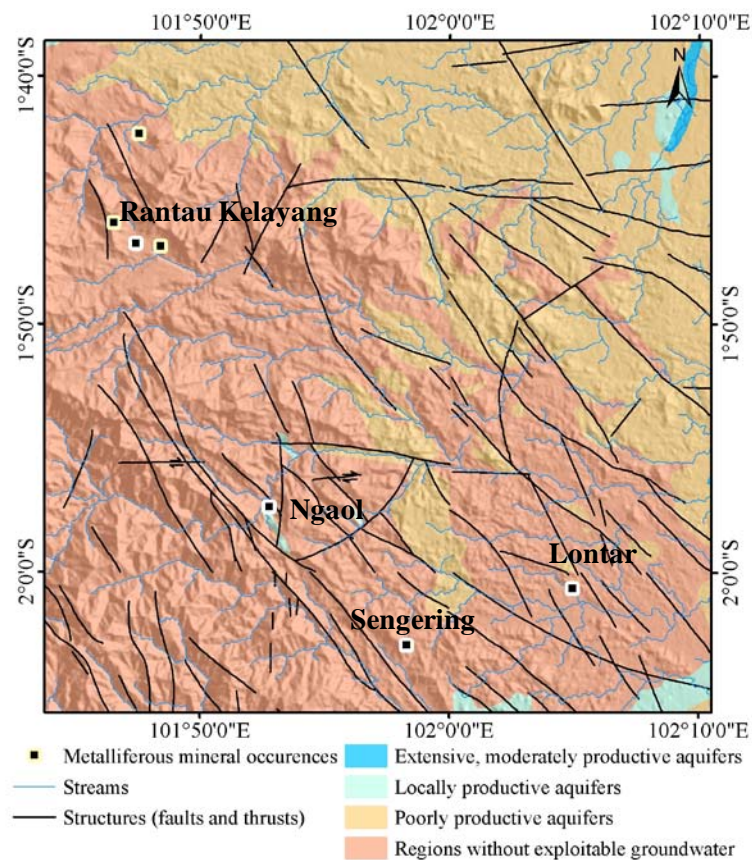


Fig. 3.3. Productivity map of aquifers (near-surface permeability for groundwater flow) superimposed on fault and river distributions, following a hydrogeological map of Indonesia (Setiawan et al., 2013; Sukiban, 2005; Yudhanagara, 2005; Zahirdin & Hendra, 1982).

3.2.2. Geochemical data

Geochemical data of near-surface rocks and soils in the study area are quoted from a report of regional geochemical investigation of southern Sumatra, undertaken systematically at scale 1:250,000 by the Indonesian Directorate of Mineral Resources between 1980 and 1992 (British Geological Survey, 2007). The project was part of Southern Sumatra Geological and Mineral Exploration Project, which was a collaborative project between the DMR and the British Geological Survey.

Table 3.2. Descriptive statistics from 282 data points; metal unit in ppm, except for Fe in %.

Metal element	Minimum	Maximum	Mean	Std. deviation
Cu	1.00	163.00	29.50	25.87
Pb	3.00	145.00	25.16	17.51
Zn	16.00	494.00	97.79	66.67
Co	1.00	72.00	24.70	13.19
Ni	1.00	44.00	15.70	9.30
Mn	30.00	2,810.00	590.23	336.30
Li	3.00	88.00	24.97	13.68
K	640.00	47,000.00	14,158.87	9,257.43
Cr	3.00	160.00	45.14	32.53
Fe	0.10	17.00	4.67	2.52

The geochemical sampling strategy involved the collection of two types of drainage samples: stream sediment and panned concentrates. The sampling of drainage sediment was based on regional geochemical reconnaissance sampling procedures, and one sample was obtained every 10 square kilometers. This traditional method, which has become an established technique, has proven to be an efficient method for identifying anomalous regions and mineral outcrops in the preliminary stages of exploration. The present study uses the metal contents of Cu, Pb, Zn, Co, Ni, Mn, Li, K, Fe, and Cr at 282 sampling points (see Fig. 3.1 for their

distribution). Table 3.2 summarizes the descriptive statistics of the geochemical data at the 282 sample locations. According to the report, atomic absorption spectroscopy was used to examine the content of all metal elements.

3.3. Methods

3.3.1. Image processing for atmospheric and topographic correction

One image of the Landsat ETM+ at path 126 and row 61, which was acquired on August 15, 2002 and obtained from the U.S. Geological Survey Earth Resources Observation and Science Center's Landsat archive, was selected for this study. The cloud cover over the study area is nearly 0%. The image used in this research was taken from the Level 1 Terrain-Corrected (L1T) data. The L1T data provides systematic geometric and radiometric accuracy by utilizing ground control points and the digital elevation model (DEM) to attain absolute geodetic accuracy. The image was processed using the Exelis Visual Information Solutions (ENVI) software to determine the surface reflectance by following steps. First, converts the digital number (DN) into radiance data, and then corrects atmospheric occurrences via a fast line-of-sight atmospheric analysis of hypercubes (FLAASH), which transforms the radiance of each pixel into a reflectance value. The parameter model in the FLAASH module is based on a tropical atmosphere and rural aerosol conditions with 2-band (K-T) aerosol retrieval.

Next is topographic correction to correct the brightness distortion caused by the change in the sun's illumination with the slope gradient (θ_p) and slope aspect (ϕ_o). The topographic correction used in this study was based on a model of the illumination condition of the study area. This method requires data analyzed by the DEM, which in this study were obtained from a shuttle radar topographic mission (SRTM) with a 90 m spatial resolution (Jarvis et al., 2008).

The DEM data were used to compute the incident angle (γ_i) for the model illumination (IL) conditions based on Civco's (1989) equation:

$$IL = \cos \gamma_i = \cos \theta_p \cos \theta_z + \sin \theta_p \sin \theta_z \cos(\phi_a - \phi_o) \quad (3.1)$$

where θ_z and ϕ_a are the solar zenith angle and solar azimuth angle, respectively. The following C-correction method, a non-Lambertian technique, was used to calculate the horizontal reflectance, ρ_H (Teillet et al., 1982):

$$\rho_H = \rho_T \left(\frac{\cos \theta_z + c_k}{IL + c_k} \right) \quad (3.2)$$

where ρ_T is the reflectance of an inclined surface and c_k is a coefficient to relate ρ_T at band k to IL by linear regression; $\rho_T = b_k + m_k IL$, where b_k and m_k are the regression coefficients and $c_k = b_k / m_k$. Furthermore, to reduce overcorrection in low IL conditions, the modified C-correction used by Riaño et al. (2003), which smooths IL values, was adopted. This method was proven to be the most effective method of mapping vegetation types.

3.3.2. Supervised classification

A supervised maximum likelihood (ML) classification method was chosen to classify pixels by generating their properties. The ML classification method is derived from Bayes' theorem, which describes the probability that the correct class is ω_i for a pixel with value x (Richards & Jia, 2006).

$$p(\omega_i|x) = p(x|\omega_i)p(\omega_i)/p(x) \quad (3.3)$$

where $p(x|\omega)$ is the probability function given from training data, $p(\omega_i)$ is the probability that class ω_i occurs in the image, and $p(x)$ is the probability of finding a pixel from any class with value x , which results in the following equation:

$$p(x) = \sum_{i=1}^M p(x|\omega_i)p(\omega_i) \quad (3.4)$$

The classification rule used to assign class ω_i at pixel x is:

$$x \in \omega_i \text{ if } p(x|\omega_i)p(\omega_i) > p(x|\omega_j)p(\omega_j) \text{ for all } j \neq i \quad (3.5)$$

It is often assumed that the probability distributions for the classes are normal multivariate models. If this is true, then the ML classification method can be implemented by calculating the following functions for each pixel in the image:

$$g_i(x) = \ln p(\omega_i) - \frac{1}{2} \ln |\Sigma_i| - \frac{1}{2} (x - m_i)^t \Sigma_i^{-1} (x - m_i) \quad (3.6)$$

where i is the class, x is n -dimensional data (n is the number of bands), $|\Sigma_i|$ is the determinant of the covariance matrix of the data in class ω_i , and m_i is the mean vector.

A supervised ML classification based on each Landsat band's surface reflectance was performed to create a land cover map based on plant formations by referring to information from the land use map (Bakosurtanal, 1986) and vegetation maps (Blasco et al., 1986). Furthermore, DEM data was used to characterize the topography of the forest region, which was determined by the land use classification. Fig. 3.4 shows the resultant map, which classifies the land cover as submontane forest, primary forest at low to medium altitude, secondary forest, and plantations, as well as other classifications that were unrelated to vegetation (paddy field, urban area, bare soil, and water). All the forest types are composed of dense, moist, evergreen vegetation (Laumonier et al., 1986).

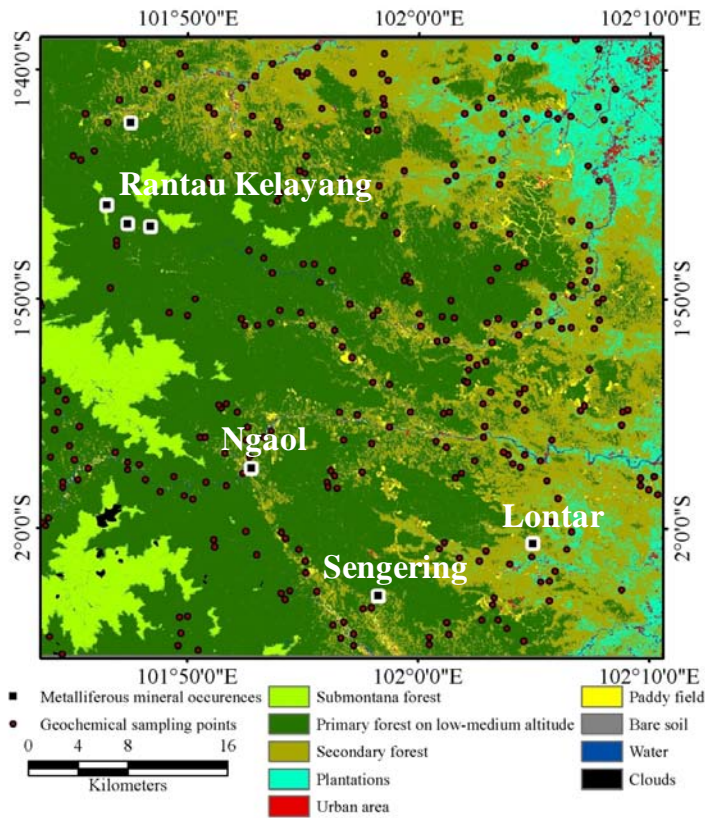


Fig. 3.4. Land cover map of plant formations and other categories produced by the maximum likelihood supervised classification of a Landsat ETM+ image.

3.3.3. Statistical analysis

An exploratory analysis was carried out to investigate the influence of spatial components and detect outliers in the geochemical data. A principal component analysis (PCA) was used to clarify the interrelations among the geochemical elements. The correlation between the geochemical data and the average vegetation reflectance was quantified by two approaches, simple linear regression and multivariate statistics via PLSR. In this study, the geochemical data and the reflectance data from selected bands are used as dependent and explanatory variables, respectively. A Pearson's correlation analysis between measured and predicted values was adopted to compare measured and predicted values in the cross-validation.

PLSR is a multivariate statistics analysis that generalizes and combines between PCA and multiple regressions that can handle multivariable of response and explanat simultaneously. PLSR has been used not only in economic studies but also in geological studies, which used it to analyze the abundance of minerals in the soil via reflectance values (Kooistra et al., 2001; Pandit et al., 2010). PLSR can be explained as follows. Suppose X is an $n \times m$ matrix for n samples with m variables and Y is an $n \times p$ matrix for n samples with p variables. PLSR techniques try to find a linear decomposition of X and Y , so:

$$\begin{aligned} X &= TP^T + E \\ Y &= UQ^T + F \end{aligned} \quad (3.7)$$

where T and P^T are the score matrix and the loading matrix for decomposing X , respectively, similar to U and Q^T , which are used to decompose Y . E and F are the residual values for X and Y , respectively. T and P are $n \times k$ and $m \times k$, respectively, while U and Q are $n \times l$ and $p \times l$, respectively. The PLSR procedure extracts factors of X and Y such that covariance between the extracted factors is maximized (Sumeet & Chowriappa, 2012). Application of PLSR in XLSTAT, a statistical analysis add-in for Microsoft Excel was used for the PLRS.

3.4. Results and discussion

3.4.1. Characterization of geochemical data

PCA reduced the 10 variables (element contents) into 7 principal components. The first three principal components represent 72.94% of the total variance of the data set: factor 1 (F1, 36.69%), factor 2 (F2, 23.18%), and factor 3 (F3, 13.08%). Fig. 3.5 shows the biplot scores of F1-F2 and F2-F3. The relations among these elements, which were determined based on a PCA analysis, can be explained as follows. F1 corresponds positively with all the metal elements, and

F2 describes the geological conditions of the study area. There is a strong relation among Ni-Cr-Li-K, which mainly originates from the southern part of the study area. This area is dominated by Jurassic-Cretaceous metasediments that are composed of quartzite, pelitic shale, and siltstone. Another strong relation was found for Cu-Fe-Co, which was derived from blocks of Permian rocks. Other metals, such as Pb-Zn-Mn, were mainly derived from intrusive and volcanic rocks, and they tend to have undergone secondary enrichment in the Tertiary and Quaternary sediment units (see Fig. 3.2 for their distributions).

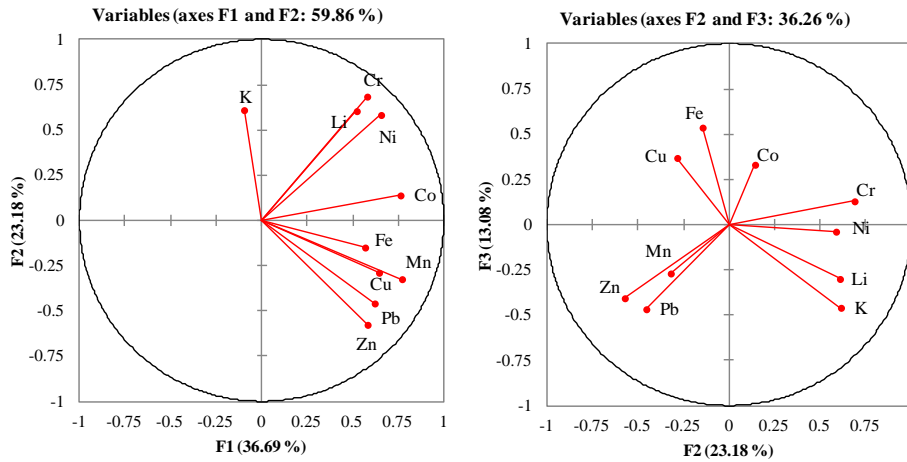


Fig. 3.5. Biplot scores of F1-F2 and F2-F3 obtained from PCA analysis.

3.4.2. Relation between geochemical data and vegetation reflectance

Generally, vegetation is sensitive to environmental conditions, including substrate materials. Nutrient absorption and accumulation in vegetation depends on the physical factors of the soil, such as structure and acidity (Karr and Mouat, 1990). Among the ten target elements, K is a macronutrient and Cu, Zn, Mo, Mn, and Fe are micronutrients. The other elements, such as

Ni, Cr, and Co, are not essential elements but are absorbed in plant tissues, and thus may affect photosynthesis.

Carranza & Hale (2001) performed similar studies by correlating the mean DN value of the Landsat bands and the mean NDVI value of the vegetation pixels based on catchment basins. However, the results showed very low correlation values, possibly because the influence of the catchment basins was too wide, considering the external factors that contributed to the reflectance value and geochemical content. Thus, this study used a different approach. A constant distance of 90 m from the sampling site was chosen as the range of influence to encompass the dispersion patterns of the geochemical survey data and to restrict dilution from the external factors affecting the vegetation conditions. Fig. 3.6 illustrates pixels that were used to calculate an average vegetation (in this case, the pixels represent primary forest at a low–medium altitude) reflectance value using a circular region at one geochemical sampling site.

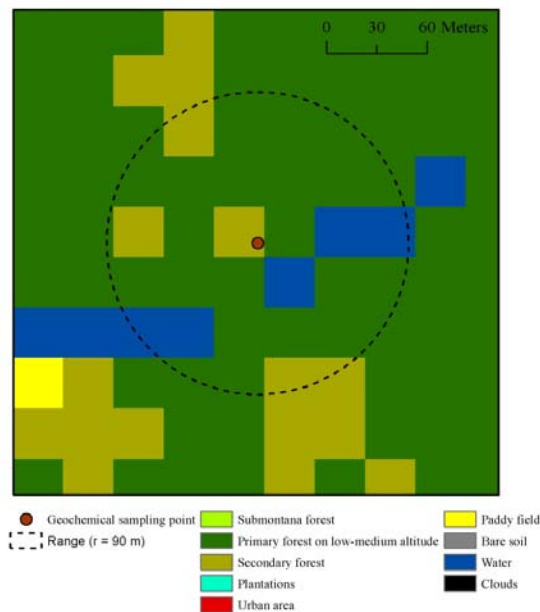


Fig. 3.6. A schematic spatial overview of the average reflectance value using a circular area of influence.

Table 3.3 shows the correlation coefficient matrix of the element content and spectral attributes (average reflectance values) at six ETM+ bands, but not the thermal band (band 6). Positive and negative correlations are mixed. This confirms that these elements can affect the spectral response of vegetation. For example, Cu has a strong positive correlation for almost all the bands, except band 3, which signifies that the Cu substrate affected the chlorophyll degradation and water absorption of plants. Ni revealed strong negative correlations at visible bands (bands 1, 2, and 3), signifying that the Ni substrate is related to chlorophyll absorption.

Table 3.3. Pearson correlation coefficients between the element content and reflectance of the Landsat ETM+ band at the pixel corresponding with the sample point ($n = 201$). Values in bold are different from 0 with a significance level $\alpha=0.05$.

Variables	B1	B2	B3	B4	B5	B7
Cu	0.166	0.189	0.094	0.189	0.269	0.283
Pb	0.161	0.218	0.126	0.249	0.249	0.239
Zn	0.167	0.142	0.125	0.110	0.196	0.229
Co	-0.005	0.179	0.095	0.225	0.266	0.266
Ni	-0.445	-0.207	-0.164	-0.158	-0.131	-0.127
Mn	-0.058	0.118	0.047	0.203	0.226	0.233
K	-0.313	-0.124	-0.090	-0.047	-0.109	-0.132
Li	-0.393	-0.135	-0.112	-0.117	-0.057	-0.036
Cr	-0.397	-0.145	-0.131	-0.056	-0.080	-0.089
Fe	0.184	0.214	0.102	0.229	0.224	0.216

The above results are common to the pixels that correspond to the vegetation category in the forest region. To obtain more accurate correlations, the sample locations need to be segmented by considering the hydraulic condition of the topsoil, which in this case is the soil's permeability. The effect of the element contents on the reflectance using selected segmentation is summarized in Table 3.4. Four metals, Cu, Zn, Ni, and K, have a strong correlation with the

reflectance at bands 4 and 5. Cu and Zn have a positive correlation, which leads to the interpretation that chlorosis and water stress occur as an effect of metal absorption. Additionally, the leaf reflectance decreases gradually with increasing Ni and K concentrations. The metals that were derived from the Permian and intrusive rocks (e.g., Cu, Pb, Zn, Co, and Mn) tend to have lower vegetation reflectance values in the SWIR (bands 5 and 7). Overall, the correlation values shown in Tables 3.3 and 3.4 are low, implying that the effect of the metal contents may result in a weak enhancement of the correlation of vegetation reflectance.

Table 3.4. Pearson correlation coefficient between the element content and reflectance of Landsat ETM+ band for the selected samples located in the selected area, which is covered by primary forest and without exploitable groundwater pixels. Values in bold are different from 0 with a significance level $\alpha=0.05$.

Variables	B1	B2	B3	B4	B5	B7
Cu	0.309	0.227	0.107	0.197	0.291	0.301
Pb	0.213	0.169	0.092	0.159	0.189	0.194
Zn	0.327	0.197	0.178	0.102	0.208	0.238
Co	0.034	0.164	0.067	0.230	0.256	0.251
Ni	-0.411	-0.257	-0.183	-0.235	-0.238	-0.250
Mn	0.018	0.094	0.034	0.171	0.190	0.195
K	-0.390	-0.209	-0.152	-0.100	-0.187	-0.210
Li	-0.319	-0.164	-0.138	-0.166	-0.143	-0.145
Cr	-0.392	-0.190	-0.153	-0.107	-0.157	-0.173
Fe	0.210	0.160	0.059	0.166	0.169	0.167

To show the aforementioned relationship more clearly, Table 3.5 was created to show that the reflectance values of vegetation vary with the metal content. Each graph was produced by averaging the spectral attributes of the same ETM+ band that are in the same content range, such as 10 to 100 ppm. For Cu and Zn, the mean reflectance values result in overall enhancement with

an increase of content, while Ni and K show the reverse characteristics. This condition may reveal the relationship between metals that was explained in section 3.4.1. There are high contents of Cu and Zn in intrusive rocks, while high quantities of Ni and K were found in metasedimentary rocks. Regardless of whether their contents increase or decrease, these four metals affect the reflectance values. For all four elements, the most remarkable change in the reflectance with the concentration occurred at NIR (band 4) in response to the internal structure of the leaves. The vegetation response varies with the metal concentration, and the degree of the response of a specific element may not be the same for different concentrations (Karr & Mouat, 1990).

Table 3.5. Mean reflectance values in Landsat ETM+ bands with different metal concentrations.

Metal	Content (ppm)	Number	B1	B2	B3	B4	B5	B7
Cu	0–20	34	0.010	0.026	0.017	0.281	0.117	0.044
	20–60	63	0.010	0.027	0.017	0.280	0.121	0.046
	> 60	15	0.011	0.028	0.017	0.295	0.129	0.049
Zn	0–100	74	0.010	0.027	0.017	0.282	0.120	0.045
	100–200	30	0.010	0.026	0.017	0.280	0.120	0.045
	> 200	8	0.012	0.029	0.018	0.291	0.131	0.051
Ni	0–20	55	0.011	0.027	0.017	0.285	0.123	0.047
	20–40	33	0.010	0.027	0.017	0.282	0.121	0.046
	> 40	24	0.009	0.026	0.016	0.275	0.116	0.044
K	0–10,000	26	0.011	0.028	0.017	0.290	0.127	0.048
	10,000–20,000	42	0.010	0.027	0.017	0.280	0.120	0.045
	> 20,000	44	0.009	0.026	0.017	0.280	0.118	0.045

3.4.3. PLSR analysis

The above vegetation reflectance–metal relations indicate there is a possibility to determined metal content through vegetation reflectance values. To this end, a PLSR analysis was conducted for Cu, Zn, Ni, and K using 112 sampling sites. The geochemical data and the

reflectance data from the selected bands are used as dependent and explanatory variables, respectively. Data were split into two categories: the training set for deriving the PLSR algorithm and the validation dataset that was used to ensure predictive accuracy. Fig. 3.7 presents the results of the PLSR analysis, which was based on Pearson's correlation coefficient, of the correlations of the metal contents (Cu, Zn, Ni, and K). The slightly higher correlations found by the PLSR analysis suggests that it is possible to detect metal-enriched zones in the forest area by the reflectance values of the Landsat-series imagery.

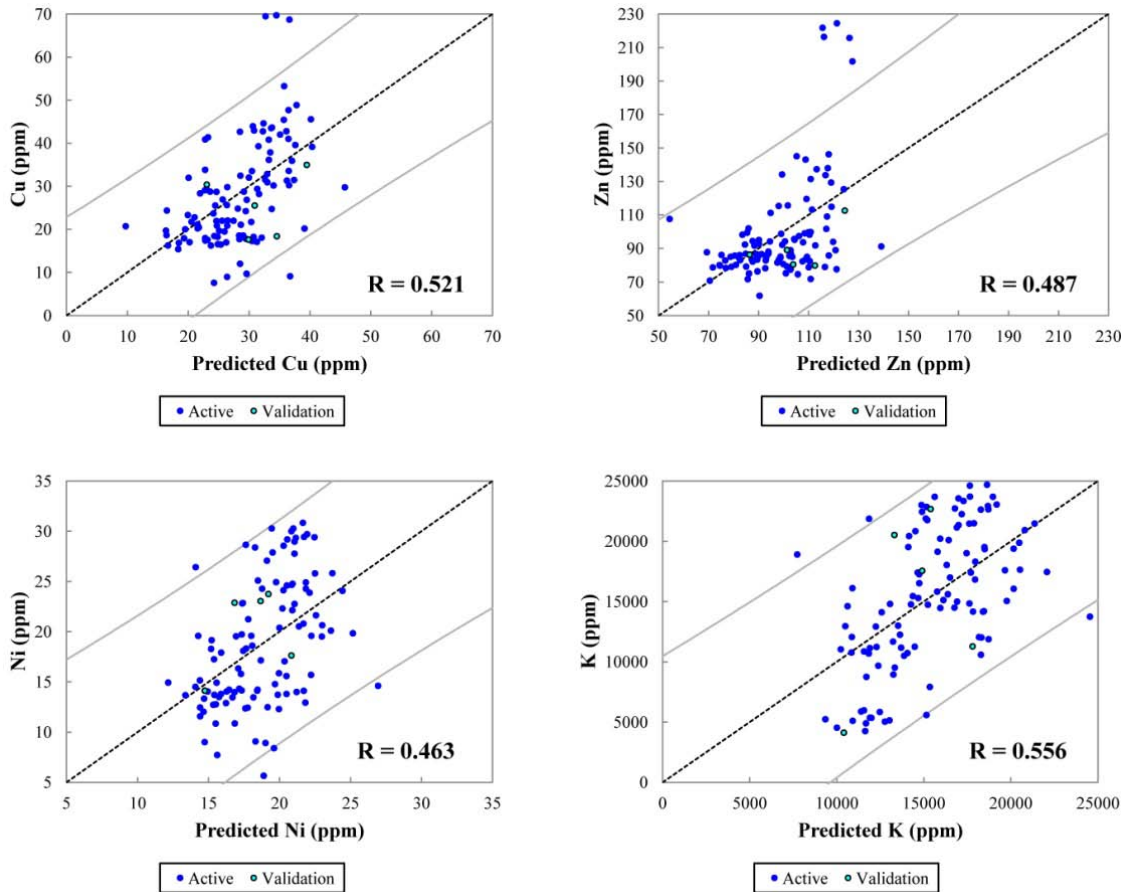


Fig. 3.7. Performance of the correlations of the metal contents (Cu, Zn, Ni, and K) and PLS model.

3.5. Conclusions

This study demonstrated the possibility of detecting geochemically-enriched zones through vegetation-reflectance properties under natural conditions. The analysis was conducted by correlating the reflectance values derived from satellite imagery (Landsat ETM+ image) with geochemical data. This relationship was also examined by a partial least squares regression (PLSR) analysis. The main results were as follows.

- A Pearson's correlation analysis of the reflectance values and metal contents showed slightly higher correlations between the metal content of Cu, Zn, Ni, and K and the reflectance of all ETM+ bands, except for the thermal band, compared with other metals.
- Weak correlations with Pb, Co, Mn, Li, Cr, and Fe content occurred at the limited bands.
- The slightly higher correlations found by the PLSR analysis suggest that it is possible to detect enriched zones in forest areas by the reflectance values of the Landsat-series imagery.

Next chapter is discussed more accurately by identified possible control factors on the canopy vegetation activity before a consideration of the metal content effect on the spectral features and applying VI for detecting vegetation stress in metal-enriched zones.

References

- Bakosurtanal. (1986). Indonesia land cover map, scale 1:250.000. National Coordinating Agency for Surveys and Mapping (Bakosurtanal). Bogor, Indonesia.
- Blasco, F., Laumonier, Y., Purnadjaja, & Setiabudhi. (1986). International map of the vegetation and the environmental nonditions. Central Sumatra. Sheet no. 2. Institut De La Carte Internationale Du Tapis Vegetal / SEAMEO-BIOTROP. Toulouse, France.
- Boluda, R., Andreu, V., Gilabert, M. A., & Sobrino, P. (1993). Relation between reflectance of rice crop and indeces of pollution by heavy-metals in soils of Albufera natural park (Valencia, Spain). *Soil Technology*, 6, 351–363.

- British Geological Survey. (2007). Indonesia regional geochemical survey (CD-ROM): Sumatra. Version 3.0. Keyworth, Nottingham, UK.
- Carranza, E. J. M., & Hale, M. (2001). Remote detection of vegetation stress for mineral exploration. *Geoscience and Remote Sensing Symposium, 2001. IGARSS '01. IEEE 2001 International Geoscience and Remote Sensing Symposium*, 3, 1324–1326. <http://doi.org/10.1109/IGARSS.2001.976833>
- Civco, D. L. (1989). Topographic normalization of Landsat Thematic Mapper digital imagery. *Photogrammetric Engineering and Remote Sensing*, 55, 1303–1309.
- Crow, M. J., Johnson, C. C., McCourt, W. J., & Harmanto. (1993). The simplified geology and known metalliferous mineral occurrences, Painan quadrangle Southern Sumatra. *Special Publication of the Directorate of Mineral Resources, No. 52-B*. Bandung.
- Jarvis, A., Reuter, H. I., Nelson, A., & Guevara, E. (2008). Hole-filled seamless SRTM data V4. Retrieved December 4, 2014, from <http://srtm.csi.cgiar.org>
- Karr, L., & Mouat, D. (1990). A biogeochemical and spectral analysis of vegetation affected by external abiotic agents results of an investigation from Kitsap County, Washington. Port Hueneme, California: Naval Civil Engineering Laboratory.
- Kooistra, L., Salas, E. A. ., Clevers, J. G. P. ., Wehrens, R., Leuven, R. S. E. ., Nienhuis, P. ., & Buydens, L. M. . (2004). Exploring field vegetation reflectance as an indicator of soil contamination in river floodplains. *Environmental Pollution*, 127(2), 281–290. [http://doi.org/10.1016/S0269-7491\(03\)00266-5](http://doi.org/10.1016/S0269-7491(03)00266-5)
- Kooistra, L., Wehrens, R., Leuven, R. S. E. ., & Buydens, L. M. . (2001). Possibilities of visible–near-infrared spectroscopy for the assessment of soil contamination in river floodplains. *Analytica Chimica Acta*, 446(1-2), 97–105. [http://doi.org/10.1016/S0003-2670\(01\)01265-X](http://doi.org/10.1016/S0003-2670(01)01265-X)
- Laumonier, Y. (1997). *The vegetation and physiography of Sumatra*. (M. J. A. Werger, Ed.). Dordrecht: Springer Netherlands. <http://doi.org/10.1007/978-94-009-0031-8>
- Pandit, C. M., Filippelli, G. M., & Li, L. (2010). Estimation of heavy-metal contamination in soil using reflectance spectroscopy and partial least-squares regression. *International Journal of Remote Sensing*, 31(15), 4111–4123. <http://doi.org/10.1080/01431160903229200>
- Kusnama, Pardede, R., Mangga, S. A., & Sidarto. (1992). Geological map of the Sungaipenuh and Ketaun quadrangle, Sumatra. Geological Research and Development Centre. Bandung, Indonesia.

- Richards, J. A., & Jia, X. (2006). *Remote Sensing Digital Image Analysis*. New York. [http://doi.org/10.1016/S0169-555X\(01\)00164-7](http://doi.org/10.1016/S0169-555X(01)00164-7)
- Rosidi, H. M. D., Tjokrosapoetro, S., Pendowo, B., Gafoer, S., & Suharso. (1996). Geological map of the Painan and northeastern part of the Muarasiberut quadrangle, Sumatra. Geological Research and Development Centre. Bandung, Indonesia.
- Setiawan, T., Tirtomihardjo, H., & Harnandi, D. (2013). Hydrogeological map of Indonesia, Muarabungo, Sumatra. Geological Agency. Bandung, Indonesia.
- Simandjuntak, T. O., Budhitrisona, T., Gafoer, S., & Amin, T. C. (1994). Geological map of the Muarabungo quadrangle, Sumatra. Geological Research and Development Centre. Bandung, Indonesia.
- Sukiban, S. (2005). Hydrogeological map of Indonesia, Muarasiberut and Painan, Sumatra. Directorate of Geological and Mining Area Environment. Bandung, Indonesia.
- Sumeet, D., & Chowriappa, P. (2012). Feature Selection and Extraction Strategies in Data Mining. In *Data Mining for Bioinformatics* (pp. 113–144). CRC Press. <http://doi.org/doi:10.1201/b13091-7>
- Suwarna, N., Suharsono, Gafoer, S., Amin, T. C., Kusnama, & Hermanto, B. (1992). Geological map of Sarolangun quadrangle, Sumatra. Geological Research and Development Centre. Bandung, Indonesia.
- Teillet, P. M., Guindon, B., & Goodenough, D. G. (1982). On the slope-aspect correction of multispectral scanner data. *Canadian Journal of Remote Sensing*, 8(2), 84–106. <http://doi.org/10.1080/07038992.1982.10855028>
- USGS. (1998). *Landsat 7 science data users handbook*. USGS Unnumbered Series General Interest Publication (Revised ed). Retrieved from <http://pubs.er.usgs.gov/publication/7000070>
- Yudhanagara, D. (2005). Hydrogeological map of Indonesia, Ketaun and Sungaipenuh, Sumatra. Directorate of Geological and Mining Area Environment. Bandung, Indonesia.
- Zahirdin, R. M., & Hendra W, M. T. (1982). Hydrogeological map of Indonesia, Bangko, Sumatra. Directorate of Environmental Geology. Bandung, Indonesia.

Chapter 4

Application of a new vegetation index to detecting vegetation anomaly due to metals enrichment in a tropical forest

4.1. Introduction

As inferred from Chapter 1, the GBRs study requires an understanding of the physical evaluations in relation to vegetation spectral analysis. These evaluations may include; edaphic factors (e.g., metal content, type of lithologies, and hydraulic condition of top soils), environmental influences, topographic features, and plant physiological factors. Obviously, correlate directly point to point or pixel by pixel between geochemical data and spectra or VI in a specific position will give low correlation result as presented in Chapter 3. This condition indicates raw geochemical data from stream sediment sampling cannot be used directly to correlate with vegetation reflectance at specific point or pixel. Stream sediment sampling usually took locations in the drainage systems with some criterions such as in slow flowing water, away from the stream bank, and in shallow water. However, regional geochemical distribution represent lithology and soil condition, and may affect to vegetation condition.

In this chapter, VIGS has developed in Chapter 2 is applied to a Landsat ETM+ imagery in a tropical forest, Jambi, Sumatra, Indonesia where mineral deposits of copper porphyry are existed and mineralized zones are distributed in places (data set as shown in Chapter 3). A set of soil geochemical data is used as a ground-truth to evaluate positional concordance of the VI anomalies derived from the imagery with the soils of high metal concentration. Through this case

study, applicability of GBRS using the new VI to mineral deposits exploration in densely vegetated areas will be discussed.

4.2. Methodology and data processing

4.2.1. Geochemical spatial data distribution

The same data as mentioned in Chapter 3 is used in this chapter. However, only three metals selected (Cu, Pb, Zn) considering their significant anomaly compared others metals in this region. The content data of three metals (Cu, Pb, and Zn) at 282 sampling points were selected and transformed into natural logarithms to reduce the bias of content distribution and approximate it to a normal distribution for subsequent geostatistical analysis. Geostatistics has been a common method to make a regional scale geochemical model using point sample data collected over several years (e.g., Conradsen et al. (1992)). Histograms and Q-Q plots of the log-transformed data show that they roughly follow a normal distribution (Fig. 4.1).

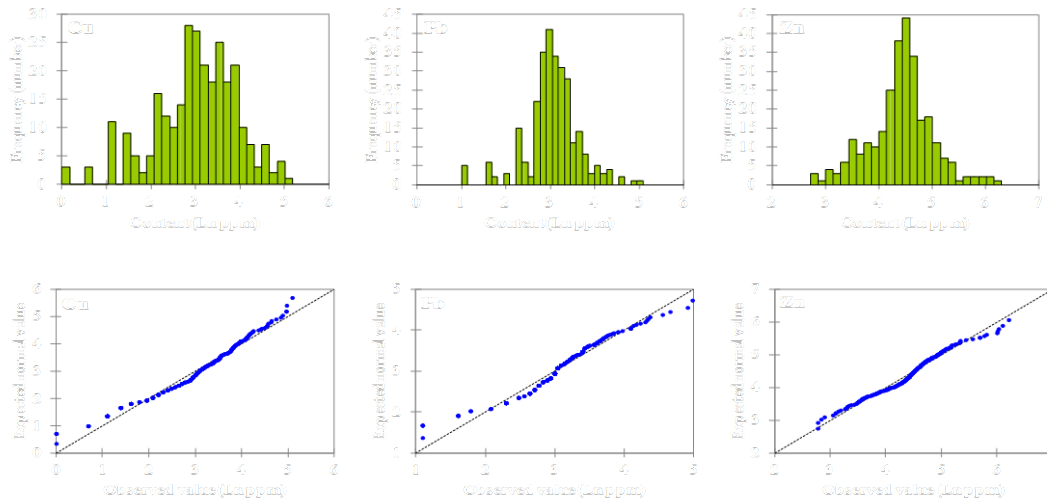


Fig. 4.1. Histograms and Q-Q plots of log-transformed contents of Cu, Pb, and Zn at sampling sites.

First, spatial correlation of the content data was clarified by semivariogram, $\gamma(\mathbf{h})$, by assuming that the content data of each metal were stationary and intrinsic random variables, $Z(\mathbf{x})$:

$$\gamma(\mathbf{h}) = \frac{1}{2} E[Z(\mathbf{x} + \mathbf{h}) - Z(\mathbf{x})]^2 \quad (4.1)$$

where \mathbf{x} and \mathbf{h} denote sampling coordinate in the space and a vector connecting the two locations, respectively, and E means expectation. Directional semivariograms were constructed along four directions (E-W, N45°E, N-S, and N45°W) for the metals content. Simple kriging (SK) or ordinary kriging (OK) was used for estimating the metal contents over the study area using the $\gamma(\mathbf{h})$ model. The choice of SK or OK was dependent upon the cross-validation on which method generate higher estimation accuracy. Detail of kriging analysis can be explained as follows. Kriging is a common method used of interpolation (prediction) for spatial data where the basic formula of kriging is:

$$z_k^* = \sum_{i=1}^n \lambda_i z_i \quad (4.2)$$

z_k^* : estimation, l_i : weight for i -th data, n : number of data used for kriging. Kriging in its simplest form is simple kriging (SK). SK assigns weights, λ_j ($j=1, 2, \dots, N$), to N sample data which can be obtained by the following set of linear equations:

$$\sum_{j=1}^N \lambda_j \gamma(\mathbf{x}_i, \mathbf{x}_j) = \bar{\gamma}(\mathbf{x}_i, V), \quad i = 1, \dots, N \quad (4.3)$$

where $\gamma(\mathbf{x}_i, \mathbf{x}_j)$ is semivariogram between points \mathbf{x}_i and \mathbf{x}_j , and $\bar{\gamma}(\mathbf{x}_i, V)$ is average of the semivariogram between point \mathbf{x}_i and cell V . The minimum variance of the estimation error (kriging variance) is:

$$\sigma_{SK}^2 = \sum \lambda_i \bar{\gamma}(\mathbf{x}_i, V) - \bar{\gamma}(V, V) \quad (4.4)$$

Ordinary kriging (OK) is a variant of SK algorithm that can be obtained by solving the following equations:

$$\left. \begin{aligned} \sum_{j=1}^N \lambda_j \gamma(\mathbf{x}_i, \mathbf{x}_j) + \mu &= \bar{\gamma}(\mathbf{x}_i, V), \quad i = 1, \dots, N \\ \sum_i \lambda_i &= 1 \end{aligned} \right\} \quad (4.5)$$

where μ is Lagrange multiplier. The kriging variance is:

$$\sigma_{OK}^2 = \sum \lambda_i \bar{\gamma}(\mathbf{x}_i, V) - \bar{\gamma}(V, V) + \mu \quad (4.6)$$

where $\bar{\gamma}(V, V)$ is mean of semivariograms for all the point pairs considered within V . The $\gamma(\mathbf{x}_i, \mathbf{x}_j)$, $\bar{\gamma}(\mathbf{x}_i, V)$, and $\bar{\gamma}(V, V)$ are derived from the semivariogram spherical models that approximate the experimental semivariograms.

Then, the concentration–area (C–A) model (Cheng et al., 1994) was applied to extract the anomaly zones in the metal content map by kriging. The model is expressed by:

$$A(r > r_i) = cr_i^{-D} \quad (4.7)$$

where $A(r > r_i)$ denotes the cumulative area of content r greater than or equal to a cutoff, r_i and c and D are a constant and scaling component, respectively of a regression line between $A(r > r_i)$ and r_i in log-log plots. The optimal threshold to separate background and anomaly was determined by inflection of the regression line, i.e. the metal content at which the D values changes abruptly.

4.2.2. VI calculation

I also use the same corrected Landsat ETM+ image as described in Chapter 3 for the image analysis. Next was VI calculation and recognizable display of the result following the procedure of Lyon et al. (1998):

- The VI values are calculated at all pixels of the image using the corrected reflectance and the values smaller than 0.2 % and greater than 0.2 % of the cumulative distribution were removed as outliers. The VIs calculation formula (NDVI and VIGS) as shown in Chapter 2 section 2.2.2.
- The remaining values are normalized to a Gaussian distribution with range 0 to 1 and mean 0.5. By this normalization, the NDVI and VIGS value could be compared.

Overall methodology in this chapter as presented in Fig. 4.2.

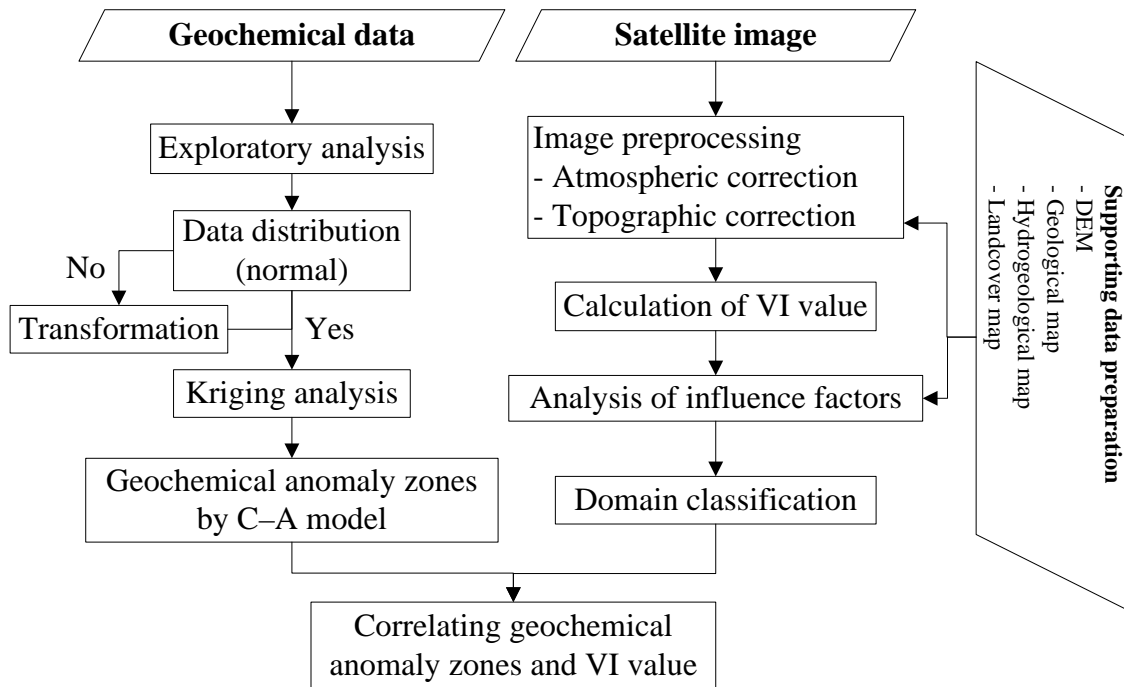


Fig. 4.2. Flow chart showing the research methodology.

4.3. Results

4.3.1. Spatial distribution of metal contents

All experimental $\gamma(h)$ of three metals fit well the spherical model (Fig. 4.3). The $\gamma(h)$ of Cu and Pb contents showed orthogonal anisotropic behavior with the major and minor axes along E–W and N–S, respectively, whereas the $\gamma(h)$ of Zn contents was isotropic. Details of the $\gamma(h)$ model and kriging method for each metal are summarized in Table 4.1.

Table 4.1. Semivariogram models and parameters of Cu, Pb and Zn content data (OK: ordinary kriging; SK: simple kriging).

Metal	Method	Model	Nugget	Sill	Azimuth of major/ minor axes	Range (km) along major/minor axes
Cu	OK	Spherical	0.335	0.84	E–W/N–S	55/24
Pb	OK	Spherical	0.195	0.15	E–W/N–S	45/14
Zn	SK	Spherical	0.171	0.31	–	34.5

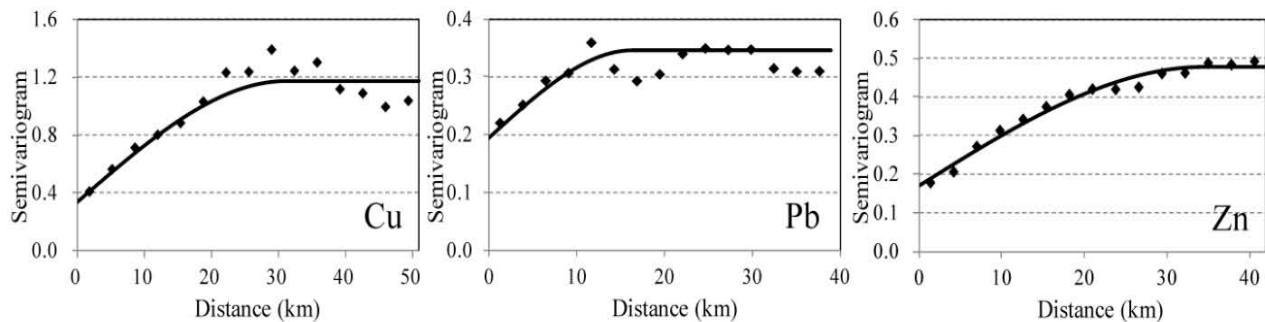


Fig. 4.3. Experimental semivariograms of log-transformed Cu, Pb, and Zn content data and approximation with the spherical model. Cu and Pb data are along the minor axes.

Spatial distributions of Cu and Pb contents were estimated by OK and Zn by SK (Fig. 4.4). It is obvious that these metal contents are strongly correlated with the geology and

controlled by the faults. For the three metals, high contents were mainly in the Permian intrusions and around an E–W fault in the central area. The high Cu and Pb contents showed clear continuity along the strike of major NW–SE faults. This trend was weak for the Zn contents, which were high along the N–S direction. The similarity of the Cu and Pb content distributions suggests that these metals originated from the same source in the Permian and Triassic–Cretaceous intrusive rocks. The contrasting trend of Zn content can be explained by secondary enrichment that occurred jointly with gold placer deposits (Crow et al., 1993). Including the Permian intrusions, the high content zones mostly originated in the intrusive rocks, associated with past volcanic activities.

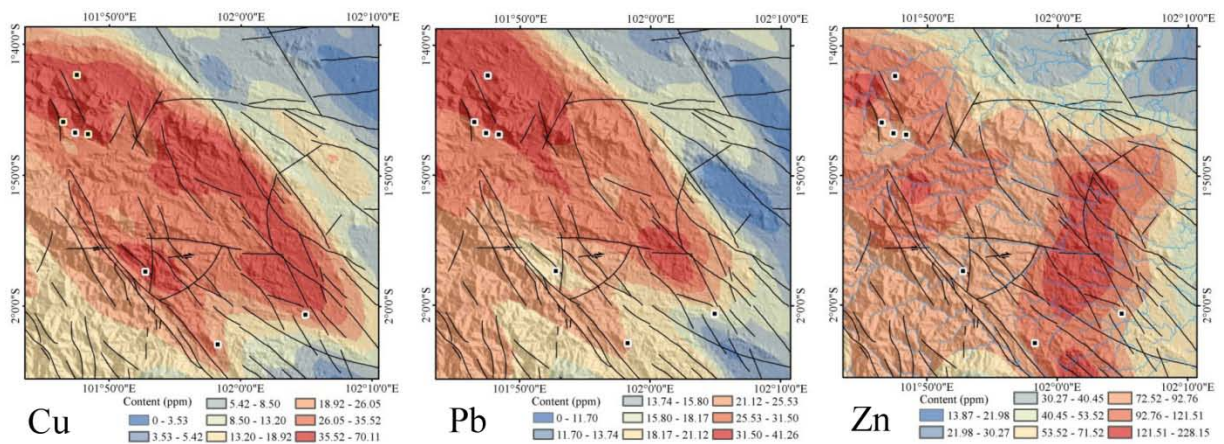


Fig. 4.4. Distributions of metal contents estimated by ordinary kriging (OK) for Cu and Pb and simple kriging (SK) for Zn. Black lines and circles here and in Fig. 4.6 show faults and metalliferous mineral occurrences, respectively.

To categorize content distributions (Fig. 4.4), C–A models of kriged metal contents were constructed, which are characterized as bi-fractal because C–A plots of all metals can be approximated by three segments with different gradients (Fig. 4.5). Using intersections of

adjacent two segments as thresholds, the contents were separated into three categories, low, medium and high. The C–A models are reasonable because the three categories are related to the geological units. The first segment corresponding to the low-content category is overlapped mainly by sediments and metasediments, whereas the other two segments (medium and high content categories) are in the Permian intrusion area (Fig. 4.6).

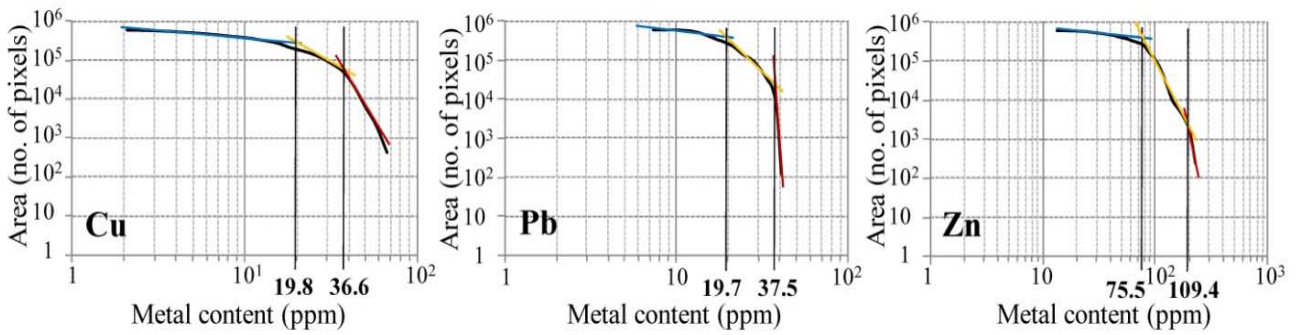


Fig. 4.5. C–A models of kriged metal contents in Fig. 4.4 and three segments for approximating the curves. Values at bottom indicated thresholds for three content categories, low, medium and high.

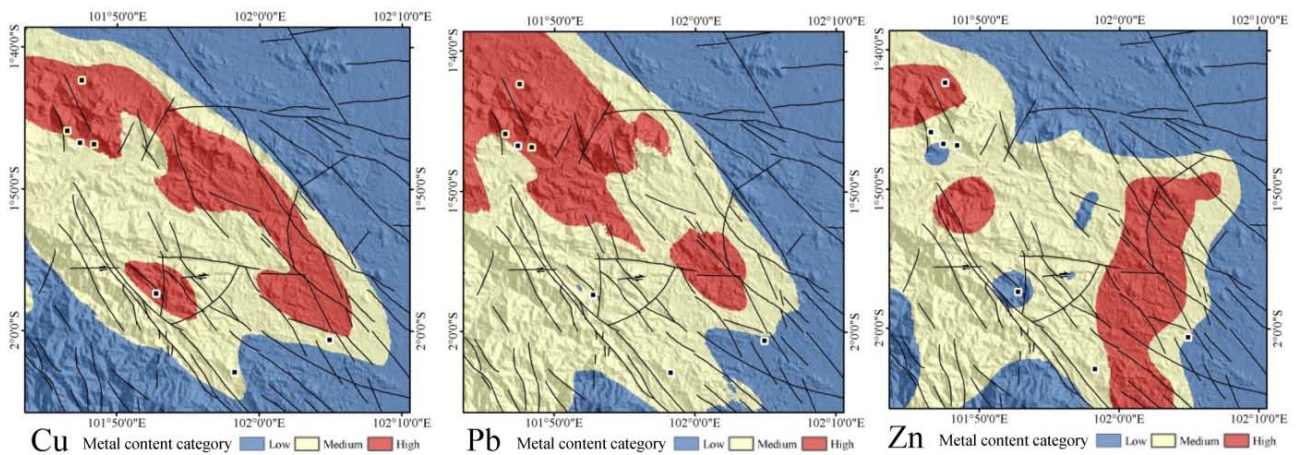


Fig. 4.6. Distributions of low, medium, and high content categories defined by C-A models in Fig. 4.5.

4.3.2. Relationship between VIs and control factors of vegetation stress

Distributions of NDVI and VIGS values from the Landsat ETM+ image were overlain on the geologic boundaries and faults (Fig. 4.7). Although the two distributions are similar, there are small differences, in that large NDVI values (> 0.5) almost completely overlap the vegetation area (see Fig. 3.1 in Chapter 3), whereas VIGS values are more variable, even in the vegetation area, probably because of intrinsic factors other than vegetation. The factors are identified as follows.

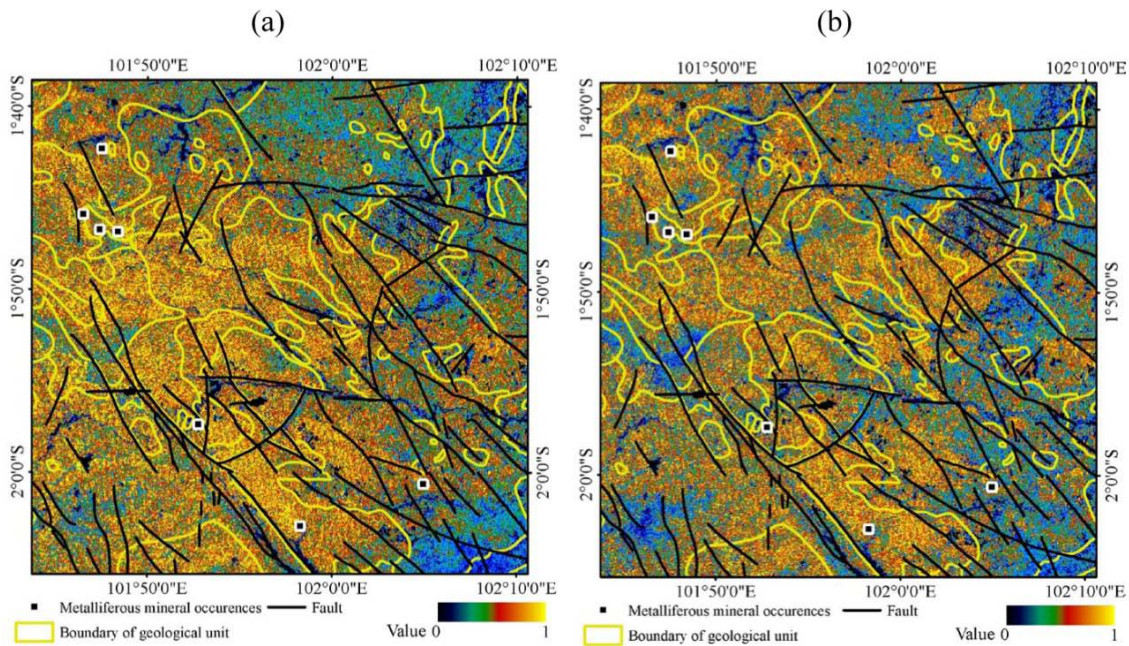


Fig. 4.7. Comparison of two maps showing (a) NDVI and (b) VIGS from Landsat ETM+ image acquired on 15 August 2002, superimposed on geologic boundaries and faults.

Several controls on vegetation activity are known, which are classified as internal factors such as leaf geometry and plant physiology, and external factors such as climatic conditions, solar illumination intensity, mineral nutrient supplies related to geology, and water supply (Bruce

& Hornsby, 1987; Koide & Koike, 2012). Therefore, the influence of each factor on the reflectance spectra must be examined over the study area.

First, to examine the effect of internal factors, the NDVI and VIGS are characterized by the relationship between their averages and land-cover type (Fig. 4.8). The two VI averages are almost identical, except that VIGS can enhance the difference between submontane forest and primary forest at low–medium altitude. From this figure, applicability of the VIGS as a VI can be confirmed in addition to the NDVI, because it satisfies the conditions that VI values should not be saturated in heavily vegetated areas and should be sensitive to land cover of green vegetation (Koide & Koike, 2012).

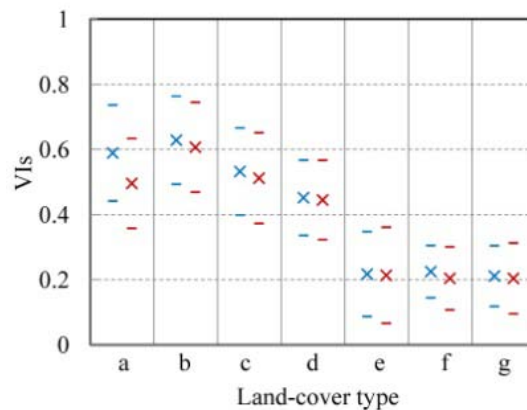


Fig. 4.8. Changes in NDVI (blue) and VIGS (red) for land-cover types, shown by averages (×) and standard deviations (bars above and below the average): (a) submontane forest; (b) primary forest at low-medium altitude; (c) secondary forest; (d) plantations; (e) paddy field; (f) bare soil; (g) urban area.

The average NDVI and VIGS were also related to elevation, slope gradient, and slope aspect, to examine the effect of the representative external factors climatic conditions and solar

illumination, by selecting the three natural forest types, submontane, primary, and secondary. NDVI and VIGS show almost the same trends and values for all three types in terms of elevation (Fig. 4.9); i.e., their values form gentle convex curves and have a maximum at 300 m a.s.l. This trend can be interpreted from the fact that plant formations of the Sumatra rain forest generally vary with elevation. The low elevation range below 300 m a.s.l. is occupied by mixed dipterocarp rain forests with trunk diameters > 30 cm, with 60% dominance across all plots. The dominance of the dipterocarp families decrease with elevation, but are still the most abundant in the medium elevation range 300–1,000 m a.s.l., coexisting with Fagaceae and Burseraceae (Laumonier, 1997). Despite the difference in dominance, plant formations in the low and medium elevations are traditionally grouped into the same type, primary forest. In the high elevation range over 1,000 m a.s.l., submontane forest composed of Fagaceae, Lauraceae, and Myrtaceae families is dominant.

A trend in which the NDVI and VIGS increase with slope gradient (Fig. 4.9b) may be caused by the crown shape of plants on slopes, because that shape can enhance the apparent crown density. For detailed characterization of the effect of aspect by considering the trend of slope gradient, the gradient was separated into gentle and steep groups, 0–15° and > 15°. Except for the submontane VIGS, NDVI and VIGS values tended to be smaller on the eastern aspects (N, NE, E, and SE) than those on the western aspects (S, SW, W, and NW) (Fig. 4.9c), which may be caused by solar azimuth. However, changes in the NDVI and VIGS with slope gradient and aspect were small, even smaller for VIGS for all forest types. This fact signifies that these effects on the reflectance spectra can be mitigated by the aforementioned topographic corrections, and this mitigation is more effective for the VIGS.

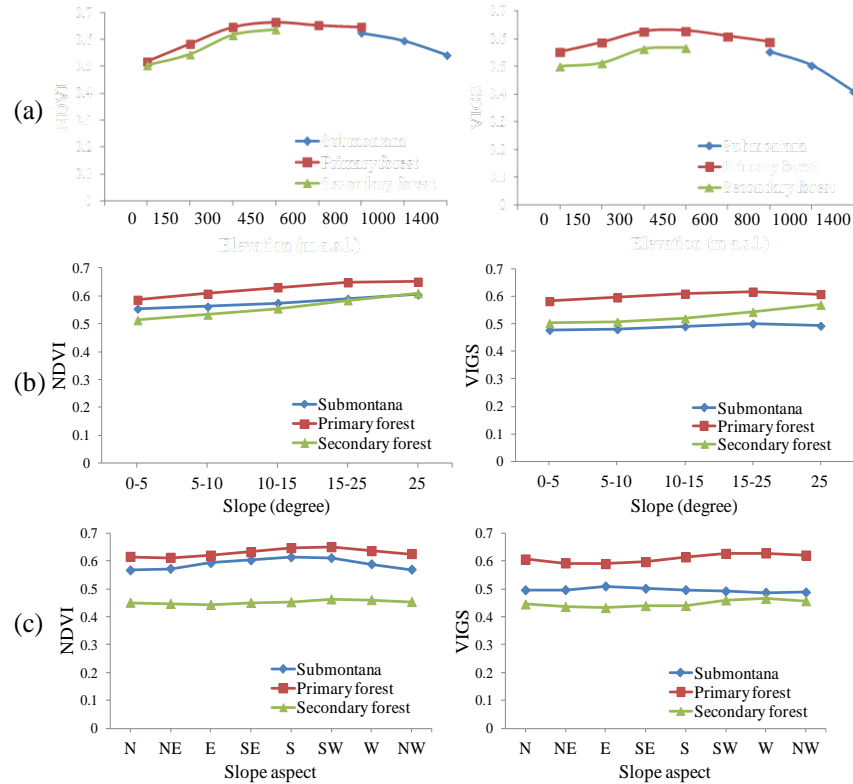


Fig. 4.9. Relationships of average NDVI and VIGS with (a) elevation, (b) slope gradient, and (c) slope aspect for three natural forest types.

Because the primary forest is the most common type, covering 54.6% of the study area, it was selected for analysis of the influence of geology on the reflectance spectra. Box plots of the NDVI and VIGS divided by the seven geological units (see Fig. 3.2 in Chapter 3 for their distributions) reveal that change of VIGS averages was less than that of NDVI. The VIGS averages for sedimentary and volcanic units (a, b, c, and e) were nearly identical and slightly smaller than the values for intrusive rocks (units d, f, and g) (Fig. 4.10a). The NDVI averages were more variable and inconsistent with the geological units. Therefore, the effect of geological unit on VI was more apparent in the only VNIR-based VI. However, this might conceal the effect of metal content in the soils. VIGS can avoid this risk.

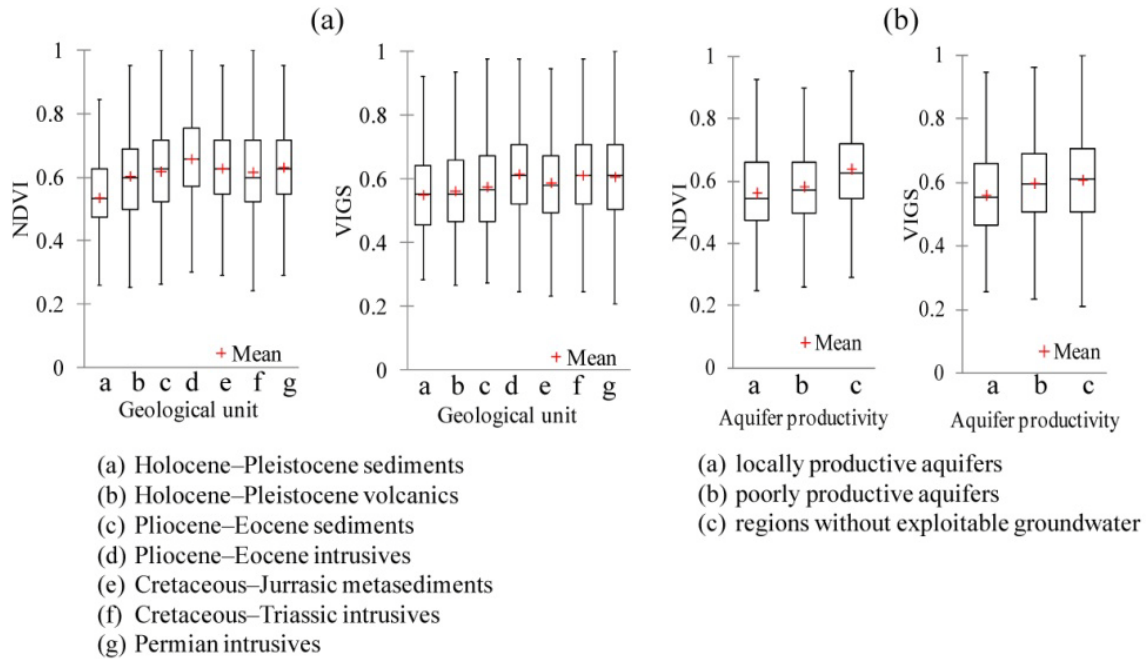


Fig. 4.10. Relationships of NDVI and VIGS of primary forest with (a) geological units and (b) three categories of aquifer productivity, shown as box plots.

Permeability of the top layer (see Fig. 3.3 in Chapter 3) is also a possible external factor of VI. The NDVI and VIGS in the primary forest show a similar trend, in which their averages increase with decreasing permeability (Fig. 4.10b: the c aquifer type has the lowest permeability). Although the differences in averages among the three categories were small, the change was smaller in VIGS than NDVI, as with the geological unit result. All the above external factors were confirmed to affect the VIs. Because the difference of VI values affected by the factors was small, a suitable categorization is necessary to minimize the effect of those factors and emphasize the effect of metal content, as examined in the next section.

4.3.3. Correlation of VIs with metal contents

To accurately evaluate the effect of soil metal content on VI by comparing NDVI and VIGS, an appropriate domain for the evaluation and comparison was defined from the aforementioned results of external factors elevation, slope gradient, slope aspect, and aquifer productivity. The factor geological unit was excluded here, because metal distributions were found to be strongly related with those units. Stability of VI values and the following featured parts of the factors were assumed to define the conditions for establishing the domain. One featured part is the area higher than 300 m a.s.l. and occupied by the primary forest, because NDVI and VIGS averages in that area were about the same, with patterns similar to those at low elevations and for the other forest types. This area was further limited to regions without exploitable groundwater, which is the most widespread (64.2 % of the study area) among the categories of aquifer productivity (see Fig. 3.3 in Chapter 3). Finally, four subdomains were defined from the two categories of slope gradient and aspect (Table 4.2).

Table 4.2. Conditions of VI control factors for selecting domain to correlate VI values with soil metal content in study area.

Plants formation	Elevation	Aquifer	Slope gradient	Slope aspect
Primary forest on low–medium altitude	>300 m a.s.l.	Regions without exploitable groundwater	0–15°	N, NE, E, and SE
			>15°	S, SW, W, and NW

Using the corrected Landsat ETM+ reflectances in the selected domain, average reflectances in the six bands were correlated with the three metal contents (low, medium, and high) in Fig. 4.6 (Table 4.3). Low Pb contents were not included because of a lack of data. Although the differences were small among the three contents of the three metals, reflectance increases with metal content generally appeared in the visible region, particularly in the visible

green (B2) region, which is sensitive to chlorophyll conditions. Additionally, the increase of reflectance in the SWIR region (B4, B5, and B7) concurs with the experimental result that suggested plant water stress from metal absorption. It is common for water stress as a secondary effect when a metal alters mineral nutrition, which may affect the photosynthesis system of plants after long exposure times (Poschenrieder & Barceló, 1999).

Table 4.3. Average reflectances of Landsat ETM+ bands after atmospheric and topographic corrections (B1–B5 and B7) and area for each metal content category. Details of the low, medium, and high categories are shown in Figs. 4.5 and 4.6. The selected area for this reflectance characterization is based on the domain classification listed in Table 4.2.

Slope gradient	Slope aspect		Eastern aspect (N, NE, SE, SE)						Western aspect (S, SW, W, and NW)							
	Metal	Category	B1	B2	B3	B4	B5	B7	Area (km ²)	B1	B2	B3	B4	B5	B7	Area (km ²)
0–15°	Cu	Low	0.008	0.025	0.016	0.276	0.113	0.042	36.14	0.008	0.024	0.015	0.270	0.111	0.041	85.93
		Medium	0.008	0.025	0.015	0.276	0.114	0.042	114.31	0.008	0.024	0.015	0.276	0.113	0.042	122.96
		High	0.010	0.026	0.016	0.283	0.117	0.044	49.00	0.009	0.026	0.016	0.283	0.116	0.043	67.57
	Pb	Medium	0.008	0.025	0.016	0.277	0.114	0.043	110.41	0.008	0.024	0.015	0.274	0.113	0.042	175.03
		High	0.009	0.025	0.016	0.279	0.115	0.043	80.93	0.009	0.025	0.016	0.281	0.115	0.043	85.33
	Zn	Low	0.009	0.025	0.016	0.280	0.116	0.044	22.91	0.008	0.025	0.016	0.277	0.114	0.043	46.41
		Medium	0.008	0.025	0.015	0.276	0.114	0.042	142.32	0.008	0.024	0.015	0.273	0.112	0.042	194.03
		High	0.010	0.026	0.016	0.286	0.116	0.043	34.22	0.009	0.026	0.016	0.290	0.116	0.044	36.02
	>15°	Cu	Low	0.008	0.025	0.016	0.280	0.114	0.042	24.97	0.007	0.024	0.015	0.275	0.111	0.041
Medium			0.008	0.024	0.015	0.279	0.114	0.042	70.46	0.007	0.023	0.015	0.273	0.110	0.041	106.39
High			0.009	0.025	0.016	0.284	0.116	0.043	37.57	0.008	0.024	0.015	0.280	0.114	0.042	50.61
Pb		Medium	0.008	0.025	0.016	0.281	0.115	0.043	77.56	0.007	0.023	0.015	0.275	0.111	0.041	156.35
		High	0.009	0.025	0.015	0.280	0.114	0.042	50.36	0.008	0.024	0.015	0.277	0.112	0.042	60.55
Zn		Low	0.008	0.024	0.016	0.277	0.114	0.042	14.77	0.007	0.024	0.015	0.276	0.112	0.041	40.26
		Medium	0.008	0.025	0.015	0.279	0.114	0.042	94.46	0.007	0.023	0.015	0.273	0.111	0.041	162.27
		High	0.010	0.026	0.016	0.289	0.115	0.043	23.78	0.009	0.025	0.015	0.290	0.114	0.042	24.73

Finally the NDVI and VIGS averages for low, medium, and high metal contents were compared for the selected area using the conditions in Table 4.2. As a result, the superiority of VIGS is confirmed from Fig. 4.11, because the VIGS of every metal increased appropriately with metal content in all four classifications. Both the NDVI and VIGS values are the smallest

for the low metal contents, which may be due to a geological control because the low categories are mostly overlain by the sedimentary rocks. When focusing only on the medium and high metal contents, the NDVI values decrease all classifications of Cu, two of Pb, and two of Zn. This part of the NDVI results and the increase of VIGS with metal content agree with the result of laboratory experiments. Additionally, VI variation with metal content is more conspicuous for VIGS than NDVI, for all metals. It is noteworthy that VIGS can discriminate high and medium contents more clearly than the NDVI. However, the present analysis was based on only the best quality Landsat image for the study area. More images with different seasons will be necessary to generalize the superiority of VIGS.

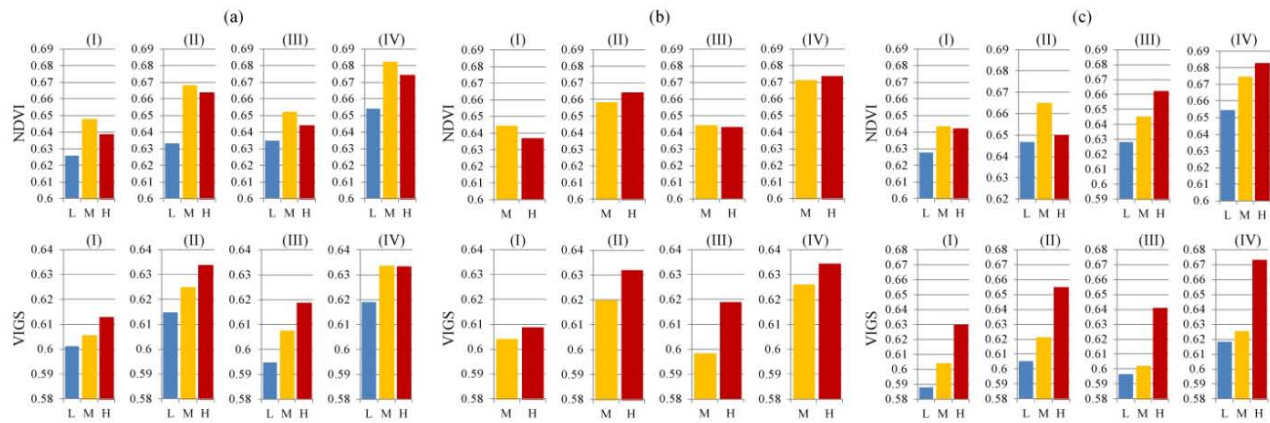


Fig. 4.11. Comparison of average NDVI and VIGS for each metal content category, low (L), medium (M) and high (H) in the selected area covered by the primary forest, higher than 300 m a.s.l. and without exploitable groundwater. Metals are (a) Cu, (b) Pb, and (c) Zn. The area is further separated into four domains by slope gradients (1) 0–15° and (2) >15°, and aspect (3) dip toward east side (N, NE, E, and SE) and (4) west side (S, SW, W, and NE). Combinations of gradient and aspect in the four domains are (I) 1 and 3, (II) 1 and 4, (III) 2 and 3, and (IV) 2 and 4, respectively.

4.4. Discussion

To improve the VIGS applicability to mineral exploration by a method other than pixel-to-pixel correlation, the following method is proposed. Because the VIGS data were transformed into a Gaussian distribution, those exceeding the mean plus one standard deviation (1.0σ) were regarded as anomalous, related to metal enrichment based on the results above. Thus, 490,990 pixels (17.7% of the total) satisfying this condition were extracted, which were scattered across the image. To characterize the anomaly distribution by converting the scatter to a simple pattern, a point density map of anomalous pixels was constructed. After gridding the study area with 1×1 km grid size, this density was defined by the number of anomalous pixels within each grid cell.

Finally, the C-A model was applied to the density of VIGS anomalous values, to clearly distinguish large-value zones (Fig. 4.12a) in which the anomaly densities were categorized as I: low, II: medium, and III: high. High-density areas are mainly covered by the primary forest (Fig. 6). Furthermore, the spatial distribution of Cu contents classified as low, medium, and high was correlated with the density of VIGS anomalies (Fig. 4.12a). The reason for selecting Cu is that it is the major metal in the study area for characterizing mineralization, with twice the average for the Sumatra region. In contrast, the Pb and Zn averages are nearly identical to that of the region (British Geological Survey, 2007). Obviously, the high Cu-content data are in the high-density category in the northern half of the study area (marked by “A” in Fig. 4.12a). This relationship did not appear in the Ngaol region, where high Cu-content data are within a low-density category. This may be because that region is covered by the secondary forest and paddy fields (see Fig. 3.4) which generally have small VIGS values. Inconsistency in the other regions was mainly caused by the submontane forest, which also tends to have small VIGS values.

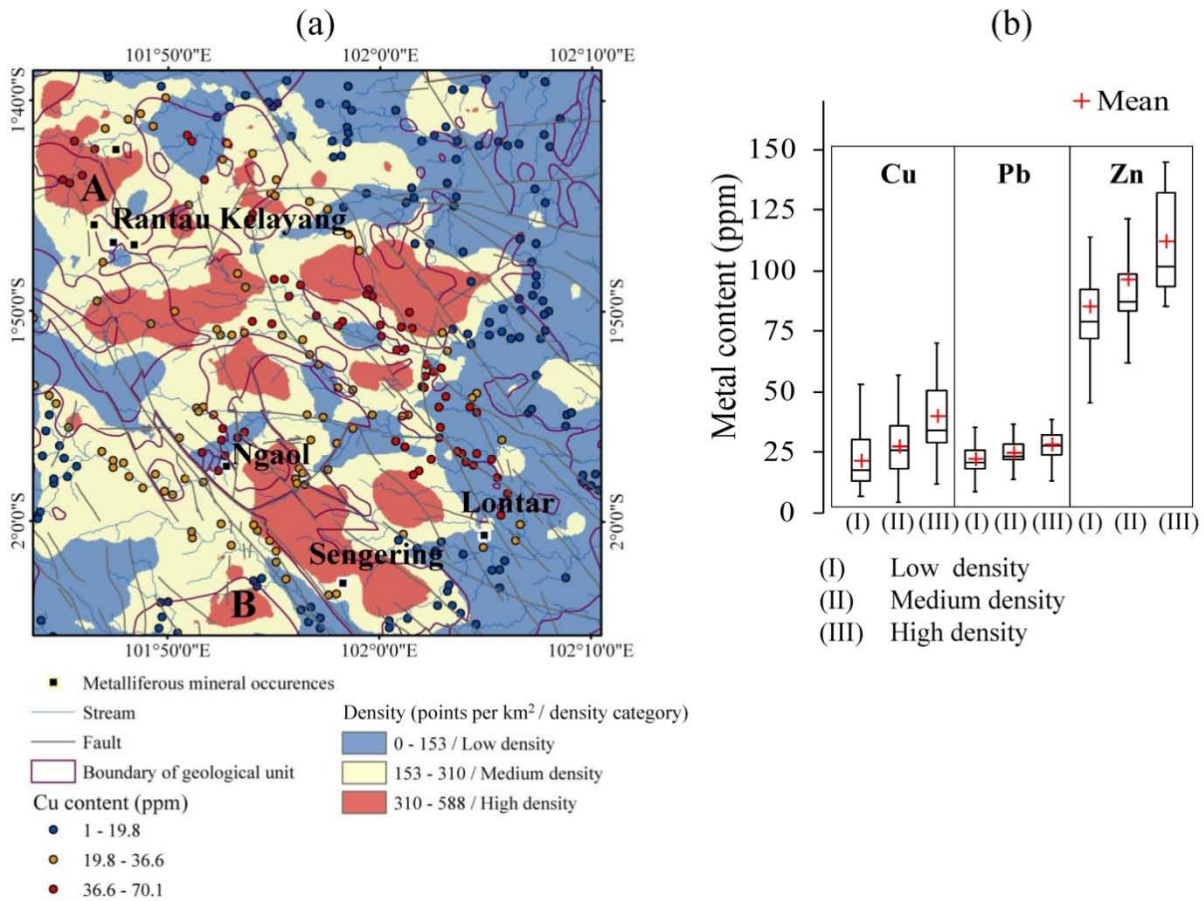


Fig. 4.12. Spatial characterization of density of VIGS anomaly values (greater than mean + standard deviation) with metal content. (a) Distribution of (I) low, (II) medium, and (III) high density categories of VIGS anomaly values from the C-A model, overlaid by Cu content data classified as low (1–19.8 ppm), medium (19.8–36.6 ppm), and high (36.6–70.1 ppm). The content classifications follow the C-A model in Fig. 4.5. (b) Relationships of Cu, Pb, and Zn contents with VIGS categories, shown by box plots.

VIGS validity can be confirmed from another aspect of geologic correspondence. High densities are found in the Tertiary intrusive rocks (see Fig. 3.2 in Chapter 3) as shown by the “B” in Fig. 4.12a, whereas there are low densities in the Jurassic–Cretaceous metasedimentary rocks. This is a reasonable tendency, because metal contents are generally higher in intrusive or

volcanic units than sedimentary and metasedimentary units. The C-A model was also used to correlate the values with the metal content data in detail. This correlation focused on the area covered by the primary forest, where 131 content data were sampled, because the effect of metal soil contamination has accumulated in this natural land cover as mentioned above. As a result, average metal contents increase with category, for all three metals (Fig. 4.12b); large VIGS values are associated with high metal contents, and small values with low contents. This trend confirms the satisfactory VIGS correspondence to metal soil contamination and the applicability of VIGS to mineral exploration in areas with thick vegetation, using the C–A model and area segmentation with control factors of VI.

4.5. Conclusions

The effectiveness of VIGS as developed in Chapter 2 was applied to Landsat ETM+ imagery in tropical forest, Jambi, Sumatra, Indonesia where mineral deposits of copper porphyry are existed and mineralized zones are distributed in places. A set of soil geochemical data is used as a ground-truth to evaluate positional concordance of the VI anomalies derived from the imagery with the soils of high metal concentration. The main results can be summarized as follows.

- Vegetation stresses from three metals (Cu, Pb, and Zn) in the soils frequently appeared in the reflectance spectra, in both the VNIR and SWIR regions. By correlating metal content categories in the top layer, which were prepared by kriging interpolation and the C-A model and using NDVI and VIGS values, VIGS superiority was confirmed. This was because VI change with metal content was more discriminable by VIGS than NDVI, for all metals.

- To simplify spatially scattered VIGS values, a method for characterizing VIGS anomaly values was proposed. This method used the C-A model of the density of points whose VIGS values were greater than the mean plus standard deviation. High-density zones were generally correspondent with those of high metal content, which verifies VIGS applicability to mineral exploration in areas thickly covered by vegetation.
- A limitation of this study is that the analysis was based on only the best quality Landsat image for the study area. More images with different seasons and a consideration of vegetation structures such as canopy heights and shapes will be necessary to generalize the superiority of VIGS in future work.

References

- British Geological Survey. (2007). Indonesia regional geochemical survey (CD-ROM): Sumatra. Version 3.0. Keyworth, Nottingham, UK.
- Bruce, B., & Hornsby, J. K. (1987). A Canadian perspective on the application of satellite remote sensing to regional geobotany. *Geocarto International*, 2(3), 53–59. <http://doi.org/10.1080/10106048709354108>
- Cheng, Q., Agterberg, F. P., & Ballantyne, S. B. (1994). The separation of geochemical anomalies from background by fractal methods. *Journal of Geochemical Exploration*, 51(2), 109–130. [http://doi.org/10.1016/0375-6742\(94\)90013-2](http://doi.org/10.1016/0375-6742(94)90013-2)
- Conradsen, K., Nielsen, A. A., & Windfeld, K. (1992). Analysis of geochemical data sampled on a regional scale. In A. T. Walden & P. Guttorp (Eds.), *Statistics in the environmental and earth sciences* (pp. 283–300). London: Edward Arnold.
- Crow, M. J., Johnson, C. C., McCourt, W. J., & Harmanto. (1993). The simplified geology and known metalliferous mineral occurrences, Painan quadrangle Southern Sumatra. *Special Publication of the Directorate of Mineral Resources, No. 52-B*. Bandung.
- Koide, K., & Koike, K. (2012). Applying vegetation indices to detect high water table zones in humid warm-temperate regions using satellite remote sensing. *International Journal of*

- Applied Earth Observation and Geoinformation*, 19, 88–103. <http://doi.org/10.1016/j.jag.2012.03.017>
- Laumonier, Y. (1997). *The vegetation and physiography of Sumatra*. (M. J. A. Werger, Ed.). Dordrecht: Springer Netherlands. <http://doi.org/10.1007/978-94-009-0031-8>
- Lyon, J. G., Yuan, D., Lunetta, R. S., & Elvidge, C. D. (1998). A change detection experiment using vegetation indices. *Photogrammetric Engineering & Remote Sensing*, 64(2), 143–150. <http://doi.org/citeulike-article-id:7262520>
- Poschenrieder, C., & Barceló, J. (1999). Water relations in heavy metal stressed plants. In *Heavy Metal Stress in Plants SE - 10* (pp. 207–229). Springer Berlin Heidelberg. http://doi.org/10.1007/978-3-662-07745-0_10

Chapter 5

Applying VIGS to multi-temporal satellite image for identification of kuroko-type ore deposits

5.1. Introduction

VIGS has been proposed by integrating the reflectances in the visible to SWIR range and has been proven to be more sensitive to vegetation stress (see Chapter 2). The effectiveness of the VIGS has been demonstrated in the tropics via correlations with geochemical data using one Landsat ETM+ scene image after atmospheric correction, indicating that high-content metal zones, which are closely related to ore deposits, are indicated by high VIGS values (see Chapter 4). However, this analysis is based on a single observation, and because images change over space and time, the accuracy and sensitivity of this approach require further clarification.

This chapter aims to improve and demonstrate the benefits of using VI by integrating it with multi-temporal data to highlight anomalous vegetation characteristics that may be related to ore deposit distributions. This chapter was built on the assumption that when temporal changes in vegetation activity are large, a temporal analysis of vegetation indices using images with different seasons must be indispensable. Therefore the target area is humid warm-temperature regions in which seasonal change in vegetation is clear and this region extend widely in the Earth. Another consideration is VIGS will applied for different type of deposits, in this case is volcanogenic massive sulphide (VMS) type that is also common ore type in volcanic zones.

5.2. Study area and geologic setting

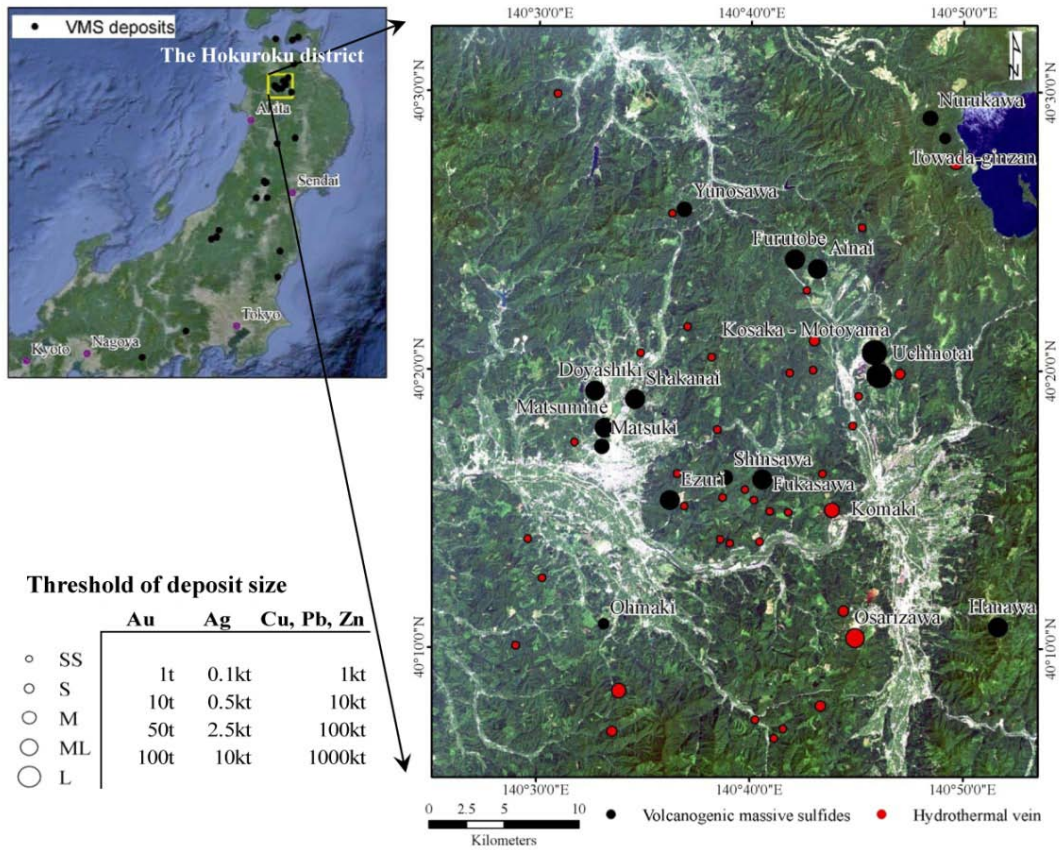


Fig. 5.1. Map of the known ore deposit locations in the Hokuroku district, northern Japan overlaid with a true-color composite of three bands, i.e., red (B3), green (B2), and blue (B1), in a Landsat ETM+ image acquired on 25 July 2002. SS, S, M, ML, and L indicate the relative size of the deposits from small to large.

To accomplish the objective of this study, an area in the Hokuroku district (40 km × 50 km in size), Akita Prefecture, Japan, is selected (Fig. 5.1). This area is the most suitable site for detecting vegetation anomalies because many ore deposits can be found there. The Hokuroku district is globally recognized for its rich ore deposits (based on grade and tonnage); the district

was one of the most productive mining regions in Japan for centuries. The estimated total reserves in the Hokuroku district are $\sim 14 \times 10^7$ tons, with the following metal contents: 0.8–3.7% Cu, 0.1–5% Pb, 0.8–16% Zn, and 1–8 ppm Au (Ishikawa, 1991; Nakajima, 1989b). There are many important ore deposits in this region, which are primarily kuroko-type volcanogenic massive sulfides (VMS) and fissure-filling hydrothermal veins that have been thoroughly explored and studied (Sato et al., 1974; Sato, 1974; Yamada & Yoshida, 2011).

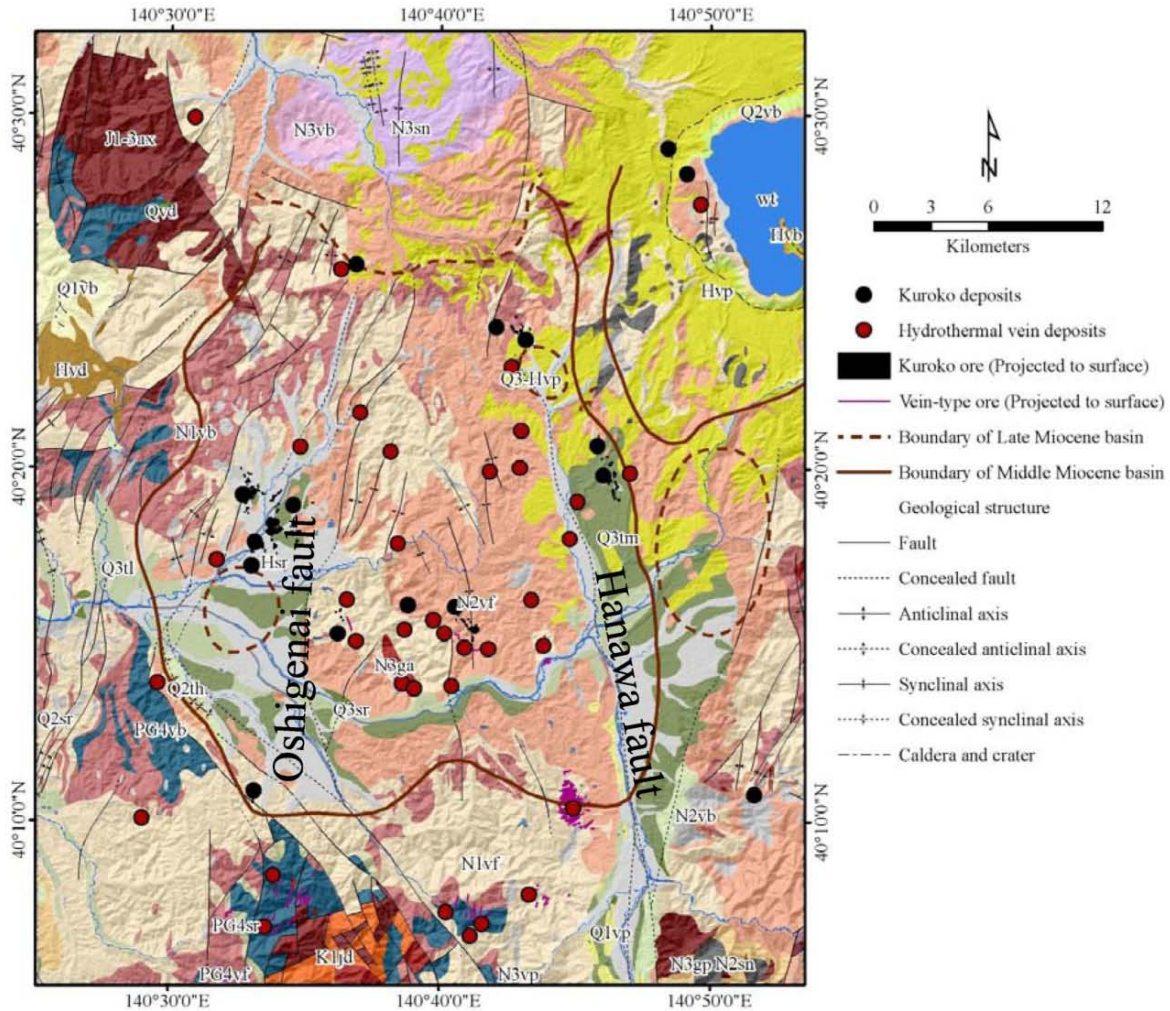
The Hokuroku district is chiefly composed of Neogene altered rocks and pre-Neogene basement rocks with felsic volcanic rocks and tuffs as the predominant rock types (Fig. 5.2). The mountainous eastern and northwestern margins of the district are overlain by Quaternary volcanic rocks: Towada Lake and its surrounding ejecta in the northeastern edge were also formed by such recent volcanic activity. There are several small basins in the district such as the Hanawa and Odate basins, which are covered by terrace and alluvial deposits. The Hokuroku basin in the central district is the largest, main basin, which is thought to be a part of volcanogenic collapses or submarine calderas formed by the undersea volcanic activity in Miocene Green-Tuff movement (Kouda & Koide, 1978; Ohmoto, 1978). Based on reconstruction of the pre-Neogene basements as the bottom structure, the thickness of the Hokuroku basin is 2,600 m at the most (Nakajima, 1993).

The Hokuroku district is dominated by kuroko (“black ore” in Japanese) deposits, a type of volcanogenic massive sulfide deposits that had been generated by the Miocene felsic to intermediate volcanism (Sato, 1974). Main mineral constituents of kuroko are chalcopyrite, pyrite, sphalerite, galena, barite, and quartz. In addition, gypsum and anhydrite are commonly remarkable and form separate bodies beside sulfide-barite bodies. Epithermal vein-type deposits, primary sources of gold and silver, are also plentiful in dacitic or andesitic volcanic rocks and

tuffs (Kouda & Koide, 1978). Table 5.1 shows major ore deposits in the Hokuroku district and their specification.

The generations of kuroko and vein-type deposits have been studied from several aspects of geological and structural controls, mineralization process, and physical chemistry ore solutions (Glasby et al., 2004; Ohmoto, 1996; Sato, 1977; Scott, 1978) as the following examples. Subsidence of the Hokuroku basin, which was associated with the dacite volcanism, caused significantly metal enrichments. Major kuroko deposits are embedded in the middle Miocene sedimentary sub-basins along the border of the subsiding basin (Sato et al., 1974). Meanwhile, distribution of the vein-type deposits is scattered and most are located at high elevation areas in the southern part (Nakajima, 1989a).

The ring structures with the 20–30 km were identified in the Hokuroku district because the kuroko deposits seem to be circularly distributed (Sato et al., 1974; Sato, 1974). The understanding of the Hokuroku basin has been extended to include large-scale ring structures with diameters of approximately 20–30 km. The small-scale cauldrons (~8–10 km in diameter), which may be resurgent cauldrons, are key structure to concentrate the kuroko deposits in the middle Hokuroku basin instead of the margin of the basin (Kouda & Koide, 1978). Post-kuroko ore veins are also related to them. However, there are kuroko deposits unrelated to the ring structures because of the complicated system of volcanism and the post-depositional tectonic activities. There are two major north-south striking, vertical faults, the Ohshigenai and Hanawa faults. Although most of Neogene intrusive rocks were controlled by the faults, the deposits locations have little relationship with the structures (Sato et al., 1974).



Code	Lithology	Code	Lithology
Hsr	Late Pleistocene to Holocene marine and non-marine sediments	N3vp	Late Miocene to Pliocene non-alkaline pyroclastic flow volcanic rocks
Hvd	Holocene volcanic debris	N3vb	Late Miocene to Pliocene non-alkaline mafic volcanic rocks
Hvp	Holocene non-alkaline pyroclastic flow volcanic rocks	N3gp	Late Miocene to Pliocene felsic plutonic rocks
Hvb	Holocene non-alkaline mafic volcanic rocks	N3ga	Late Miocene to Pliocene mafic plutonic rocks
Q3tl	Late Pleistocene lower terrace	N2sn	Middle to Late Miocene non-marine sediments
Q3tm	Late Pleistocene middle terrace	N2vf	Middle to Late Miocene non-alkaline felsic volcanic rocks
Q3sr	Late Pleistocene marine and non-marine sediments	N2vb	Middle to Late Miocene non-alkaline mafic volcanic rocks
Q3-Hv	Late Pleistocene to Holocene non-alkaline pyroclastic flow volcanic rocks	N1vf	Early Miocene to Middle Miocene non-alkaline felsic volcanic rocks
Q3-Hv	Late Pleistocene to Holocene non-alkaline mafic volcanic rocks	N1vb	Early Miocene to Middle Miocene non-alkaline mafic volcanic rocks
Q2th	Middle Pleistocene higher terrace	PG4sr	Late Oligocene to Early Miocene marine and non-marine sediments
Q2sr	Middle Pleistocene marine and non-marine sediments	PG4vf	Late Oligocene to Early Miocene non-alkaline felsic volcanic rocks
Q1vp	Early Pleistocene non-alkaline pyroclastic flow volcanic rocks	PG4vt	Late Oligocene to Early Miocene non-alkaline mafic volcanic rocks
Q1vb	Early Pleistocene non-alkaline mafic volcanic rocks	K1jd	Early Cretaceous granodiorite (Abukuma Granite)
N3sn	Late Miocene to Pliocene non-marine sediments	J1-3ax	Melange matrix of Early to Late Jurassic accretionary complex
N3vf	Late Miocene to Pliocene non-alkaline felsic volcanic rocks	wt	water

Fig. 5.2. Surface geological and Miocene sedimentary basin map of the study area modified after (Ohmoto, 1978; Wakitawa et al., 2009), which shows projected kuroko and vein-type ore deposits at the surface.

Table 5.1. Major ore deposits in the Hokuroku district and their specification. These deposits are plotted in Figs. 5.1, 5.2, 5.10–5.13.

Deposit name	Commodity (Cu, Pb, and Zn in %; Au and Ag in ppm)	Type	Longitude (East °)	Latitude (North °)	Size*
Kosaka - Motoyama	Cu (1.1–2.6), Pb (0.6–1.9), Zn (2.7–5.8), Au, Ag	kuroko	140.76	40.34	L
Uchinotai	Cu, Pb	kuroko	140.77	40.33	L
Ezuri	Cu (1.3–1.7), Pb (3.0–3.2), Zn (9.0–9.3), Au, Ag	kuroko	140.60	40.26	ML
Ainai	Cu (0.6–1.8), Pb (0.5–2.2), Zn (1.7–7.2), Au, Ag	kuroko	140.72	40.39	ML
Furutobe	Cu (1.9–2.3), Pb (0.3–1.2), Zn (1.2–3.3), Au, Ag	kuroko	140.70	40.40	ML
Hanawa	Cu (0.8–2.1), Pb (0.5–1.2), Zn (2.7–3.9), Au, Ag	kuroko	140.86	40.18	ML
Matsumine	Cu (2.4–2.8), Pb (0.2–0.9), Zn (1.1–3.4), Au, Ag	kuroko	140.55	40.30	ML
Shakanai	Cu (1.7–2.6), Zn (2.5–10.2), Pb (0.5–3.3), Au, Ag	kuroko	140.58	40.32	ML
Doyashiki	Cu (1.1–1.2), Pb (0.1–0.5), Zn (0.8–2.1), Au, Ag	kuroko	140.54	40.32	ML
Fukasawa	Cu (1.0–2.9), Pb (1.0–2.7), Zn (2.7–9.5), Au, Ag	kuroko	140.68	40.27	ML
Matsuki	Cu (3.7), Pb (0.8), Zn (2.0), Au, Ag	kuroko	140.55	40.29	M
Nurukawa	Cu (0.8–1.0), Pb (2.0–5.0), Zn (3.0–10.0), Au, Ag	kuroko	140.81	40.48	M
Towada-ginzan	Cu (1.5), Pb (15–20), Zn (10–15), Au (6.5), Ag (516)	kuroko	140.82	40.47	M
Shinsawa	Cu, Pb, Zn	kuroko	140.65	40.27	M
Yunosawa	Pb, Zn, Ag	kuroko	140.61	40.43	M
Komaki	Cu (2.5–3.0), Au (0.3–0.7), Ag (7–10)	kuroko	140.73	40.25	M
Ohmaki	Cu (1.5), Zn (4.9), Pb, Ag	kuroko	140.55	40.18	S
Osarizawa	Cu, Zn, Au, Ag, Pb	vein	140.75	40.17	ML
Tatemata	Cu, Zn, Pb, Ag	vein	140.56	40.14	ML
Namariyama	Zn, Cu	vein	140.83	40.46	M
Horinai	Cu (0.8), Pb (0.3–3), Zn (2–7)	vein	140.72	40.35	S
Okuzu	Cu (1.7–3.8), Pb (0–1.1), Zn (0–6.8), Au (1.8–8.0), Ag (7–23)	vein	140.72	40.13	S
Tokito	Cu (1.5–3.0), Pb (1.7–5.0), Zn (3–5)	vein	140.78	40.33	S
Akarimata	Cu, Ag	vein	140.56	40.12	S

Dofukai	Cu (2.8–4.0)	vein	140.74	40.19	S
Nagaki	Cu (2–8), Pb (5–27), Zn (10–30), Au (1–8), Ag (300–500)	vein	140.72	40.33	SS
Ishikura	Cu (3–4), Pb (2–6), Zn (7–8)	vein	140.70	40.33	SS
Kanahata	Cu (1.5–3.5)	vein	140.75	40.32	SS
Daichi	Cu (2–10)	vein	140.75	40.30	SS
Wakakidachi	Au, Ag	vein	140.71	40.38	SS
Zogakura	Cu (5.0–6.2)	vein	140.66	40.26	SS
Takarakura	Cu (2–4)	vein	140.67	40.25	SS
Iwagami	Cu (10, Zn (18)	vein	140.61	40.27	SS
Akitsu	Cu (4–6), Zn (8–40), Ag (150)	vein	140.60	40.43	SS
Edate	Cu, Pb, Zn	vein	140.61	40.25	SS
Yamadate	Cu, Pb, Zn	vein	140.64	40.26	SS
Magada	Au (2–400)	vein	140.64	40.23	SS
Karuizawa	Cu (1–3), Zn (4–20)	vein	140.65	40.23	SS
Saruma	Cu (5–6)	vein	140.68	40.25	SS
Osawa	Au, Ag	vein	140.69	40.12	SS
Otani	Au, Ag	vein	140.68	40.11	SS
Kamata	Au, Ag	vein	140.67	40.12	SS
Yunotai	Cu, Pb	vein	140.48	40.17	SS
Izuti	Cu (2.5), Pb (2), Zn (7)	vein	140.51	40.50	SS
Ohkura	Cu, Au	vein	140.49	40.23	SS
Usagijiri		vein	140.75	40.42	SS
Maeda		vein	140.50	40.21	SS
Shirasawa		vein	140.62	40.36	SS
Ohshigenai		vein	140.64	40.34	SS
Nakahadachi		vein	140.58	40.34	SS
Koyukizawa		vein	140.64	40.30	SS
Numadate		vein	140.53	40.29	SS
Kanayamazama		vein	140.72	40.27	SS
Asahizawa		vein	140.69	40.25	SS
Saruma-Tozawa		vein	140.67	40.23	SS

Deposit size	L	ML	M	S	SS
Au	>100t	50t–100t	10t–50t	1t–10t	<1t
Ag	>10kt	2.5kt–10kt	0.5kt–2.5kt	0.1kt–0.5kt	<0.1kt
Cu, Pb, Zn	>1000kt	100kt–1000kt	10kt–100kt	1kt–10kt	<1kt

t = ton and kt = 10³ metric ton

5.3. Methods

5.3.1. Satellite images

Five Landsat ETM+ images acquired at different times between 40° 10' and 40° 26' latitude and 140° 19' to 140° 28' longitude in the UTM-WGS84 system are used for the image analysis (Table 5.2). I assume that no significant loss of land cover type occurred in this area during the image acquisition period (2000 to 2002). Areas of small cloud cover are excluded in the subsequent analysis. The pre-processing stages include atmospheric correction using the Fast Line-of-sight Atmospheric Analysis of Spectral Hypercubes (FLAASH) module, which is included in the ENVI 5.2 software package, and a topographic correction that follows the C-correction method (Civco, 1989). The ASTER Global Digital Elevation Model (GDEM), which highlights rough topography, is used for the topographic correction. The ASTER GDEM is a product developed by the Ministry of Economy, Trade, and Industry (METI) of Japan and the United States National Aeronautics and Space Administration (NASA).

Table 5.2. Detailed description of the Landsat 7 ETM+ images used in this study.

Image No.	Acquisition	Sun azimuth (°)	Sun elevation (°)	Cloud cover	Surface temperature* (°C)	Season
1.	7/25/2002	127.24	60.61	0.08	26.5	Summer
2.	8/20/2000	137.52	55.48	0.44	25.6	Summer
3.	9/5/2000	143.74	51.10	0.28	20.1	Autumn
4.	9/21/2000	149.47	46.12	0.04	17.5	Autumn
5.	10/13/2002	154.70	38.71	0.04	12.5	Autumn

* Surface temperature data based on daily averages recorded by the Japan Meteorological Agency

(<http://www.data.jma.go.jp>).

5.3.2. Land-cover information and geological datasets

The land-cover data are based on the Land-Use and Land-Cover (LULC) ver.14.02 map edited by the Japanese Aerospace Exploration Agency (JAXA) Earth Observation Research Center (EORC) (http://www.eorc.jaxa.jp/ALOS/lulc/lulc_jindex.htm). This map is generated using Advanced Visible and Near Infrared Radiometer type 2 (AVNIR-2) image data on the Advanced Land Observing Satellite (ALOS) with a spatial resolution of 50 m. As shown in Fig. 5.3, thick vegetation (deciduous and evergreen type forest) is dominant (Fig. 5.4), with small areas comprised of water, urban environments, paddy fields, crop fields, and grasslands.

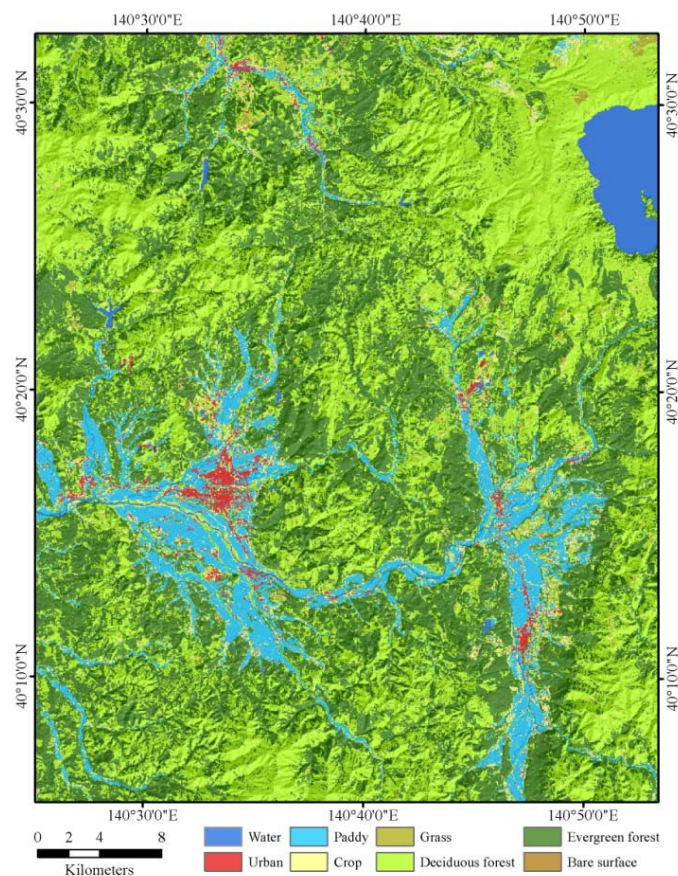


Fig. 5.3. Map of the land cover generated by the Japan Aerospace Exploration Agency (JAXA) that is superimposed with the ASTER GDEM shaded relief.



Fig. 5.4. Field photographs showing typical forest cover and outcrops. Sceneries of (a) evergreen forest in which the predominant vegetation community is conifer and (b) a mixture of the evergreen and deciduous forests in the Komaki area. (c) An alteration outcrop of the East Kannondo in the northern Doyashiki deposit (See Fig. 5.1). These photos were taken in a field study on 26 November 2012.

Geological units were compiled from the seamless digital geological map of 1:200,000 by the Geological Survey of Japan (Wakitawa et al., 2009). Several references were sourced for the location of the ore deposits, the geological structures, and the interpretation of the basin, are obtained from various published sources (Kouda & Koide, 1978; Nakajima, 1989b; Sato et al., 1974). In addition, a gravity data set by the Geological Survey of Japan (ed.) (2013) used as the basis for the geophysical data.

5.3.3. Calculation of the VIs

Reflectance at each pixel was derived from the pre-processed Landsat images and used to calculate two images for VIs, VIGS and NDVI (see Chapter 2 section 2.2.2). Here, I demonstrated that VIGS was more sensitive to metal-induced vegetation stress than NDVI using the Landsat ETM+ images that included the Hokuroku district. To emphasize a small reflectance change caused by the stress, multi-temporal satellite images with different seasons and a ratio of the mean (m) to the standard deviation (σ) calculated on a per-pixel basis from the VIGS dataset were used. Selection of this ratio based on the previous studies that showed that the VIGS values tended to be large at metal contamination zones common to the Landsat images in the growing season (see Chapter 2 and Chapter 4), which suggested that VIGS could partly remove the phenology effect. Therefore, seasonal change in the reflectance of the stressed plants is expected to be small and yield a large ratio.

5.3.4. Image enhancement methods

The following three methods were used to enhance the VIGS image and highlight the vegetation anomaly zones.

Forced invariance method. This algorithm, originally proposed to suppress the vegetation from a remotely-sensed image (Crippen & Blom, 2001), was used to even the image contrast by reducing the elevation effect by the following two steps. The first step is to produce a curve that approximates the relationship between the elevation and ratio m/σ . This curve was defined to connect the averages of m/σ in each elevation bin. The spikes (outliers) in the curve originated from the water and cloud covers were deleted using a sequence of median and mean

filters, respectively (Crippen & Blom, 2001). The next step is to flatten the curve to a defined, desirable ratio by:

$$\text{Revised ratio} = \text{original ratio} \times \text{defined value} / \text{ratio based on the curve} \quad (5.1)$$

The total average of the original ratio was used for the defined value, which was 46 in the 8-bit integer scale (0–255) in the present case. The revised ratios over 255 were changed to 255 to avoid overcorrection. Finally, the elevation effect was confirmed to be corrected because the averages of revised ratios were constant over all the elevation bins.

Geostatistical smoothing approach. This approach was employed to delete the local abrupt changes of the ratios (noise). The spherical model was the best fit to the experimental $\gamma(h)$ and used for interpolating the centers of unit cells by ordinary kriging (OK) at the 30 m interval (equal to the Landsat ETM+ image resolution) to generate a smoothed ratio image.

Residual analysis. The purpose of this analysis was to remove regional trends and emphasize local variation related to anomalies of the VI values and gravity data. A regional trend component was first extracted by applying a moving average filter to the smoothed raster data by the above kriging interpolation (the ratio image and residual gravity data). The radius for the data averaging was set equal to be the range (the maximum distance of presence of any correlation between data pairs) of the $\gamma(h)$ model. A residual anomaly component was determined by subtracting the trend component from the smoothed raster data. Fig. 5.5 shows the overall procedure used in this chapter.

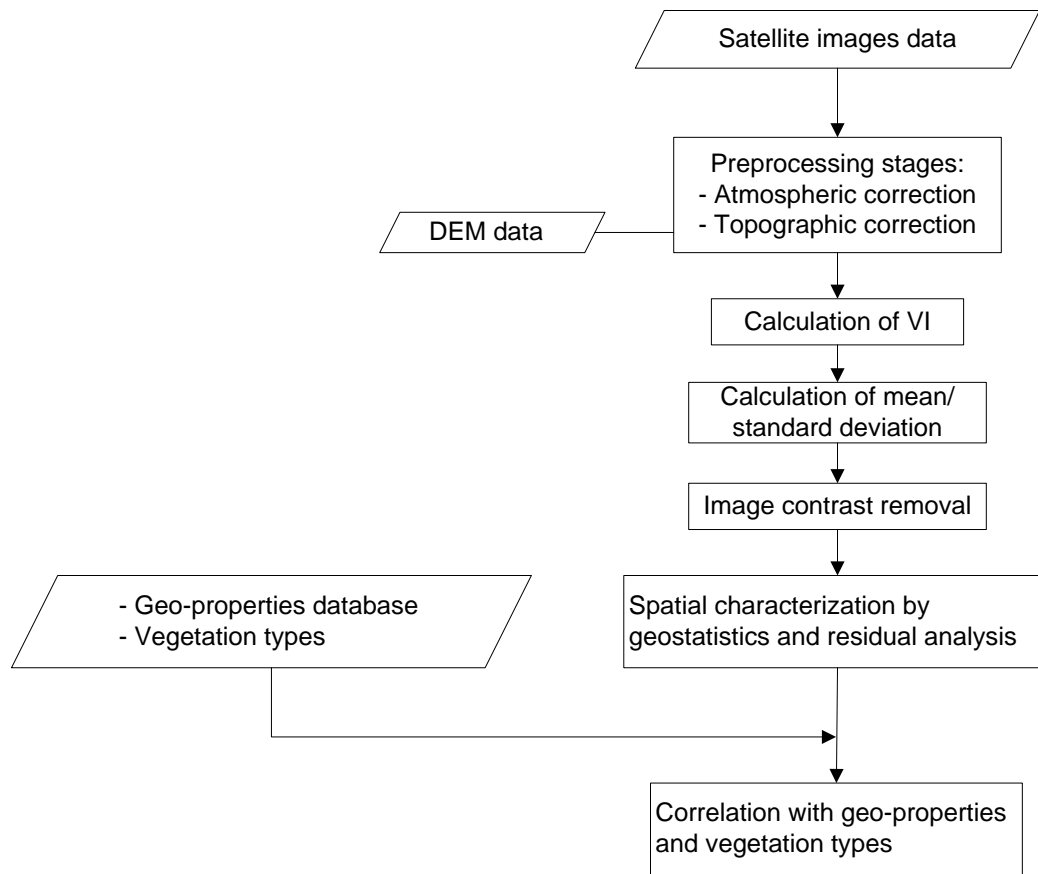


Fig. 5.5. Workflow of image and data analyses.

5.4. Results and discussion

5.4.1. Temporal change in vegetation index

More than 84.21% of the study area is covered by dense forest, which consists of 42.19% deciduous forest and 42.02% evergreen forest between elevations of 10 m and 1,100 m a.s.l. (Fig. 5.6a; see Fig. 5.3 for their distribution). Different forest types have difference reflectance values; this variability can be affected by the elevation (Fig. 5.6b). The variabilities in the means and standard deviations at difference elevations and over different spectral ranges can be explained as follows. The variability in the reflectances at low elevations (e.g., < 200 m a.s.l.) is most likely affected by anthropogenic factors because this region is approximately 37.56% covered by urban

environments, paddy fields, and crops. The mean reflectances of the visible green and blue bands (B2-B3) increase slightly at < 600 m a.s.l., especially for the deciduous forest, which is thought to be due to more intense chlorophyll degradation during seasonal changes. Note that the mean reflectances also increase slightly as a function of elevation in the NIR to SWIR range (B4 - B7), which is indicative of water stress and may be related to the water table conditions. Moreover, the temporal changes also impact water stress in vegetation, which is indicated by the large variability in the SWIR range (B5 and B7) for both deciduous and evergreen forests.

Landsat-based five NDVI and VIGS images show clear seasonal changes in vegetation activity (Fig. 5.7a). Consistent with a previous result that spring and autumn are the best seasons to detect the plant physiological response to environment (Bruce & Hornsby, 1987), both VI images are contrasted in the autumn images. However, the differences in the VI values between deciduous and evergreen forests are more obvious by VIGS than NDVI, which demonstrates high sensitivity of VIGS to the changes in reflectance spectra of vegetation. This sensitivity is proved by the wider range of the VI histogram of VIGS than NDVI (Fig. 5.7b).

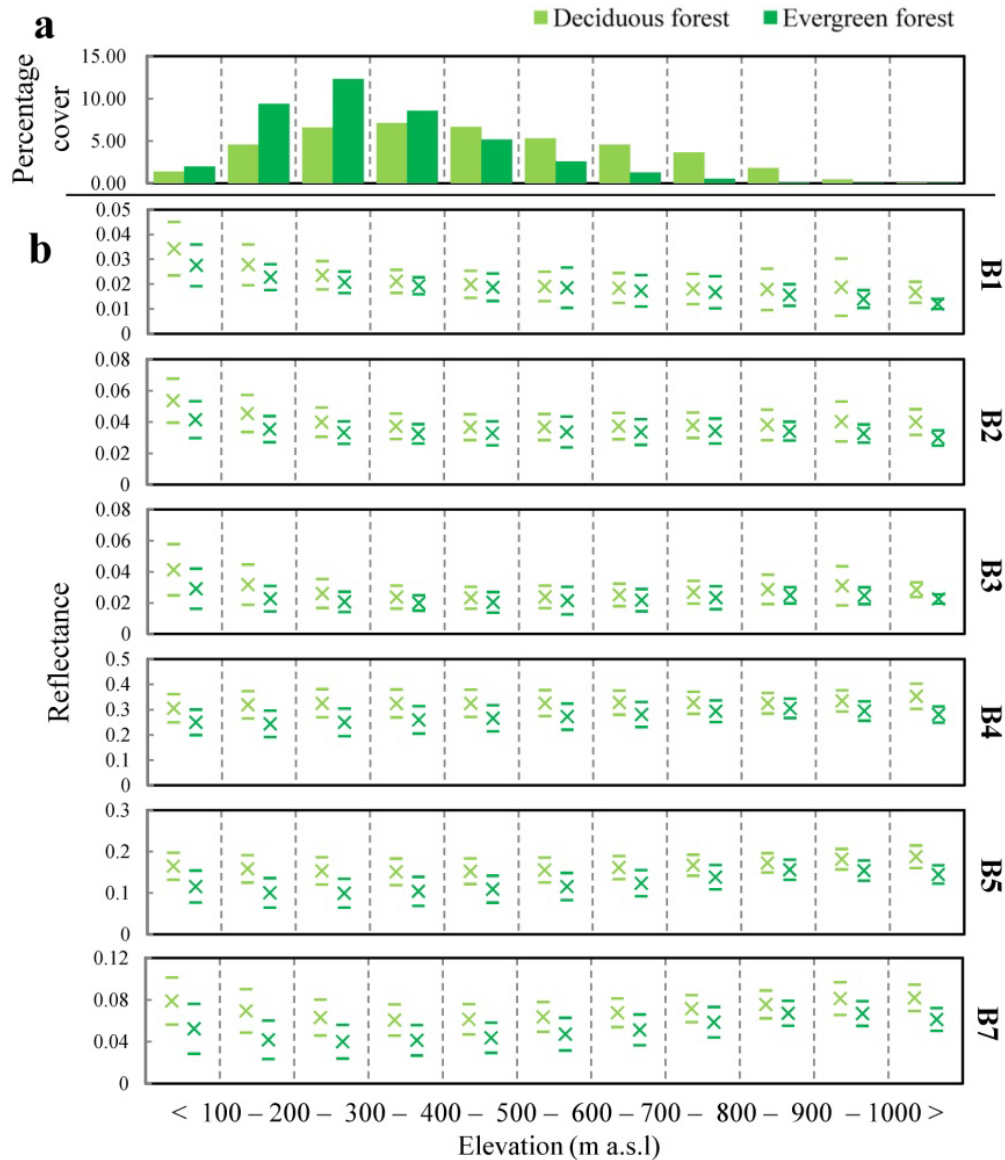


Fig. 5.6. Forest type spatial distribution according to the elevation and multi-temporal data. (a) Changes in forest (deciduous and evergreen types) cover rates and (b) reflectance variability by mean (×) and standard deviation (bars above and below the mean) of VNIR and SWIR bands (B1–B5 and B7) of five Landsat ETM+ images for each 100 m elevation range

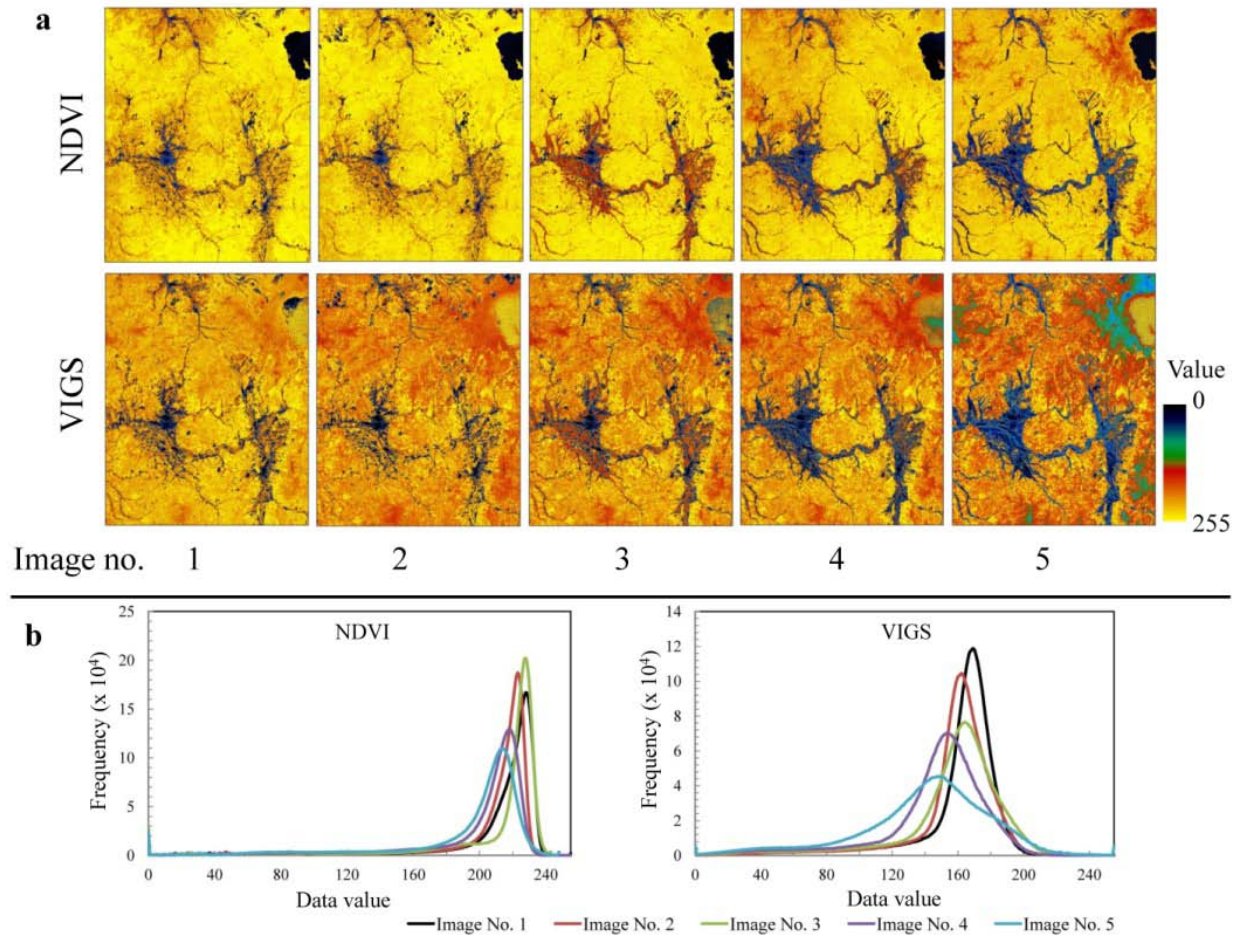


Fig. 5.7. (a) Comparison of NDVI and VIGS of the five images and (b) histogram of the NDVI and VIGS for multi-temporal images. The numbers in (b) refer to Table 5.2, indicating continuous conditions from summer to autumn. Each VI image is rescaled into 8-bit color using the initial NDVI range of 0 to 1 and the VIGS range of 0 to 3.6.

5.4.2. Spatial characterization of vegetation anomaly

The pixel-based ratio, m/σ , calculated from the five VIGS images is used to quantify anomaly intensity defined in Methods (Fig. 5.9a). This ratio should correct for elevation effects in the deciduous forests, which have seasonal changes and relatively low VIGS values, which are dominant at the high elevations (see Fig. 5.6a). This effect appears bluish as low value zones in

Fig. 5.9a, but could be reduced by the algorithm of the forced invariance method (Crippen & Blom, 2001). The method successfully reduces the contrast, which is shown in Fig. 5.9b.

Furthermore, a geostatistical technique and a residual analysis were applied to reduce variability of the corrected image by two steps: smoothing of the image by ordinary kriging with a unit cell size of $300\text{ m} \times 300\text{ m}$ (Fig. 5.9c) and production of a residual image by subtracting the regional trend from the kriging result (Fig. 5.9d). The regional trend was defined by a moving average of the kriging result within 8,500 m, a radius equal to the range of the semivariogram of the ratio (Fig. 5.8). Finally, the residual image was related to the distribution of ore deposits, as discussed in the next section.

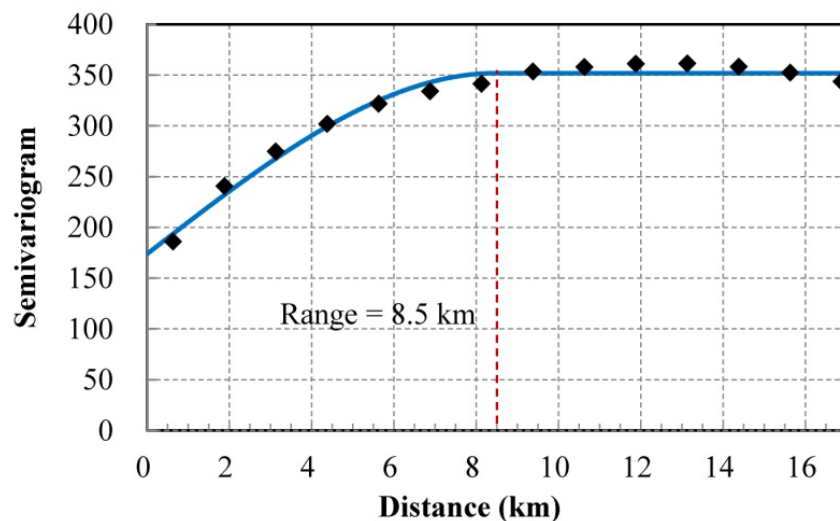


Fig. 5.8. Semivariogram of the ratio (mean standard deviation) of VIGS values. Experimental semivariogram (black diamonds) of the ratio, converted to a 0–255 integer scale, is fitted to the spherical model (blue curve). Range (the maximum correlation distance) is 8.5 km from the model.

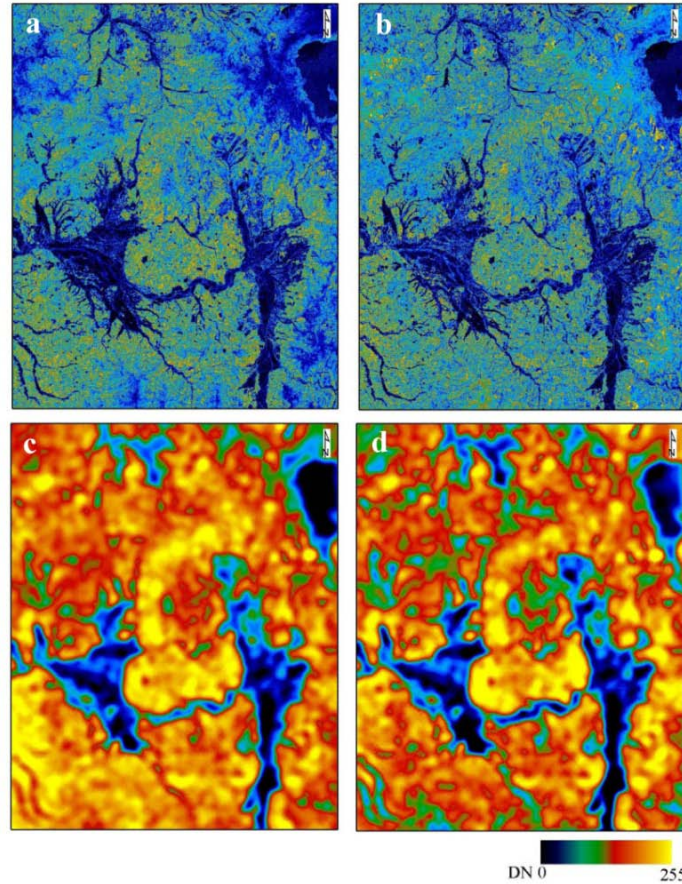


Fig. 5.9. Anomaly intensity images and image enhancement. (a) Original image using the ratio (m divided by σ) of VIGS values from the five Landsat ETM+ images. (b) Flattened image through the forced invariance method to correct the elevation effect. (c) Smoothed image using ordinary kriging with a unit cell of $300 \text{ m} \times 300 \text{ m}$ size. (d) Residual image to enhance anomalous ratios, which is (c) image minus regional trend. Values $< 0.2 \%$ and $> 99.8 \%$ in the cumulative distribution were removed as outliers. All images were rescaled into 8-bit integer.

5.4.3. Correlating vegetation anomaly with ore deposits potential map

This section evaluates the vegetation anomaly image obtained in the previous analysis and its relation to the distribution of ore deposits in the Hokuroku district. First, the residual image was grouped into three classes by thresholds using m and σ of the residual values of the

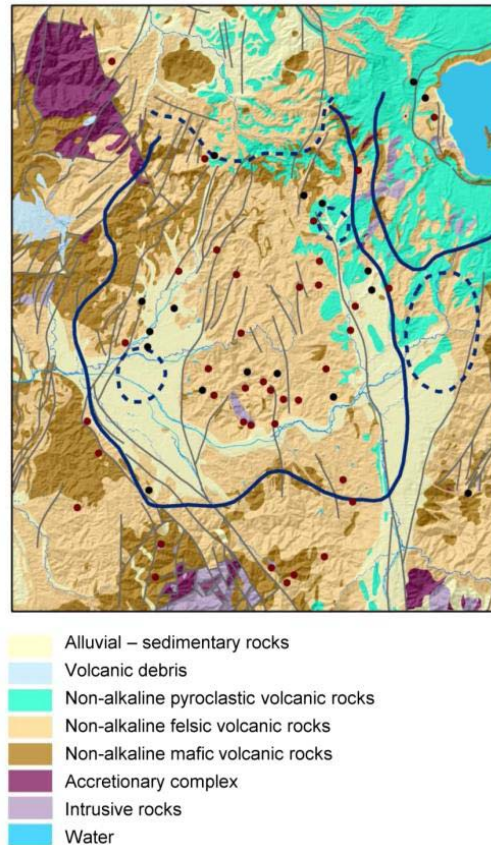


Fig. 5.11. Simplified division and facies map of the study area modified after a digital geological map (Wakitawa et al., 2009).

Next, the correlation of the three classes with geology. To consider how the main geologic units are related to ore deposits, the study area was divided into six major geological units based on rock divisions and facies; sediments (s), non-alkaline felsic volcanic rocks (vf), non-alkaline pyroclastic flow volcanic rocks (vp), non-alkaline mafic volcanic rocks (vb), accretionary complex from pre-Neogene (b), and intrusive/plutonic rocks (p) (Fig. 5.11). Because vf covers much of the study area (45.24 %), this unit occupies the largest frequency common to the three vegetation anomaly classes (Fig. 5.13a–c) and its relative dominancy increases from the background class to the high anomaly class, in particular in the evergreen

forest type (Fig. 5.13c). Accordingly, the VIGS-based vegetation anomaly is primarily distributed in the vf area. This trend is concordant with the fact that the deposits occur in the same horizon (Kouda & Koide, 1978; Ohmoto, 1978; Sato, 1974).

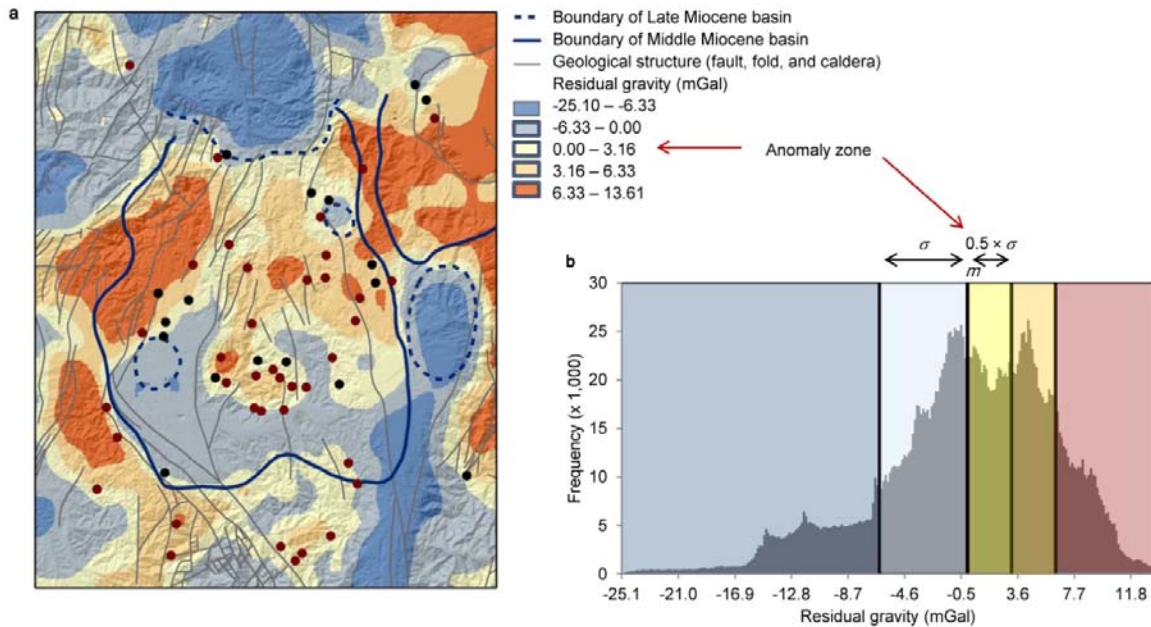


Fig. 5.12. Residual gravity map produced from the residual analysis. (a) Map of the residual gravity superimposed with the boundary of the Miocene basin and the major ore deposits. (b) Histogram of the residual gravity values, which are classified into five classes, based on the mean and standard deviations of residual gravity values.

The vegetation anomalies can be related to geophysical survey results. Gravity anomalies are a useful geophysical property for exploring basement rock structure and can be used to spatially characterize the ore deposits in the Hokuroku district (Komazawa, 1984; Nakajima, 1993). One example is that the deposits are distributed near the 0 mGal contour line of the residual gravity map (Komazawa, 1984). To test for a correlation with the vegetation anomalies,

residual gravity data were processed to extract anomalies by the same residual analysis used in Fig. 5.9d. The original residual gravity map was grouped into four classes (Fig. 5.12a) considering the shape of histogram of the residual values (Fig. 5.12b). The class between m and $m + 0.5\sigma$ was found to best correlate with the locations of major ore deposits. Also, this class shows the highest frequency in the high vegetation anomaly of the evergreen forest type, although the difference from the subordinate class is small (Fig. 5.13d–f).

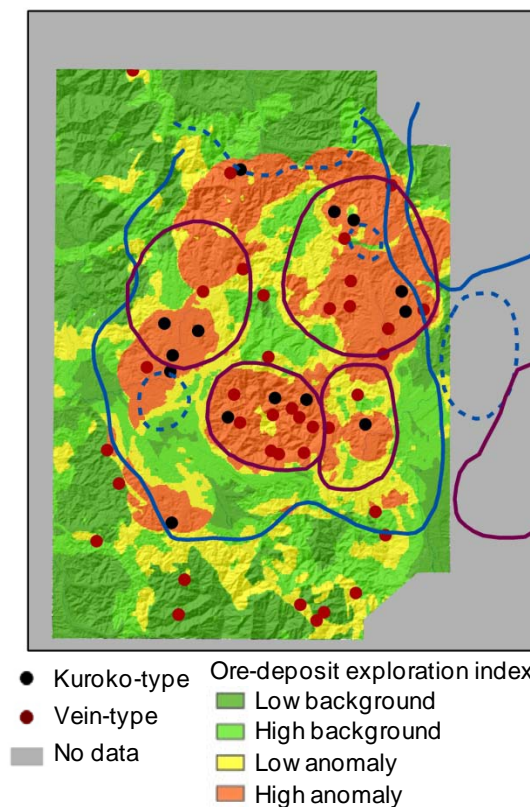


Fig. 5.13. Map of ore exploration index using multivariate regression analysis (Suzuki, 2003) overlaid with the possible ring structures and basin. No data is due to the availability geologic information as referred to detail geologic map scale 1:50,000 (Nakajima, 1989b).

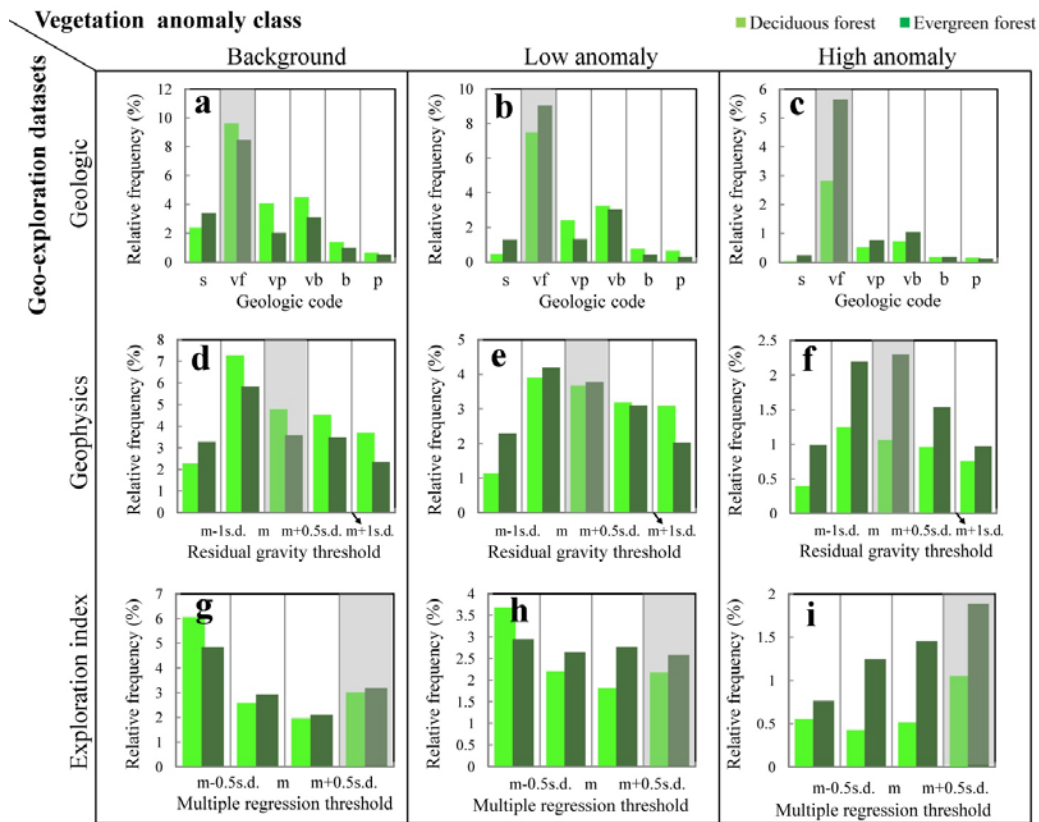


Fig. 5.14. Histograms of geo-properties classified by vegetation (deciduous and evergreen types) anomaly classes: (a–c) main geological units, (d–f) residual gravity, and (g–i) ore-deposit exploration index. The gray shadings in (a–i) denote the classes of each property related to ore deposits.

The vegetation anomaly is also evaluated against the exploration index using multivariate regression analysis based on the work of Suzuki, 2003. This index map may be the most comprehensive, precise to express the ore deposits distribution in the Hokuroku district using more factors than used in other studies (Koike, Matsuda, Suzuki, & Ohmi, 2002; Kubota, Urabe, Yamada, & Tanimura, 2004; Singer & Kouda, 1996). According to Suzuki’s report, multivariate regression analysis of seven factors, i.e., positional relation to dacitic sequence and upper layer, presence of ring structures, dacitic or rhyolite lava, andesite, vein-type deposits, alteration index,

and gravity anomaly. Based on the mapped results almost all major ore deposits were located in the range $\geq m + 0.43\sigma$ of the index values. The values were classified into four classes based on m and σ ; low background ($< m - 0.5\sigma$), high background (between $m - 0.5\sigma$ and m), low anomaly (between m and $m + 0.5\sigma$), and high anomaly ($> m + 0.5\sigma$). Although this index map is a part of the present study area, the distribution of high anomaly zones corresponds well to the high vegetation anomalies in Fig. 5.10a. This correspondence is verified in that the frequency of high anomaly zone is the largest in the high vegetation anomaly class common to the two forest types (Fig. 5.13g-i).

5.5. Discussion

The results show that the distribution of vegetation anomalies zones correspond well to the ore deposits potential zones extracted from geo-properties and encompass the major ore deposits located in dense forests. However, it is important to recognize the difference in the plant communities in terms of vegetation anomaly classes that we have defined. The background class, covering 56.05% of the study area, is composed of 40.42% deciduous forest type and the evergreen forest type with a similar rate (33.16%), while the high anomaly class area, covering 12.66% of the study area, is dominated by the evergreen forest type (63.29% cover rate) and the deciduous forest type (35.12%). This different rate suggests that the deciduous plants may be affected by external factors more strongly than the evergreen plants, which causes senescence and conceals the effect of metal-induced vegetation stress. This concealing may explain why the Nurukawa and Towada-ginzan mines are not located in the high anomaly class. However, our method successfully enhances anomalies in the deciduous plants along the main ring structures

(Fig. 5.9). This indicates the existence of key influence factor(s), considered below, causing vegetation anomalies around the ore deposits.

Common to the kuroko and vein-type deposits, the main minerals are sulfides in the Hokuroku district. Therefore, the top soils must be strongly acidic around the deposits caused by the oxidation and alteration minerals. Such low pH of the soil strongly affects plant physiological activity. Because the major ore deposits (all are currently closed mines), e.g. the Ezuri, Fukazawa, and Osarizawa, are concordantly located in the high anomaly class of vegetation, soil acidity can be regarded as the most plausible factor for the vegetation stress.

Several methods have been proposed to potential mapping of ore deposits in the Hokuroku district using multiple data sets of geological, geophysical, geochemical, and drilling surveys with spatial techniques such as geographical information system, neural network, and multivariate regression (Koike et al., 2002; Kubota et al., 2004; Singer & Kouda, 1996; Suzuki, 2003). However, potential mapping still requires improvement because of lack of outcrops, limited drilling density and depth, complicated generation mechanisms and structures of deposits, as usual cases. Although this proposed method uses only a set of reflectance spectra images of vegetation, the vegetation anomalies distribution was compatible with the high potential zones by preceding research. Therefore, a combination of VI, descriptive statistics of the temporal change in VI values, geostatistics, and residual analysis can give a preliminary potential map of deposits by emphasizing subtle vegetation stress in thick vegetation covered areas.

5.6. Conclusions

In conclusion, this chapter presents novel methods to detect vegetation anomalies caused by ore deposits and verify their usefulness by comparing the anomalies with a deposit potential

map produced from multiple geological data. The effectiveness of this method is demonstrated based on a case study in the Hokuroku district. The main results are as follows:

- The vegetation anomalies were detectable using VI analysis, in which a key variable to detect the anomalies was a variation of the VI with time at each pixel.
- Differences in variation were enlarged by a sequence of image-enhancement methods for the detection of vegetation-anomaly zones. The locations of vegetation-anomaly zones were found to be appropriate by comparing the anomalies with a deposit-potential map produced from multiple geological data.
- The above findings create the possibility of the extraction of valuable information that may reveal ore deposits below the surface by optimizing vegetation signatures at the surface, which can be combined with existing exploration databases.

References

- Bruce, B., & Hornsby, J. K. (1987). A Canadian perspective on the application of satellite remote sensing to regional geobotany. *Geocarto International*, 2(3), 53–59. <http://doi.org/10.1080/10106048709354108>
- Civco, D. L. (1989). Topographic normalization of Landsat Thematic Mapper digital imagery. *Photogrammetric Engineering and Remote Sensing*, 55, 1303–1309.
- Crippen, R. E., & Blom, R. G. (2001). Unveiling the lithology of vegetated terrains in remotely sensed imagery. *Photogrammetric Engineering and Remote Sensing*, 67(8), 935–943.
- Geological Survey of Japan (ed.). (2013). Gravity database of Japan, DVD edition, Digital geoscience map P-2. Geological Survey of Japan, AIST.
- Glasby, G. P., Yamanaka, T., Yamamoto, J., Sato, H., & Notsu, K. (2004). Kuroko and hydrocarbon deposits from Northern Honshu, Japan: a possible common hydrothermal/magmatic origin? *Resource Geology*, 54(4), 413–424. <http://doi.org/10.1111/j.1751-3928.2004.tb00217.x>

- Ishikawa, Y. (1991). *Kuroko: Kyoritsu Shuppan*. Tokyo, Japan.
- Koike, K., Matsuda, S., Suzuki, T., & Ohmi, M. (2002). Neural network-based estimation of principal metal contents in the Hokuroku district, Northern Japan, for exploring kuroko-type deposits. *Natural Resources Research*, *11*(2), 135–156. Retrieved from <http://link.springer.com/article/10.1023/A%3A1015520204066>
- Komazawa, M. (1984). On the quantitative gravimetric analysis in the Hokuroku district. *Geophysical Exploration*, *37*(3), 123–134.
- Kouda, R., & Koide, H. (1978). Ring structures, resurgent cauldron, and ore deposits in the Hokuroku volcanic field, northern Akita, Japan. *Mining Geology*, *28*(150), 233–244. <http://doi.org/10.11456/shigenchishitsu1951.28.233>
- Kubota, H., Urabe, T., Yamada, R., & Tanimura, S. (2004). Exploration indices and mineral potential map of the Kuroko deposits in northeast Japan. *Resource Geology*, *54*(4), 387–397.
- Nakajima, T. (1989a). Explanation text of the geological map for mineral resources assessment of the Hokuroku district, scale 1:50,000, Miscellaneous Map Series 27. Geological Survey of Japan.
- Nakajima, T. (1989b). Geological map for mineral resources assessment of the Hokuroku district, scale 1:50,000, Miscellaneous Map Series 27. Geological Survey of Japan, AIST.
- Nakajima, T. (1993). Reconstruction of the depositional circumstances of the Kuroko deposits in the Hokuroku basin. *Bulletin of the Geological Survey of Japan*, *44*(2/3/4), 251–282.
- Ohmoto, H. (1978). Submarine calderas: A key to the formation of volcanogenic massive sulfide deposits? *Mining Geology*, *28*(150), 219–231. <http://doi.org/10.11456/shigenchishitsu1951.28.219>
- Ohmoto, H. (1996). Formation of volcanogenic massive sulfide deposits: The Kuroko perspective. *Ore Geology Reviews*.
- Sato, T. (1974). Distribution and geological setting of the kuroko deposits. In T. Ishihara (Ed.), *Geology of kuroko deposits. Mining geology special issue No. 6* (pp. 1–10). Society of Mining Geologists of Japan.
- Sato, T. (1977). Kuroko deposits: their geology, geochemistry and origin. *Geological Society, London, Special Publications*, *7* (1), 153–161.

- Sato, T., Tanimura, S., & Ohtagaki, T. (1974). Geology and ore deposits of the Hokuroku district, Akita prefecture. In T. Ishihara (Ed.), *Geology of kuroko deposits. Mining geology special issue No. 6* (pp. 11–18). Society of Mining Geologists of Japan.
- Scott, S. D. (1978). Structural control of the Kuroko deposits of the Hokuroku district, Japan. *Mining Geology*, 28(151), 301–311. <http://doi.org/10.11456/shigenchishitsu1951.28.301>
- Singer, D., & Kouda, R. (1996). Application of a feedforward neural network in the search for Kuroko deposits in the Hokuroku district, Japan. *Mathematical Geology*, 28(8), 1017–1023. <http://doi.org/10.1007/BF02068587>
- Suzuki, T. (2003). Application of multiple regression analysis to extract promising areas of kuroko deposits in the Hokuroku area, Akita pref., Japan. *Shigen-to-Sozai*, 119(4,5), 149–154. <http://doi.org/10.2473/shigentosozai.119.149>
- Wakitawa, T., Igawa, T., & Takarada, S. (2009). Seamless geological map of Japan at a scale of 1:200,000 DVD edition, Digital Geoscience Map G-16. Geological Survey of Japan, National Institutes of Advanced Industrial Science and Technology.
- Yamada, R., & Yoshida, T. (2011). Relationships between Kuroko volcanogenic massive sulfide (VMS) deposits, felsic volcanism, and island arc development in the northeast Honshu arc, Japan. *Mineralium Deposita*, 46(5), 431–448.
- Zirschky, J. (1985). Geostatistics for environmental monitoring and survey design. *Environment International*, 11(6), 515–524. [http://doi.org/10.1016/0160-4120\(85\)90187-4](http://doi.org/10.1016/0160-4120(85)90187-4)

Chapter 6

Detection of hydrothermal alteration zones in a dense vegetated area by directed principal component analysis

6.1. Introduction

The preceding three chapters (Chapter 3–5) used the basic assumption that the satellite image pixels were almost entirely vegetation. However, there is a possibility that the spectra on the image pixels were mixtures of vegetation, soil, rock, and other features; the contributions of soil and rock reflectances were more or less included. Thus, this chapter was built prior upon to this spectra mixture problem.

One of the methods that has been widely used to solve the problem of spectral mixture is the principal component analysis (PCA). Researchers have used two image enhancement PCA-based methods in remote sensing applications for mineral exploration in vegetated areas. First is the PCA examination of selected bands of the satellite image, which was introduced by Crosta & Rabelo (1993) and is known as the Crosta technique. The Crosta technique analyzes the eigen factors of the PCA results from satellite imagery bands, and the result is compared with the spectral characteristics of target materials (soil or rocks). The second method is called directed principle component analysis (DPCA), where the intention is to enhance the mineral signatures by reducing the effects of plants by optimization from a limited number of selected band ratios (Fraser & Green, 1987). Both PCA and DPCA, in the early stage of their development, were applied for the detection of clay and iron oxide minerals; this application is being continued by several researchers (Crósta et al., 2003; Liu et al., 2011; Pour et al., 2013; Tangestani & Moore,

2000, 2001; Tiwari et al., 2011). In a recent development, DCPA was evolved to interpret hydrothermal alterations zones by integration with geographic information systems (GIS)-based image classification (Carranza & Hale, 2002). Hereafter, the present study focuses on improving the DPCA method.

The standard DPCA method uses two simple ratios to represent the vegetation and components of interest (minerals or rocks). The ratio for vegetation components is derived from the simple band ratio $0.83/0.66 \mu\text{m}$ or $0.56/0.66 \mu\text{m}$ (Carranza & Hale, 2002; Fraser & Green, 1987). The simple band ratio used to represent the mineral component is similar to that developed by Rowan et al. (1974). On the other hand, the preceding studies mostly use Landsat images that have band restrictiveness. In this study, I focused on the Advanced Spaceborne Thermal Emission and Reflection Radiometer (ASTER) image that has more advanced capability to discriminate minerals and rocks through wider range of data, i.e., 3 bands in the visible and near-infrared (VNIR) with 15-m spatial resolution, 6 bands in the short-wave infrared (SWIR) with 30-m spatial resolution and 5 bands in the thermal infrared (TIR) with 90-m spatial resolution. This research is aimed to improve the DPCA method and enhance the hydrothermal alteration zone in a vegetated area by optimizing the combination band ratio integrated with GIS-based analysis. The possibility of an optimization ratio derived from a wider band combination to represent the components (vegetation and minerals) is explored. However, the method still required spectral characteristics evaluation before the ratio was selected and controlled by the ground truth data. To my knowledge, this is the first DPCA-based study to examine the vegetation-mineral relation by using both of ASTER data and a combination band ratio rather than a simple ratio to represent the vegetation and mineral components.

6.2. Study location and geologic setting

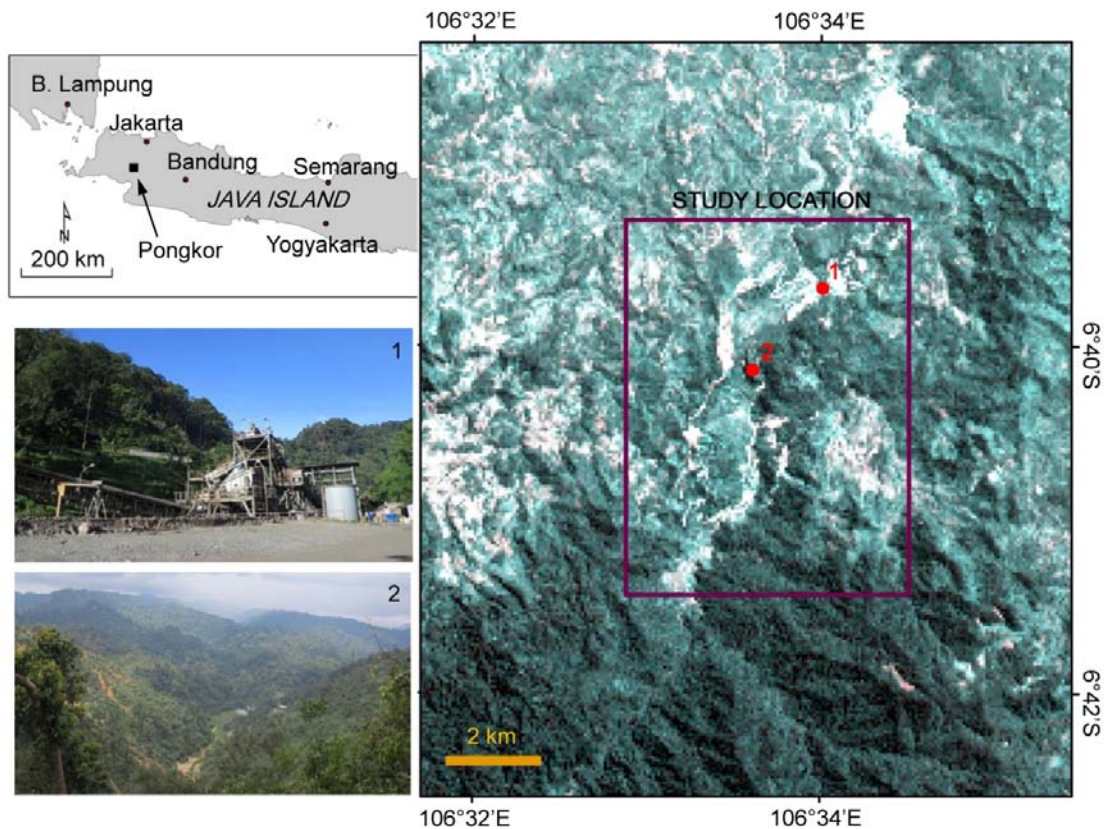


Fig. 6.1. Study location in Pongkor, West Java province, Indonesia, superimposed on an ASTER image of the true-color band 2, 1, and 1 in the RGB composition acquired on 15 June 2006. Insert photos 1 and 2 refer to points 1 and 2 at the map of the location and are the view of Pongkor's location taken in the center of the mine plant site toward the southwest and the aerial of the actual vegetation cover in the south direction, respectively.

The Pongkor region, located in Bogor District, West Java, Indonesia (Fig. 6.1), was chosen for the present study for the following reason. This field is an active underground mine operated by the state mining company, PT. Aneka Tambang (Antam), and has been thoroughly geologically explored. The estimated total reserve as of December 2014 was 2.12 tons, with

metal contents of Au 5.1 ppm and Ag 70 ppm on average (PT Aneka Tambang, 2014). The elevation range of the study area is 425-1,125 m a.s.l., and the land cover type includes bare soil, urban area, paddy field, plantations, bushes and forest. Moreover, based on the supervised land cover classification using Bakosurtanal (2000), more than 38% of the region is heavy forest as part of the Mount Halimun Salak National Park.

The geologic setting of the Pongkor deposit is at the northeastern flank of the Bayah Dome (Fig. 6.2a), one of the main hosts of several epithermal deposits in the western part of Java (Basuki et al., 1994; Marcoux & Milési, 1994). It is an inlier of the reputedly Miocene volcano-sedimentary rocks composed within the Pliocene-Quaternary volcanites (Milési et al., 1999). The deposits have an intimate relationship with a circular structure (8 km diameter in size), which is interpreted as a volcano-tectonic depression (caldera) associated with ignimbrite volcanism (Fig. 6.2b). The general lithologic unit is composed of three main units, which can be described as follows. Recent andesitic volcanic rocks are found at the southern edge of the Pongkor caldera. These rocks are also well developed in the central part along a north-south axis that corresponds to a fault. The explosive subaerial dacitic volcanic rocks, which can be divided into several units, occupy the middle stratigraphic. The unit members include a basal with accretionary lapilli tuff, lapilli-block tuff, and pyroclastic tuff–epiclastic siltstone in the topmost subunit. The Pongkor veins are mostly within the lapilli-block tuff. The lower unit is characterized by andesitic volcanic rocks. This unit is exposed around the Cikaniki and Ciguha River, and the majority is on the western edge of the Pongkor caldera.

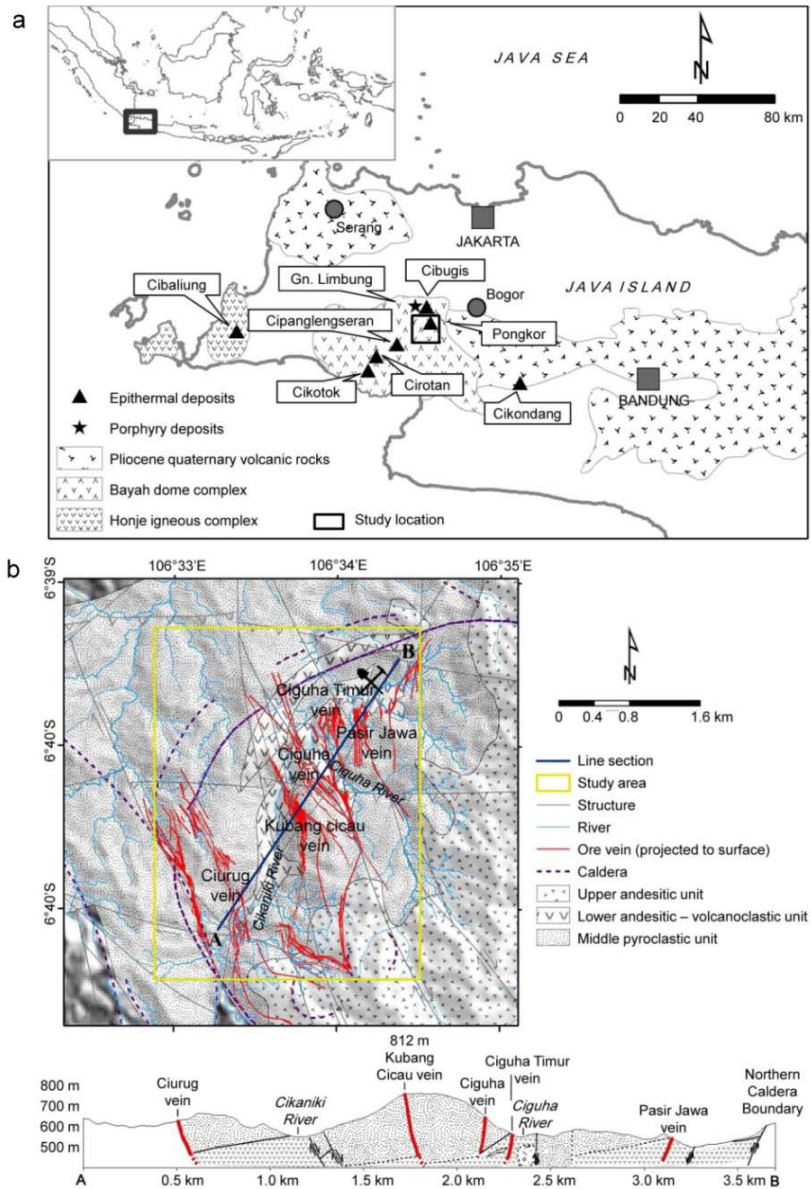


Fig. 6.2. (a) Location of the study site, Pongkor mine and (b) regional geological map with schematic cross section (A-B) showing the main ore veins of the Pongkor deposits modified from Milési et al. (1999).

The Pongkor deposit is low sulfide, Au-Ag, epithermal type (Milési et al., 1999). Pongkor's mineralization is controlled structurally by vein systems with steep dips. The major faults host some NW-trending ore bodies, and the others are hosted by minor faults. The major

veins are the Pasir Jawa, Gudang Handak, Ciguha, Kubang Cicau, and Ciurug veins (see cross section in Fig. 6.2b). The vein thickness varies, e.g., at the Ciguha vein, the thickness is approximately 2 km in length, and there is a 2-m-thick outcrop that reaches up to 24 m ore-body thickness under the surface (Syafrizal et al., 2005).

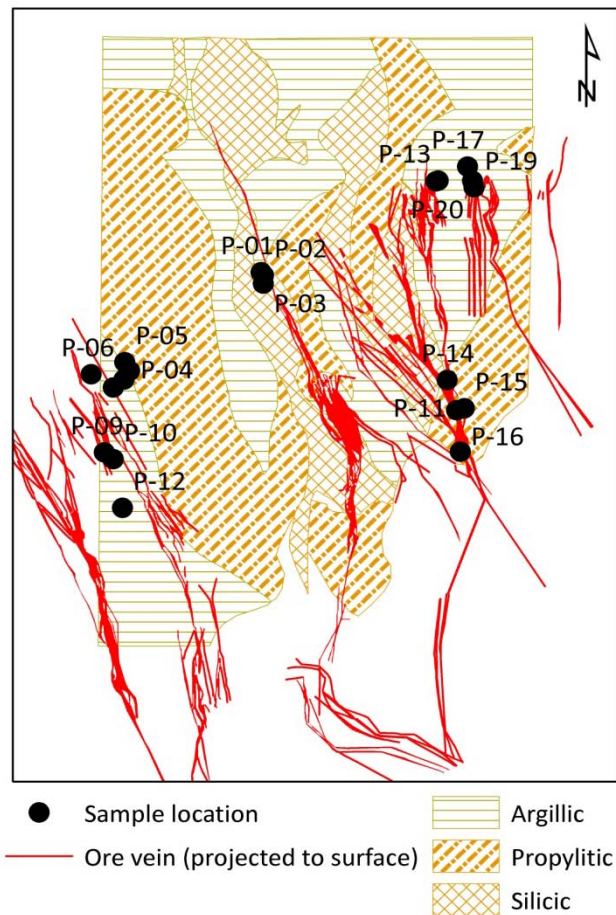


Fig. 6.3. Alteration map of the Pongkor region modified from Basuki et al. (1994).

The hydrothermal alteration zone is spread widely around the Pongkor vein system (Basuki et al., 1994). There are three main types of alteration, i.e., propylitic, argillic, and silicification alteration (Fig. 6.3). Propylitic alteration is characterized by chlorite, epidote,

carbonate, and quartz minerals and is distributed mainly in the eastern and western parts of the major veins and in the lower part of the Cikaniki River valley. Argillic alteration, marked by the presence of illite, kaolinite, smectite, montmorillonite, quartz, and pyrite, is spread over hundreds of meters around the veins and throughout the tuff units. Silicic alteration (quartz > 40%) occurs around the Kubang Cicau and Ciguha veins along andesitic unit and extends toward to north through the highest elevation of Gunung Pongkor. Recent publication, e.g., Syafrizal et al. (2007), discussed more detail information about the conceptual genetic model of hydrothermal alteration zones of the Pongkor deposits as shown in Fig. 6.4.

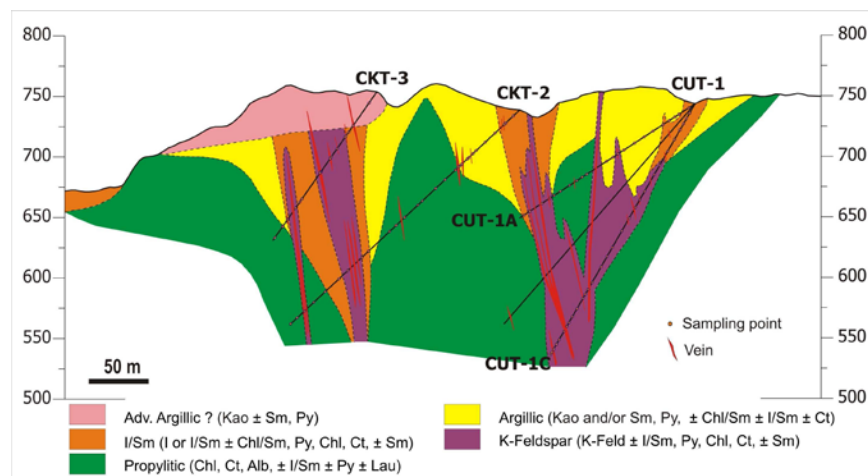


Fig. 6.4. Simplified longitudinal section of the hydrothermal alteration of Cikoret and Ciurug Utara (Syafrizal et al., 2007).

6.3. Materials and methods

6.3.1. Satellite image data

A subscene of the ASTER data level-1B acquired on 15 August 2002 from the ASTER Ground Data System (GDS) Japan Space Systems (J-spacesystems) was used in this study. This

image registered radiance at the sensor without atmospheric correction from the original level-1A. The cloud cover over the study area is nearly 0%. The standard procedure of preprocessing ASTER data was undertaken, including crosstalk correction (Iwasaki & Tonooka, 2005) performed by Crosstalk correction software (www.gds.aster.ersdac.or.jp) and image georeferencing using local topographic map made by PT. Antam. The image was also processed for atmospheric correction by using the FLAASH module in ENVI software (ver 5.2).

6.3.2. Ground-truth data

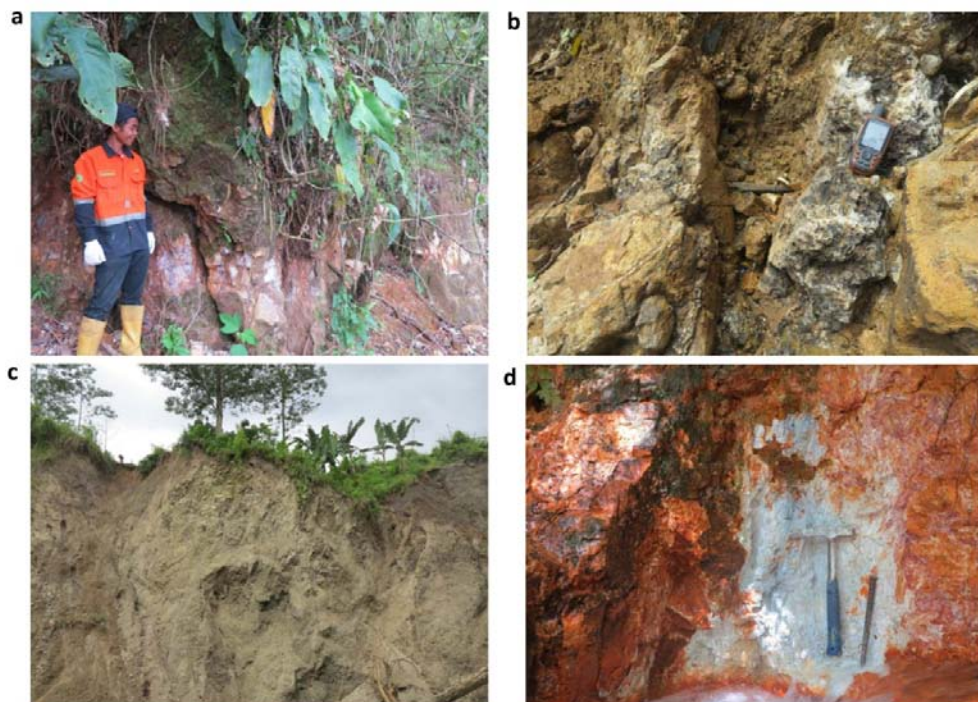


Fig. 6.5. Field photographs show (a) quartz vein, (b) weathered quartz vein with some manganese-oxides, (c) exposed pyroclastic soils, and (d) altered kaolinite with an abundance of highly oxidized pyrite.

A field survey was performed for geological observation, ground checking, and collecting the samples (Fig. 6.5). The ground-truth data were used to calibrate the remote sensing analysis and the interpretation of the results. The 25 surface samples, which included 13 soil samples and 12 rock samples, were collected during a field survey on 12–15 April 2014, and their location was scattered around the Pongkor deposits (see Fig. 6.3). The soil samples were taken from a depth of 5–20 cm below the surface. The chip sampling method was used to collect the rock samples, which included fresh and weathered rocks. Their positions were recorded using a handheld GPS Garmin eTrex with a 3–4 m error.

To identify the characteristics of the samples in terms of physical and mineral properties, samples were measured by petrographic and spectroscopic analysis. Spectral reflectance measurements were performed using a FieldSpec3 Spectroradiometer (Analytical Spectral Devices, Boulder, CO, USA) with a contact probe and built-in illumination sources. The mineral composition analysis was performed by petrographic analysis using a Nikon E200 Polarization microscope and X-ray diffraction (XRD) analysis using an XRD 7000 Shimadzu.

6.3.3. DPCA and GIS-based analysis

Theoretically, DPCA converts a set of correlated components into uncorrelated components termed principal components. The interpretation of the results is simple because the number of input components is limited to two specific components, i.e., vegetation and mineral components. The computation of DPCA generates two DPC images, each of which represents the contribution of the interfering component of both ratios and highlights the unique contribution for each component (Fig. 6.6). Based on the analysis of the loading factors, the DPC1 images mostly contain the contribution of the interfering component in both ratios

(vegetation and mineral components) and cannot discriminate clearly between the vegetation and mineral components. In contrast, DPC2 images are suitable for this discrimination. A positive or a negative sign of the loading (depending on the eigen factor) on the mineral components can be used as an indicator of mineral enrichment areas for further analysis.

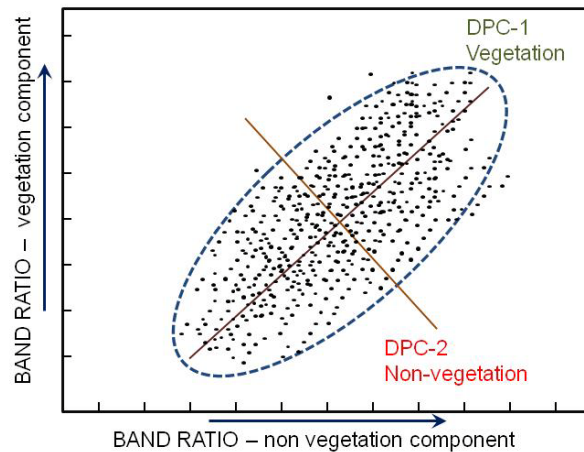


Fig. 6.6. Schematic representation of the DPC analysis (Fraser & Green, 1987).

The above figure indicates the following specific requirements in selecting the optimum band ratio to represent vegetation and non-vegetation (rock/mineral) components. To select the band ratios, an understanding of the reflectance spectra pattern characteristics is needed. Carranza & Hale (2002) suggested that the band ratio for vegetation in both images must be high based on the vegetation reflectance spectra but that the band ratio for rock/mineral can be high (above the average value) or low (below it). Another important consideration is that the result of the measured variables of PCA is scale dependent, and the histogram of the band ratio results need to be standardized by histogram equalization (Carranza & Hale, 2002; Fraser & Green, 1987). In this study, each ratio image was standardized into an 8-bit digital number (DN: 0–255), with an average of 128 by histogram Gaussian stretch.

The next step is a GIS-based analysis to interpret the DPCA results. To remove noise and enlarge the contrast, I use a geostatistical approach for smoothing the DPCA images result followed by fuzzy logic operation to classify the mineral images resulting from the DPCA. Semivariogram analysis produces a curve that is well fitted to a spherical model; the new smooth raster is created by simple kriging (SK) interpolation.

The fuzzy values are used to determine the mineral distribution, overlay the images of each mineral feature, and generate the distribution map of the hydrothermal alteration zones. To assign fuzzy membership values for each mineral image from the DCPA, I used the fuzzy LARGE function. Fuzzy logic with the AND operator was used to overlay the map based on the mineral characteristics of each alteration type. The final image is also validated by the hydrothermal alteration map using the geological investigations of PT. Antam (unpublished data) combined with those of Basuki et al. (1994). However, because there is land cover that might be affected by anthropogenic factors, e.g., populated areas, paddy fields, and open water, the pixels created by the supervised land cover map must be delineated during the image analysis to avoid over-corrections. The overall procedures of the image processing and interpretation are summarized in the flow chart of Fig. 6.7.

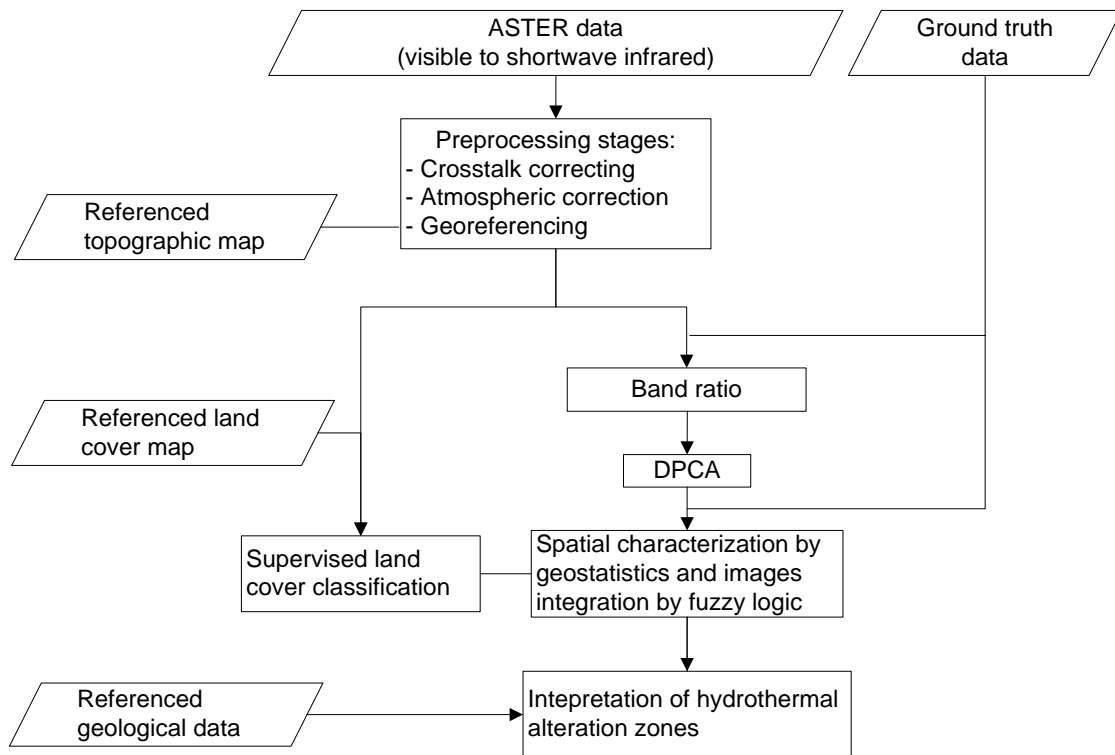


Fig. 6.7. Workflow of the image processing and interpretation.

6.4. Results and Discussion

6.4.1. Petrographic and spectroscopy analyses

The petrographic analysis showed that quartz vein samples typically consist of anhedral holocrystalline that is predominantly composed of quartz and slightly opaque minerals, locally quartz with layering and a comb structure (Fig. 6.8a). There are two types of quartz: coarse and fine-grained quartz minerals in the form of microgranules. Opaque minerals, which are generally anhedral, spread both as individuals and groups and are slightly oxidized to brownish-black iron oxide. Thin sections prepared from pyroclastic rocks showed the texture of sub-angular, matrix supported, poorly sorted, composed by andesitic rock fragments, claystone, quartzite, plagioclase and opaque minerals filling in the fine cracks (Fig. 6.8b). Plagioclase shows a twin structure, generally fine cracks, filled or replaced with opaque minerals, partially altered to sericite.

Opaque minerals are spread in the base period, mostly in the andesitic rock fragments and fill fine cracks, and are oxidized to iron oxide and covered the surface of rocks.

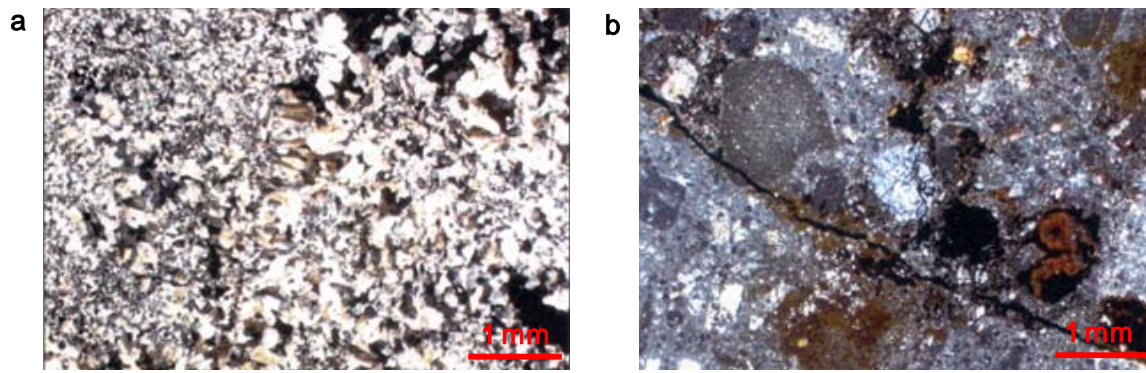


Fig. 6.8. (a) Microphotograph of a quartz vein showing mostly coarse-grained quartz layering with microgranule quartz. (b) Altered tuff litic formed by fragments of andesitic, quartzitic, plagioclase, clay and opaque minerals in a polished section.

In relation to the spectroscopic analysis, Hauff (2008) summarized that spectroscopic analyses are based on the spectral properties of materials as a function of electron transition in the visible region and the composition of the minerals in the SWIR region (Table 6.1). Fig. 6.9a shows the typical reflectance spectra of rock samples in particular quartz veins. There are two main types: fresh veins rocks (e.g., sample ID; P-13, P-15, and P-18) and altered rocks, which show the presence of abundant clay minerals and secondary iron minerals that can be reflected by spectral analysis (e.g., sample ID; P-01, P-14, and P-15). The difference in the spectral pattern was characterized by the abrupt changes in the visible region caused by iron oxyhydroxides, such as Fe^{2+} (chlorite) and Fe^{3+} (hematite–goethite). Another common feature is water absorption around $\sim 1.4 \mu\text{m}$ and $\sim 1.9 \mu\text{m}$.

Similar features were found for soil samples, except for the depth of water absorption; for the rock samples, the overtone of an O-H stretch vibration of water (H-O-H) is longer than it is for the soil samples (Fig. 6.9b). XRD analysis was conducted for 10 soil samples and showed that the soil mineral composition is dominated by quartz-illite-kaolinite-montmorillonite (e.g., sample ID; P-04, P-05, and P-16) and quartz-montmorillonite-albite (e.g., sample ID; P-07 and P-12). In addition, I used other spectral references from the United States Geological Survey (USGS) spectral library and the Jet Propulsion Laboratory (JPL) spectral library (Baldrige et al., 2009), as shown in Fig. 6.10.

Table 6.1. Common absorption features in the SWIR region related to the type of minerals (Hauff, 2008).

Wavelength	Absorption feature	Mineral group
~1.4 μm	OH and water	clays, sulfates hydroxides, zeolites
~1.56 μm	NH_4	NH_4 species
~1.8 μm	OH	sulfates
~1.9 μm	Water	smectites
~2.02, 2.12 μm	NH_4	NH_4 species
~2.2 μm	Al-OH	clays, sulfates, micas
~2.29 μm	Fe-OH	Fe-clays
~2.31 μm	Mg-OH	Mg-clays, organics
~2.324 μm	Mg-OH	chlorites
~2.35 μm	CO_3^{-2}	carbonates
~2.35 μm	Fe-OH	Fe-chlorites

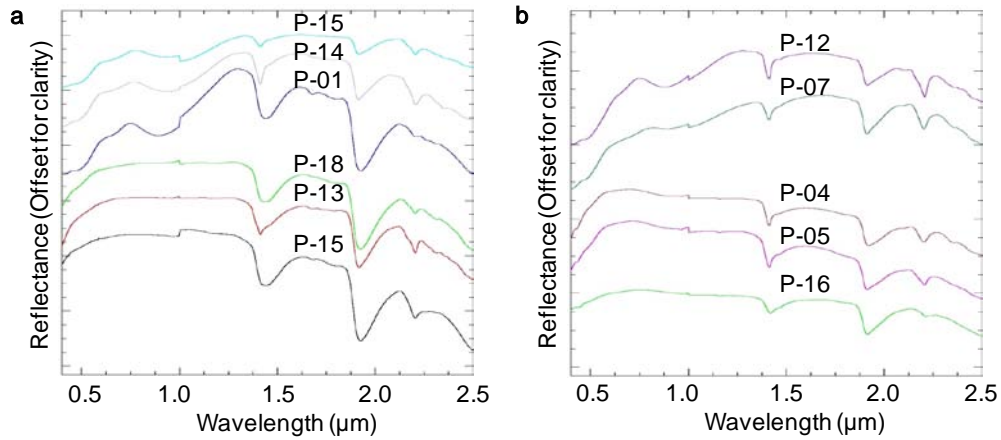


Fig. 6.9. Typical spectral analysis results for (a) rock and (b) soil samples. See Fig. 6.3 for sample locations.

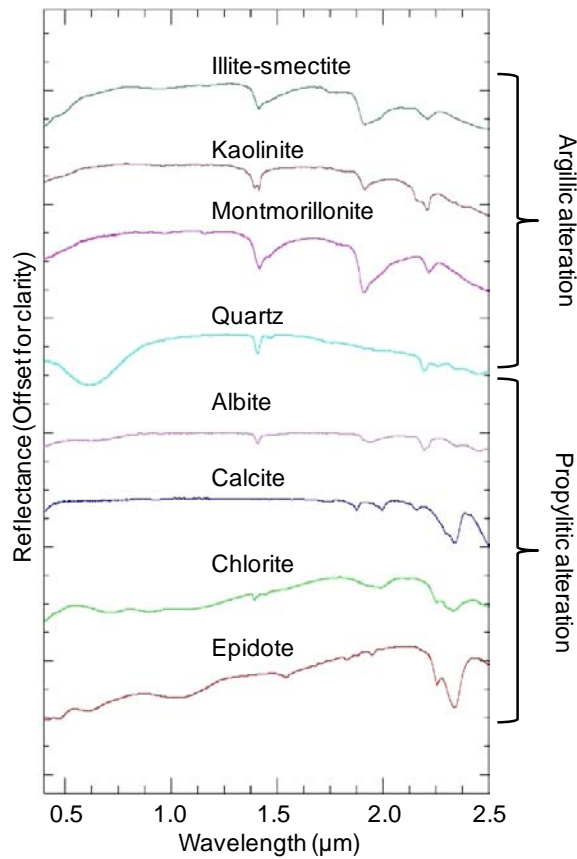


Fig. 6.10. The spectral plots for key minerals end-members that can be related to the type of argillic and propylitic alterations from the USGS and JPL spectral library.

6.4.2. Selection of band ratios and DPCA results

In the present study, the band ratio in the form of the normalized difference-based ratio rather than a simple ratio to identify the vegetation and mineral components for the following reasons was used. The normalized difference-based ratio, defined as $(b_i - b_j) / (b_i + b_j)$, where b_i and b_j are two selected bands at band i and j , can enhance the variation of the spectral reflectance between two wavelength bands. Another advantage of the normalized difference index-based ratio is to delimit the lower and upper bound result values. Traditional DPCA uses the simple ratio (b_i / b_j) to define the components, and there is a limitation as the denominator approaches zero. Then, the ratio result is without bound.

The normalized difference vegetation index (NDVI), where the NIR and red bands are equal to bands 3 and 2 in the ASTER data, respectively, satisfies the prerequisite for the vegetation components because it is high in the vegetation pixels and relatively low for the non-vegetation components. To select optimum band ratio to represent the minerals component, I must understand the typical hydrothermal alteration minerals that are developed around the ore deposit. Fig. 6.11 shows the relation between the spectral features compared with the ASTER band data used in this study. Argillized samples show a clear reflectance absorption of Al-OH at the wavelength of 2.17–2.20 μm (ASTER bands 5 and 6), which is specific to kaolinite-alunite-illite minerals (Fig. 6.11a). Propylitic minerals, such as epidote and chlorite, are characterized by the Fe- or Mg-OH reflectance absorption at 2.35 μm , which corresponds to ASTER band 8 (Fig. 6.11b). Therefore, based on the above features, I use a combination of bands 3, 4, 5, and 6 to enhance the argillic alteration. Then, bands 2, 5, 7, and 8 are used as the input images for propylitic alteration in the DPC analysis. Table 6.2 shows a list of the selected bands employed in this study.

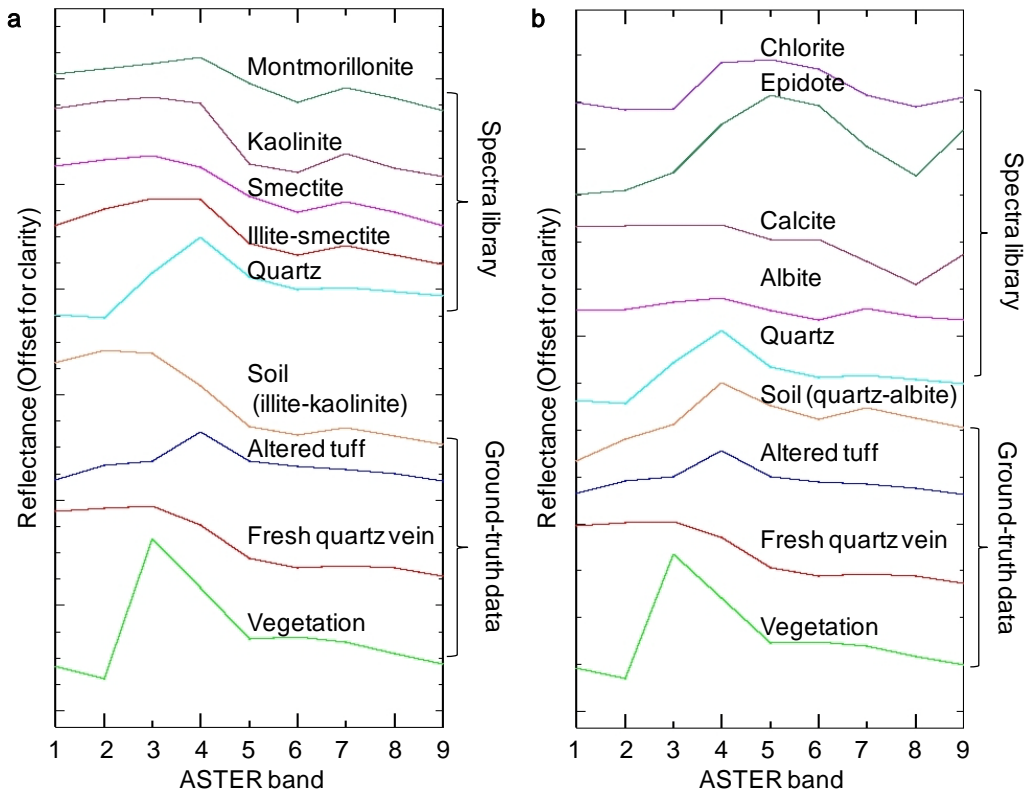


Fig. 6.11. Plots of the reflectance spectra of typical hydrothermally altered minerals (propylitic and argillic alterations) and vegetation. The reflectances are at the ASTER bands.

Table 6.2. List of selected bands (b_i and b_j) that used in the normalized difference-based ratio $((b_i - b_j) / (b_i + b_j))$ as the input images for DPCA.

Mineral features	b_i, b_j ; two selected bands, according to ASTER bands	
	Vegetation component	Mineral component
Kaolinite	bands 3, 2	bands 3, 5
Illite-smectite	bands 3, 2	bands 4, 6
Quartz	bands 3, 2	bands 7, 2
Chlorite-Epidote	bands 3, 2	bands 5, 2
Albite	bands 3, 2	bands 5, 8

The results of DPCA, interpreted as mineral images overlaid with ore veins projected onto surfaces, are shown in Fig. 6.12b–f. As a comparison, Fig. 6.12a is a subscene of the ASTER data used in this study, as shown in true color composite (RGB; band 3, 2, 1). The color brightness in the mineral images indicates the relative abundance of minerals, where bright pixels represent enriched areas. For example, argilized minerals (kaolinite, illite, and smectite) are found in the central, western, and southern parts of the study area, which are relatively closely related to the main vein deposits (Fig. 6.12b–c). Due to the spectral similarity between quartz and other propylitic minerals, e.g., chlorite and epidote (see Fig. 6.11b), the results of the DPCA images are similar (Fig. 6.12d–f). The quartz and propylitic images reveal vein deposits in the central and southern regions.

Each of the mineral images is extracted using the fuzzy LARGE function to generate fuzzy members for each mineral. Fuzzy member values closer to 1 indicate that the original DN from the DPCA is close to 255 and that the probability of mineral existence is high. It is inevitable that some fuzzy members have similar values for different mineral components due to the similarity in the patterns of the reflectance spectra. The next process is to incorporate the fuzzy member value of each mineral feature using fuzzy logic and the AND operator. A fuzzy logic method integrates the raster layers from the DPC analysis into the integrated alteration maps, which can be divided into two main alteration zones, i.e., argillic (Fig. 6.12g) and propylitic alteration (Fig. 6.12h) zones.

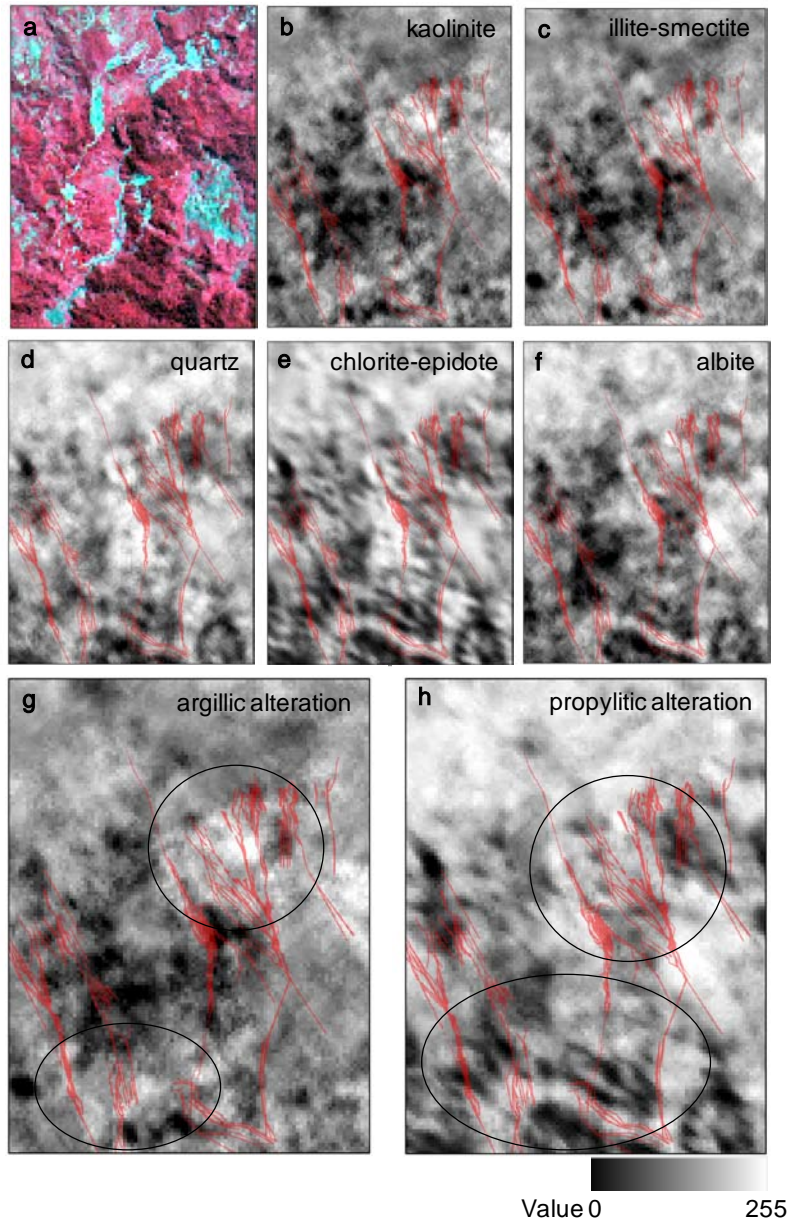


Fig. 6.12. (a) False-color bands 3, 2, and 1 in RGB composition compared with (b–f) the mineral images in 8-bit color from the DPCA and GIS-based analysis can be used as an indicator of hydrothermal alteration zones. Final images of (g) argillic alteration zones resulting from image combination (b-c) and (h) propylitic alteration zones resulting from image combination (d-f). The image combination using the fuzzy logic operation in ArcGIS 10.2. Mineral-alteration images were overlaid by vein deposits (red lines) projected onto the surface.

The propylitic zones extracted from the image analysis (Fig. 6.12h) are located mostly around the mineralization of the Pongkor deposits. The zones also correspond to the hydrothermal alteration map, particularly in the southern and central parts of the study area. However, the significant brightness areas, as indicators of propylitic zones, found in the northern part are not related to Pongkor mineralization, which might be caused by anthropogenic factors. In these areas, there are many paddy field and agricultural fields, which are contaminated by metal-rich fertilizers.

One concern related to the result is that the alteration zones (based on the alteration map, see Fig. 6.3) were not perfectly mapped as alteration zones, especially for the argillic alteration zones (Fig. 6.11g). This incompleteness can be explained by the fact that the mineral abundance in this area is not sufficient to enhance the reflectance spectra response. However, our result is reasonable based on the distribution of the ore veins, where the alteration zones from DPCA successfully enhanced the mineralization areas and concentrated only around Pongkor deposits. Another reason for the unsuccessful DPCA enhancement of the alteration zones, particularly, the argillic alterations in some parts, is the geological condition of the Pongkor deposits. Milesi et al. (1999) reported that the hydrothermal alterations in the Pongkor area are generally overprinted by supergene weathering products and intensively covered an argillic zone, which caused confusion in the detection of hydrothermally altered rocks. However, hydrothermal alteration zones are often inconsistent due to the overlap of the mineral constituents. Finally, the DPCA can work well only if the soil surfaces can be seen between the trees. If the vegetation is too dense, a geobotanical method is possible for detecting the anomalies caused by hydrothermal mineralization.

6.5. Conclusions

This study demonstrated the application of satellite remote sensing using ASTER data for detecting the hydrothermal alteration zones covered by thick vegetation. An improvement of the DPCA method by optimizing the combination band ratio integrated with GIS-based analysis successfully enhanced the hydrothermal alteration zones, which are closely related to the distribution of epithermal gold deposits in Pongkor district, Bogor, Indonesia. The main results can be summarized as follows.

- ASTER data provide a wider range of bands to discriminate mineral alteration characteristics that are useful in selecting band combinations in DPCA methods. There are more options to explore the optimum band combinations as representations of vegetation and mineral components.
- The present study used the normalized difference-based ratio for rationing the bands, which has advantages over the simple ratio used in traditional DPCA, e.g., enhanced variations of the spectral reflectance between two wavelength bands and delimited lower and upper bound values.
- By the DPCA combined with geographic information system (GIS)-based analysis, it is confirmed that the alteration and mineralization zones are enhanced largely despite the area covered by thick vegetation.
- The alteration zones extracted by this combination were confirmed to be plausible and consistent with the mineralization and alteration zones. However, there are some considerations related to unsuccessful of DPCA to enhance the alteration zones that may be caused by geologic and vegetation cover conditions.

References

- Bakosurtanal. (2000). Indonesia digital land cover map, 1:25.000, sheet no. 1209-131, Cihiris. Bogor: National Coordinating Agency for Surveys and Mapping (Bakosurtanal).
- Baldrige, A. M., Hook, S. J., Grove, C. I., & Rivera, G. (2009). The ASTER spectral library version 2.0. *Remote Sensing of Environment*, 113(4), 711–715. <http://doi.org/10.1016/j.rse.2008.11.007>
- Basuki, A., Aditya Sumanagara, D., & Sinambela, D. (1994). The Gunung Pongkor gold-silver deposit, West Java, Indonesia. *Journal of Geochemical Exploration*, 50(1-3), 371–391. [http://doi.org/10.1016/0375-6742\(94\)90032-9](http://doi.org/10.1016/0375-6742(94)90032-9)
- Carranza, E. J. M., & Hale, M. (2002). Mineral imaging with Landsat Thematic Mapper data for hydrothermal alteration mapping in heavily vegetated terrane. *International Journal of Remote Sensing*, 23(22), 4827–4852. <http://doi.org/10.1080/01431160110115014>
- Crósta, A. P., De Souza Filho, C. R., Azevedo, F., & Brodie, C. (2003). Targeting key alteration minerals in epithermal deposits in Patagonia, Argentina, using ASTER imagery and principal component analysis. *International Journal of Remote Sensing*, 24(21), 4233–4240. <http://doi.org/10.1080/0143116031000152291>
- Crosta, A. P., & Rabelo, A. (1993). Assessing Landsat/TM for hydrothermal alteration mapping in central- western Brazil. *Exploration, Environment and Engineering. Proc. Ninth Thematic Conference on Geologic Remote Sensing, Pasadena, 1993. 2 Vols.* Environmental Research Institute of Michigan, Ann Arbor.
- Fraser, S. J., & Green, A. A. (1987). A software defoliant for geological analysis of band ratios. *International Journal of Remote Sensing*, 8(3), 525–532. <http://doi.org/10.1080/01431168708948659>
- Hauff, P. (2008). An overview of VIS-NIR-SWIR field spectroscopy as applied to precious metals exploration. *Arvada, Colorado: Spectral International Inc, 80001*, 303–403.
- Hede, A. N. H., Kashiwaya, K., Koike, K., & Sakurai, S. (2015). A new vegetation index for detecting vegetation anomalies due to mineral deposits with application to a tropical forest area. *Remote Sensing of Environment*, 171, 83–97. <http://doi.org/10.1016/j.rse.2015.10.006>
- Iwasaki, A., & Tonooka, H. (2005). Validation of a crosstalk correction algorithm for ASTER/SWIR. *IEEE Transactions on Geoscience and Remote Sensing*, 43(12), 2747–2751. <http://doi.org/10.1109/TGRS.2005.855066>

- Liu, L., Zhuang, D.-F., Zhou, J., & Qiu, D.-S. (2011). Alteration mineral mapping using masking and Crosta technique for mineral exploration in mid-vegetated areas: a case study in Areletuobie, Xinjiang (China). *International Journal of Remote Sensing*, 32(7), 1931–1944. <http://doi.org/10.1080/01431161003639678>
- Marcoux, E., & Milési, J.-P. (1994). Epithermal gold deposits in West Java, Indonesia: geology, age and crustal source. *Journal of Geochemical Exploration*, 50(1-3), 393–408. [http://doi.org/10.1016/0375-6742\(94\)90033-7](http://doi.org/10.1016/0375-6742(94)90033-7)
- Milési, J. P., Marcoux, E., Sitorus, T., Simandjuntak, M., Leroy, J., & Bailly, L. (1999). Pongkor (west Java, Indonesia): a Pliocene supergene-enriched epithermal Au-Ag-(Mn) deposit. *Mineralium Deposita*, 34(2), 131–149. <http://doi.org/10.1007/s001260050191>
- Okada, K., Segawa, K., & Hayashi, I. (1993). Removal of the vegetation effect from LANDSAT TM and GER imaging spectroradiometer data. *ISPRS Journal of Photogrammetry and Remote Sensing*, 48(6), 16–27. [http://doi.org/10.1016/0924-2716\(93\)90052-O](http://doi.org/10.1016/0924-2716(93)90052-O)
- Pour, A. B., Hashim, M., & van Genderen, J. (2013). Detection of hydrothermal alteration zones in a tropical region using satellite remote sensing data: Bau goldfield, Sarawak, Malaysia. *Ore Geology Reviews*, 54, 181–196. <http://doi.org/10.1016/j.oregeorev.2013.03.010>
- PT Aneka Tambang. (2014). *2014 annual report PT. Aneka Tambang Tbk*. Jakarta, Indonesia.
- Rowan, L. C., Wetlaufer, P. H., Goetz, A. F. H., Billingsley, F. C., & Stewart, J. H. (1974). *Discrimination of rock types and detection of hydrothermally altered areas in south-central Nevada by the use of computer-enhanced ERTS images*. Professional Paper (- ed.). Retrieved from <http://pubs.er.usgs.gov/publication/pp883>
- Sabins, F. F. (1999). Remote sensing for mineral exploration. *Ore Geology Reviews*, 14(3-4), 157–183. [http://doi.org/10.1016/S0169-1368\(99\)00007-4](http://doi.org/10.1016/S0169-1368(99)00007-4)
- Syafrizal, Imai, A., Motomura, Y., & Watanabe, K. (2005). Characteristics of gold mineralization at the Ciurug vein, Pongkor gold-silver deposit, West Java, Indonesia. *Resource Geology*, 55(3), 225–238. <http://doi.org/10.1111/j.1751-3928.2005.tb00244.x>
- Syafrizal, Imai, A., & Watanabe, K. (2007). Origin of ore-forming fluids responsible for gold mineralization of the Pongkor Au-Ag deposit, West Java, Indonesia: evidence from mineralogic, fluid inclusion Microthermometry and Stable isotope study of the Ciurug–Cikoret veins. *Resource Geology*, 57(2), 136–148. <http://doi.org/10.1111/j.1751-3928.2007.00013.x>

- Tangestani, M. H., & Moore, F. (2000). Iron oxide and hydroxyl enhancement using the Crosta Method: A case study from the Zagros Belt, Fars Province, Iran. *ITC Journal*, 2(2), 140–146.
- Tangestani, M. H., & Moore, F. (2001). Comparison of three principal component analysis techniques to porphyry copper alteration mapping: A case study, Meiduk area, Kerman, Iran. *Canadian Journal of Remote Sensing*, 27(2), 176–182.
- Tiwari, P. S., Sen, A. K., & Garg, R. D. (2011). Application of DPCA Technique in Khetri Copper Belt, India for Alteration Zones. *Asian Journal of Earth Sciences*, 4(1), 54–59. <http://doi.org/10.3923/ajes.2011.54.59>

Chapter 7

Summary and future works

7.1. Summary

GBRS for mineral exploration in densely vegetated areas was developed and applied in this study. The main works included analyzing the responses of plants in metal-contaminated soils, developing a new VI called the VIGS for detecting vegetation anomalies, correlating spectral attributes derived from satellite imagery and geochemical data, applying VIGS for detecting mineral deposits, proposing novel combined methods for detecting vegetation anomalies, and improving an image-enhancement method to detect alteration zones in vegetated areas. Each of the above works can be summarized as follows.

Chapter 2 was aimed at developing a geobotanical remote sensing method by analyzing the effect of metals on vegetation reflectance at various wavelengths (from visible to SWIR) under laboratory conditions. The purpose of the experiment was to clarify the changes in the reflectance spectra of plants with different metal concentrations in soil and with different types of metals, and to develop a new VI based on the experimental results. The conclusions are as follows:

- Vegetation stress due to contamination of soil by metals (Cu, Pb, Zn, and Cd) in Japanese mustard spinach showed clear effects on the rate of plant growth under conditions of higher metal content. The contamination also caused chlorosis of the leaves, which caused a decline in the photosynthetic rate and induced chlorophyll deficiency in the leaves.
- There were changes in the reflectance spectra with different types and levels of metal exposure. In concordance with the magnitude of the decrease in total chlorophyll content,

reflectance in the visible region increased with increasing metal content. In NIR and SWIR, there were two patterns of reflectance change in which these phenomena were related to either deformation of the cells or an increase in the reflective surface area of the cells.

- A new VI that combines reflectances in VNIR and SWIR, the VIGS, is proposed that will enhance the detection of vegetation stress due to metal absorption. To evaluate sensitivity, the VIGS was compared to the normalized difference vegetation index (NDVI). The VIGS was proven to be more sensitive for detecting vegetation stress because it considers both the chloroplast-related stress and the water stress.

Chapter 3 demonstrated the possibility of detecting geochemically-enriched zones through vegetation-reflectance properties under natural conditions. The analysis was conducted by correlating the reflectance values derived from satellite imagery (Landsat ETM+ image) with geochemical data. This relationship was also examined by a partial least squares regression (PLSR) analysis. The main results are as follows.

- A Pearson's correlation analysis of the reflectance values and metal contents showed slightly higher correlations between the metal content of Cu, Zn, Ni, and K and the reflectance of all ETM+ bands, except for the thermal band, compared with other metals.
- Weak correlations with Pb, Co, Mn, Li, Cr, and Fe content occurred at the limited bands. Further investigation is needed to more accurately classify vegetation species and to increase the number of ground truths to validate the imagery-based results.
- The slightly higher correlations found by the PLSR analysis suggest that it is possible to detect enriched zones in forest areas by the reflectance values of the Landsat-series imagery.

Chapter 4 described one of the highlights of this overall GBRS study. In this chapter, the effectiveness of VIGS as developed in Chapter 2 was applied to Landsat ETM+ imagery of a tropical forest in Jambi, Sumatra, Indonesia, where mineral deposits of copper porphyry exist and mineralized zones are distributed among places (data set as shown in Chapter 3). A set of soil geochemical data was used as a ground truth to evaluate the positional concordance of the VI anomalies derived from the imagery with the soils of high metal concentration. The main results can be summarized as follows:

- Vegetation stress from three metals (Cu, Pb, and Zn) in the soil frequently appeared in the reflectance spectra, in both the VNIR and SWIR regions. By correlating metal content categories in the top layer, which were prepared by kriging interpolation and the C-A model and using NDVI and VIGS values, VIGS superiority was confirmed. This was because VI changes according to metal content were more discriminable by VIGS than by NDVI for all metals.
- To simplify spatially scattered VIGS values, a method for characterizing VIGS anomaly values was proposed. This method used the C-A model of the density of points whose VIGS values were greater than the mean plus standard deviation. High-density zones generally corresponded to those of high metal content, which verifies VIGS applicability for mineral explorations in areas thickly covered by vegetation.

The effectiveness of the VIGS has been demonstrated in a tropical area via correlations with geochemicals, as presented in Chapter 4. However, this analysis is based on a single observation, and because images change over space and time, the accuracy and sensitivity of this approach require further clarification. Thus, Chapter 5 aimed at improving VIGS as integrated with multi-temporal data to highlight anomalous vegetation characteristics that may be related to

ore deposit distributions. Chapter 5 also presented novel combined methods of remote detection of vegetation anomalies that can be used as indicators of ore deposits. A case study was performed of the Hokuroku District in northern Japan, which has some of the richest ore deposits (volcanogenic massive sulfide and vein-type) in the country and is covered by thick vegetation. The main results are as follows:

- The vegetation anomalies were detectable using VI analysis, in which a key variable to detect the anomalies was a variation of the VI with time at each pixel.
- Differences in variation were enlarged by a sequence of image-enhancement methods for the detection of vegetation-anomaly zones. The locations of vegetation-anomaly zones were found to be appropriate by comparing the anomalies with a deposit-potential map produced from multiple geological data.
- The above findings create the possibility of the extraction of valuable information that may reveal ore deposits below the surface by optimizing vegetation signatures at the surface, which can be combined with existing exploration databases.

The preceding three chapters used the basic assumption that the satellite image pixels were almost entirely vegetation. However, there is a possibility that the spectra on the image pixels were mixtures of vegetation, soil, rock, and other features; the contributions of soil and rock reflectances were more or less included. Chapter 6 was built prior upon to this spectra mixture problem and aimed to improve one of the image-enhancement methods, the directed principal component analysis (DPCA), in order to enhance the hydrothermal alteration zone in a vegetated area by optimizing the combination band ratio integrated with a geographic information system (GIS)-based analysis. The study case took place in the Pongkor district, Bogor, Indonesia, where

vein-type Au-Ag epithermal deposits can be found. The main results can be summarized as follows:

- ASTER data provided a wider range of bands to discriminate mineral alteration characteristics that are useful in selecting band combinations in DPCA methods. There were thus more options to explore the optimum band combinations as representations of vegetation and mineral components.
- The present study used the normalized difference-based ratio for rationing the bands, which has advantages over the simple ratio used in traditional DPCA, e.g., enhanced variations of the spectral reflectance between two wavelength bands and delimited lower and upper bound values.
- The alteration zones extracted by this combination were confirmed to be plausible and consistent with the mineralization and alteration zones. However, there are some considerations related to unsuccessful use of DPCA to enhance the alteration zones, which may be caused by geologic and vegetation-cover conditions.

7.2. Future works

The GBRS discussed in this study was related to the effects of metal absorption in vegetation that can be detected by changes in reflectance spectra in visible-to-SWIR wavelength regions, and the application was limited to multispectral imagery. As a recent advance, VIs derived from a more limited wavelength range on hyperspectral imagery have successfully detected vegetation stress due to metals. This is unavoidable, given that the objective of this study is to provide a new perspective and methods that can be widely used to solve the problem of remote sensing for mineral exploration in densely vegetated areas. For example, hyperspectral

imagery does not cover all of the land on Earth. Landsat and ASTER imagery are more versatile because they provide global coverage of land surfaces. However, future research may integrate the thermal bands that have already revealed quartz minerals and certain soil types in a GBRS study.

One of the critical issues in this study was scaling from the laboratory (leaf scale) to the field (canopy scale). The present study did not use detailed information about the vegetation structures because of an insufficiency of data, which is a limitation of this study. The consideration of vegetation structures, such as canopy height and shape, will be necessary to generalize the superiority of VIGS in future research. At present, some parts of the study areas are difficult to be approached because of the remoteness and poor accessibility. Special cautions and equipment are indispensable to walk through the trees. Due to these conditions and restrictions, the reflectance spectra measurement for the ground-truth data is difficult. However, ground-truthing is needed as complementary to satellite image interpretation, which may include extensive chemistry and spectroscopy analyses of rocks, soil, and leaf samples in the future studies.

The application of GBRS in this study was also limited to certain metal elements and deposit types. Specifically, this study successfully detected vegetation anomalies that may be related to porphyry, epithermal, and volcanogenic massive sulfide deposits in different locations and under different vegetation conditions. However, as mentioned above, the vegetation condition is a complex process and its underlying physiology is not yet entirely understood, so continuation of this study is needed. There is an open possibility of applying these study results to different types of metals and deposits, such as orthomagmatic, lateritic, or sedimentary

deposits. Finally, it is required to determine the limitation of depth and magnitude of ore deposits for applying GBRS that will conduct in the future works.

List of associated publications and presentations

- Chapter 2; Hede, A. N. H., Kashiwaya, K., Koike, K., & Sakurai, S. (2015). A new vegetation index for detecting vegetation anomalies due to mineral deposits with application to a tropical forest area. *Remote Sensing of Environment*, 171, 83–97.
- Chapter 3; Hede, A. N. H., Kashiwaya, K., Koike, K., & Sakurai, S. (2013). Correlating vegetation reflectance spectra of satellite imagery with geochemical data for remote sensing mineral exploration in vegetated areas. *International Symposium on Earth Science and Technology 2013*, Fukuoka, Japan.
- Chapter 4; Hede, A. N. H., Kashiwaya, K., Koike, K., & Sakurai, S. (2015). A new vegetation index for detecting vegetation anomalies due to mineral deposits with application to a tropical forest area. *Remote Sensing of Environment*, 171, 83–97.
- Chapter 5; Hede, A. N. H., Kashiwaya, K., Koike, K., & Sakurai, S. (2013). Detection of vegetation anomaly cause by mineral deposits in thickly vegetated areas using a new spectral index and Landsat ETM+ imagery. *The 10th MMIJ Young Researchers Conference 2013*, Kyoto, Japan.
- Hede, A. N. H., Kashiwaya, K., Koike, K., & Sakurai, S. (2014). Detection of vegetation anomaly caused by mineral deposits from reflectance spectra of satellite imagery in vegetated areas. *GEOINFORUM-2014*, Kyoto, Japan.
- Hede, A. N. H., Kashiwaya, K., Koike, K., Sakurai, S., Yamada, R., & Singer, D.A. How can satellite imagery be used for mineral exploration in thick vegetation areas? Submitted to *Scientific Reports* (under review).
- Chapter 6; Hede, A. N. H., Kashiwaya, K., Koike, K., & Sakurai, S. (2014). Application of remote sensing to detecting hydrothermal alteration zones covered by thick vegetation. *The 13th International Symposium on Mineral Exploration*, Hanoi, Vietnam.